博士論文

Study on photochemical reactions based on optical near-fields

（近接場光に基づく光化学反応に関する研究）

A Thesis in the Field of Electrical Engineering and Information Systems

for the Degree of Doctor of Engineering

University of Tokyo

November 30, 2018

ブランデンブルグ　フェリックス　ユリアン

Brandenburg Felix Julian (37-167086)

Supervisor　　Takashi Yatsui

Copyright 2018 [Felix Julian Brandenburg]

Abstract

Optical near-field (ONF) theory has recently started to receive a lot of attention in the academic landscape, and its applications show promise for improving nanoscale fabrication and nanoscale sensing applications. They are locally induced amongst material surfaces when being illuminated by far-field light sources, and it was found that these localized ONFs can interact with their surrounding and cause surface structure changes. In this thesis three experiments are presented in which ONF based photochemical reactions were used to condition sample surfaces. It is found that these photochemical reactions are able to reduce the surface roughness as well as increase sensing parameters of specific samples. In the first experiment (Chapter 4), ONF based photochemical reactions, hereby called near-field (NF) etching, are used to reduce the surface roughness of photoresists. Both light sources used, 325 nm and 405 nm, for inducing the ONFs, are able to reduce the surface roughness of the photoresist. On top of that, 325-nm light reduces the overall width of the photoresist structure. In the second experiment (Chapter 5), NF etching is used to improve the surface conditions of Nitrogen-vacancy (NV) nanodiamonds in order to improve NV spin properties. NF etching seems to remove paramagnetic noise along the surface of the NV nanodiamond, and it is found that with ongoing etching time the T_2 coherence time and the full-width at half-maximum (FWHM) value, obtained from the emission spectrum, are being improved. The effectiveness of NF etching has been further confirmed by detecting a significant size reduction of the nanodiamonds through an atomic force microscope (AFM). In the third experiment (Chapter 6), localized ONFs induced in

Au nanoparticles (NPs) (typically ~6 nm) are used to catalyze the photosensitized reduction of silver-ions. This experiment is performed in order to obtain a more fundamental understanding of the ONF power-dependence, by using synthesized silver as an indicator for the NF magnitude.

Overall, these results show that our NF based processing techniques can be used to improve lithography based nanoscale fabrication of semiconductors, by reducing the photoresist roughness, and improve nanoscale magnetic sensing applications, by prolonging electron spin properties in NV nanodiamonds. The etching results are interesting since they are performed under ambient conditions, based on a non-contact etching technique and can generally be used to improve any nanoscale surface-reliant application.

Acknowledgments

The work describes in this thesis would not have been possible without the help, guidance and support of many collaborators and friends. I would like to thank them for their contributions here.

First of all, I would like to thank my supervisor, Prof. Takashi Yatsui. Over the last 5 years he guided me and has always been the utmost supportive, understanding and patient with me. He would always take his time to thoroughly discuss and explain new ideas and concepts to me. Without his support I would not have had the chance to come and successfully study at the University of Tokyo, and for that I am deeply grateful.

I am also thankful for all of the other members of Yatsui laboratory, who were always eager to assist me in various situations. Special thanks go to Drs. Maiku Yamaguchi and JunHyoung Kim who always took their time to talk to me about physics. They were both key figures in the course of my PhD, and I truly admire both of them. I would also like to thank Takumi Sato, Kota Saichi, Hiroshi Saito and Ryosuke Nagumo who helped me a lot with various experimental setups and discussions.

Also I would like to thank the technical staff of our department, especially Mizushima-san, Ota-san and Oshikawa-san, for helping me with various machines.

Along the course of my study I have also had the pleasure to be consulted by truly uniquely smart and inspirational people, hence I would also like to thank Prof. J. J. Delaunay (University of Tokyo), Prof. O. Soppera (Institut de Science des Matériaux de Mulhouse) and Prof. F. Jelezko (Ulm University).

And of course, I would like to thank all of my family and friends, who always gave me support and joy, as well as all of the people I've had the pleasure of meeting over the course of my stay at the University of Tokyo and Japan.

.

Table of Contents

Chapter 1. Introduction 1

1.1 Background 1

1.1.1 Next generation photolithography based on photoresists........3

1.1.2 NV nanodiamond magnetic sensing.......................................5

1.2 Relationship between the chapters 7

1.2.1 Chapter 2 Optical near-fields 10

1.2.2 Chapter 3 Fundamentals of NF etching 11

1.2.3 Chapter 4 Reducing organic photoresist surface roughness.............11

1.2.4 Chapter 5 Improving NV nanodiamond electron spin properties 11

1.2.5 Chapter 6 Synthesis of Ag nanoparticles by NF based photo-reduction of Ag^+ 12

1.2.6 Chapter 7 Conclusion and outlook 12

Chapter 2. Theory of optical near-fields 13

2.1 Optical near-fields 13

2.2 Quantitative difference through NFs 15

2.3 Qualitative difference through NFs 17

Chapter 3. Near-field etching 19

3.1 Near-field (NF) etching principle..19

3.2 NF etching and other gases in air (besides O_2) 21

3.3 NF caused dissociation of H_2O 23

3.4 NF etching on various materials 25
Chapter 4. Reducing organic photoresist surface roughness..31
4.1 Background 31
4.2 LER and other roughness values of photoresists 35
4.3 NF etching on photoresists...37
4.4 Experimental 40
4.5 Results and Discussion..42
Chapter 5. Improving NV nanodiamond electron spin properties....................................56
5.1 Background 56
5.2 Structure of the NV Center 57
5.3 Readout, AC and DC Sensing with NV centers..58
5.4 Surface noise influence on NV spin properties...64
5.5 NF etching on NV nanodiamonds...66
5.6 Experimental 68
5.7 Results and Discussion..70
Chapter 6. Synthesis of Ag nanoparticles by NF based photo-reduction of Ag^{+} 85
6.1 Background 85
6.2 ONF power dependency..85
6.3 NF based silver synthesis...89
6.4 Results and Discussion..90
Chapter 7. Conclusion and Outlook. 102
7.1 Summary and outlook for Chapter 4 102
7.2 Summary and outlook for Chapter 5 102

7.3 Summary and outlook for Chapter 6 103

7.4 Final summary and outlook 104

Appendix A. Methods and analysis for the experiments presented in Chapter 4 106

A.1 Atomic force microscopy (AFM) with L-Trace II 106

A.2 Surface roughness evaluation 107

Appendix B. Methods and analysis for the experiments presented in Chapter 5 108

B.1 Charge of the NV Center 108

B.2 Electronic structure model of the NV center 109

B.3 Optical properties of the NV Center 109

B.4 Hahn-Echo T_2 coherence time 111

B.5 Confocal microscopy & NF etching setup 112

B.6 Nanodiamond sample preparation 117

B.7 NF etching laser parameters 117

Appendix C. Methods and analysis for the experiments presented in Chapter 6 119

C.1 Photosensitive silver-ion solution 119

C.2 Machine vision software for evaluating TEM images for particle sizes 121

C.3 Energy-dispersive X-ray spectroscopy (EDS) analysis of gold nanoparticles after experiment 122

References 124

List of Publications 139

I. Journal Publications 139

II. Conferences (International) 139

III. Conferences (Domestic) 140

List of Figures

Figure 1.1. Connection between thesis experiments. 9

Figure 1.2. Structure of this thesis 10

Figure 2.1. Localized ONF induced around a nanoparticle 14

Figure 2.2.Uncertainty principle 15

Figure 2.3. Surface enhanced Raman spectroscopy 16

Figure 2.4. Two-photon spectroscopy gold nanorods 16

Figure 2.5. Plasmon based photovoltaic devices 17

Figure 2.6. The non-uniformity of ONF 18

Figure 3.1. Scheme of NF etching 19

Figure 3.2. The photo-dissociation of O_2 by ONF 21

Figure 3.3. Atmospheric composition 22

Figure 3.4. Theoretically calculated N_2 dissociation energies 23

Figure 3.5. Psychrometric chart, sea-level pressure (101325 Pa) 24

Figure 3.6. Dissociation energy of H_2O. 25

Figure 3.7. NF etching performed on a glass substrate 26

Figure 3.8. NF etching performed on a type Ib diamond substrate 27

Figure 3.9. NF etching performed on a single crystal diamond substrate edge 28

Figure 4.1. Wafer size time-chart 31

Figure 4.2. EUVL extension concerns (post 2017) 32

Figure 4.3. Chemical composition of organic CAR 33

Figure 4.4. RLS tradeoff for EUV 34

Figure 4.5. Evaluation of LER and LWR 35

Figure 4.6. Negative impact of LWR on device performance 36

Figure 4.7. Relation between PR errors (bridges) and CD...37

Figure 4.8. Organic photoresist fabrication sequence 40

Figure 4.9. Photoresist evaluation sequence 42

Figure 4.10. 3D AFM images of photoresists before and after NF etching.......................44

Figure 4.11. Cross-sectional image of photoresist during NF etching..............................46

Figure 4.12. Simulation of photoresist exposure to 325nm laser.......................................48

Figure 4.13. Surface roughness evaluation over NF etching time. 50

Figure 4.14. Inherent organic photoresist absorption spectrum. 51

Figure 4.15. Potentially reducing full- and half-bridges with NF etching 52

Figure 4.16. Challenges in using NF etching for high-end lithography............................54

Figure 5.1. NV center applications...57

Figure 5.2. NV center configuration. 58

Figure 5.3. Energy levels of NV center and illustration of confocal setup. 59

Figure 5.4. Zeeman splitting of spin degeneracies...60

Figure 5.5. ESR based DC Magnetometry with NV ensemble 61

Figure 5.6. ESR based AC Magnetometry 63

Figure 5.7. Common T_2 limitations of NV centers. 64

Figure 5.8. Surface depth dependence of T_2 65

Figure 5.9. Scheme of NV nanodiamond surface conditioning by NF etching..................66

Figure 5.10. Fabrication of ND samples 69

Figure 5.11. Scheme of NF etching on diamonds surfaces 70

Figure 5.12. Size reduction of NV nanodiamonds 72

Figure 5.13. ODMR spectrum and FWHM value of NV center 74

Figure 5.14. T_2 (Hahn Echo) coherence time of NV center 76

Figure 5.15. Cathodo-Luminescence value of NV nanodiamonds......77

Figure 5.16. Photoluminescence intensity spectrum of NV nanodiamonds......78

Figure 5.16. Net T_2 change over etching time......83

Figure 5.17. Target sensing applications for NF etching 84

Figure 6.1. Nano-second laser power-dependent etching 86

Figure 6.2.Power dependency of ONFs 87

Figure 6.3. Scheme of NF based silver reduction amongst gold nanoparticles 89

Figure 6.4. Plasmon resonance spectrum for gold nanoparticles 90

Figure 6.5. Silver nanoparticle synthesis caused by 325 nm light absorption......91

Figure 6.6. TEM image of Au NPs observed for topological changes......92

Figure 6.7. Initial size distribution of Au NPs 94

Figure 6.8. Power-dependency for ONF-based Ag synthesis 95

Figure 6.9. NF-effects vs. Thermal-effects in Ag synthesis......96

Figure 6.10. Power-dependency for FF-based Ag Synthesis 97

Figure 6.11. Illustration of FF saturation due to limited availability of photo-components. 98

Figure 6.12. Power-dependency for FF-based Ag Synthesis 99

Figure 6.13. Theoretical and experimental ONF power-dependency comparison......101

Figure A.1 User interface for inbuilt AFM roughness evaluation software......106

Figure A.2 Mathematical model visualizing the best fitting plane 107

Figure B.1. Scheme of Hahn-Echo T_2 112

Figure B.2. Confocal microscopy setup combined with NF etching 113

Figure C.1. Molecular structure of Irgacure 819...119

Figure C.2. Molecular structure of Irgacure 819. 120

Figure C.3. National Instruments Computer Vision software 122

Figure C.4. EDS proof of Gold and Silver traces...123

Citations to previously published work

Chapter 4 has been published as

"Surface improvement of organic photo-resists through a near-field-dependent etching method," F. Brandenburg, T. Okamoto, H. Saito, O. Soppera & T. Yatsui, *Beilstein Journal of Nanotechnology* **8**, 784-788 (2017).

Chapter 5 has been published as

"Improving the electron spin properties of nitrogen-vacancy centres in nanodiamonds by near-field etching," F. Brandenburg, R. Nagumo, K. Saichi, K. Tahara, T. Iwasaki, M. Hatano, F. Jelezko, R. Igarashi & T. Yatsui, *Scientific Reports* **8**, 15847 (2018).

.

Chapter 1.

Introduction

1.1 Background

We currently have a principal idea about ONF theory, mainly through first principle simulations, however experimental data is still lacking for a more fundamental understanding of ONFs. In fact, one area of ONFs which has been to some extent studied through experiments is NF etching. Previous research confirmed that we can use ONFs as catalysts for photochemical reactions, especially in form of etching which resulted in ultra-flat surface conditions (much smoother than conventional chemical/mechanical surface flattening techniques), however, those experiments have been mostly performed on inorganic materials, which due to their innate sturdiness can be rather difficult to be shaped (often too little change visible under e.g. atomic force microscope (AFM)). Hence in this thesis NF etching is being applied on a novel material, organic photoresists. Since they naturally have a higher porosity then inorganic materials, etching effects should be more visible (easier removal of atom layers). There are two main benefits of studying NF etching on organic photoresists. First of all, we will be able to see NF etching effects more clearly (due to organic photoresists porosity). Secondly, NF etching shows potential to improve high-end industrial lithography fabrication of nanoscale semiconductors. It is well known that due to the low dimensions we are moving towards, sub 10nm, scattering losses play an increasingly crucial role. And NF etching could be the game-changer for sub 10nm

photoresist lithography, since its surface roughness reduction surpasses all other currently available flattening techniques.

Building on the successful results of the NF etching experiments on photoresists (surface conditioning as well as size control), I figured that nitrogen-vacancy (NV) nanodiamond for magnetic sensing could be another application which drastically benefits from NF etching. Nanodiamonds generally have a higher surface-per-volume ratio than bulk diamond and often suffer from paramagnetic residue, such as termination groups, originating from their fabrication processes. Unfortunately spin coherence times of NV centers are quite susceptible to paramagnetic noise in its surrounding. NF etching has the potential to remove paramagnetic noise on the NV nanodiamond surface and thus improve NV electron spin properties, especially the coherence time T_2, resulting in an improvement of NV nanodiamond magnetic sensing applications. By successfully improving NV nanodiamond sensing, NF etching can be considered as a serious candidate for improving surface -reliant high-end industrial applications.

After proofing the effectiveness of NF etching in high-end industrial applications, it would be nice to deepen our fundamental understanding of NF etching. More specifically, etching parameters, such as wavelength or excitation power, are still not fully understood. Since etching is overall tricky to evaluate (e.g. inherent variance in surface roughness between samples or low-rate etching rate of NF etching), it should be easier to observe ONF based synthesis. For this purpose, a photosensitive silver-ion solution is being used, which can produce solid silver agglomerations when hit by the right photon energy. The trick is hereby to induce this reaction by using a far-field light source weak enough to be solely responsible for silver induction. The idea is that only with the help of localized

ONFs (amongst gold nanoparticles, since they are ideal for NF experiments) the photochemical reaction can take place. As a result, the induced solid silver can be used as an indicator for the presence of ONFs. The results obtained in this experiment help us to solidify NF theory from an experimental point of view. Also, by studying the dependence of NF parameters, such as far-field wavelength and power density, we can ultimately understand the role of specific parameters for applied NF techniques (i.e. etching), and thus further improving NF etching applications.

1.1.1 Next generation photolithography based on photoresists

Gordon E. Moore predicted in the 1970`s that the number of transistors on an affordable CPU would approximately double every 18 months [1], meaning that every two years people would have access to computers approximately twice as fast. However as electrical components have shrunk below the 10 nm mark [2], and parasitic effects such as electron tunneling make further size reduction difficult, Moore's Law is starting to come to an end. As we continue with structures below the 10 nm mark, and the desire to go even smaller still prevails, the impact of parasitic parameters, such as scattering losses through the surface roughness (SR) is increasing as well [3]. There are a wide-range of attempts to further enable the downscaling of electrical components, e.g. transistors, in an attempt to maintain Moore`s Law [4,5]. As a part of this, we explore new manufacturing techniques [6] in addition to novel materials [7] and they are continuously being proposed in the scientific and industrial society. One of the next-generation candidates for the sub 10 nm mark is Extreme ultraviolet lithography, currently using 13.5 nm. EUV is being developed

for high volume use by 2020 (e.g. Intel 7 nm by 2019, Samsung 7 nm by 2020) [Intel 7nm by 2019, Globalfoundries EUV by 2020, Samsung 7nm by 2020, TSMC 5nm by 2020].

Since most future fabrication techniques are still based on lithographic systems, SR values could suffer on smaller scales, due to the so called resolution (R), line-edge-roughness (LER), and sensitivity (S) trade-off (RLS trade-off) principle for highly precise lithography [8]. The trade-off relation is between the resolution, line edge roughness and sensitivity of the lithography. And as expected, one of the most important criteria for new materials and techniques to be a realistic candidate for sub 10 nm fabrication is a low SR value, especially for high-end lithography (such as Extreme ultraviolet lithography), due to the mentioned trade-off relation. When considering ways to reduce SR values, polishing is the most often sought-after technique. However, the ordinary chemical mechanical polishing (CMP) technique [9] is usually restricted by the inherent surface roughness of the polishing pad, typically within the micrometer range, as well as by the diameter of the chemical slurry particles itself, which is most often in the 100 nm range. [10]. This means that reducing the surface roughness to values far below the 100 nm range might be quite tricky to accomplish when only using the conventional CMP method. Even more so, the high cost and limited material availability for the rare-earth material CeO_2 which is used in CMP, causes people to start looking for alternative etching techniques. We hereby introduce the novel etching technique, the so called NF etching, to further realize SR reduction without using conventional etching techniques (such as CMP) and ensure roughness values of sub 1 nm.

1.1.2 NV nanodiamond magnetic sensing

The NV center in diamond has become a promising candidate for quantum computing applications as well as magnetic sensing applications, especially in biotechnology [11-15], due to its atomic-scale size which allows it to get into close proximity to its target as well as a stable coherence time (T_2) and accessibility even at room temperature. We will demonstrate the effectiveness of NF etching for improving NV nanodiamond spin properties (the full width half maximum (FWHM) value obtained out of the optically-detected magnetic resonance (ODMR) spectrum as well as its T_2 coherence time). The NV center can conveniently be read out by a controlling laser, and from the NV spin resonances (e.g. ODMR) as well as its shift when exposed to magnetic fields, we can deduce its magnetic sensitivity, which is generally dependent on NV coherences properties [16]. Another example for sensing applications would be to directly observe the change in the NV coherence time when being in close proximity to magnetic molecules [17]. This latter method has also been labelled as by the term “quantum sensing” [18]. Regardless of which approach we take for NV sensing, the importance of T_2 for either technique prevails.

Another thing we should consider is quantum computing, and its critical requirement of a qubit candidate to have long enough coherence times. More precisely, the coherence time is the time in which the system stays in a superposition state, in which it is generally sensitive towards external magnetic effects, or in the case of quantum computing, the time where it can be effectively used for the transmission of quantum information. It was previously announced by D. DiVincenzo that for a quantum qubit system to be a valid quantum computing candidate, it needs to have a long enough coherence time. More precisely, to have a coherence time which is longer than the gate operation time [19]. This

makes up one of the most important criteria in our search for the perfect quantum qubit candidate. Unfortunately most of our current qubit candidates, especially considering room temperature operation, have a rather short coherence time, meaning that they lose their quantum information too quickly. One possible solution to this problem would be increasing the coherence time of qubit candidates by conditioning their surfaces, i.e. removing magnetic noise on their surfaces and thus increasing their coherence times. In chapter 5 it is my goal to push the coherence time of the NV center to its maximum. Previously it was already possible to achieve coherence times within the minute range, mainly by making use of ionized donors in combination with special optical methods and dynamical decoupling [20], however it is still of great interest to find simpler techniques which can at the same time work under ambient conditions, such as the NV center is often used in. The NV center is an excellent candidate for qubit and sensing applications, since it naturally has got some excellent properties, such as long electron-spin coherence and relaxation times and also stable magnetic and optical characteristics [21-26], in addition to the fact that diamond is an excellent candidate for biological applications as well, due to its non-toxicity. NV centers can be driven remotely by optical pumping (532 nm). Together with using microwaves to cause the electron spin population to oscillate between its respective energy levels, we can basically remotely initialize, drive and read out the NV center [27,28,29]. Normally, under room temperatures, the coherence time of the NV center typically lies within the microsecond range [30], while the current record of 1.8 ms has been achieved by the usage of an ultrapure isotopically engineered single-crystal chemical vapor deposition (CVD) method. This was basically realized by first of all purifying the diamond in order to decrease the amount of additional defects in the crystal. Next,

isotopically engineered carbon, which only consists of the nuclear-spin-free ^{12}C isotopes, are used as the main component of the diamond crystal.

Contrary to NV spin improvements based on new fabrication techniques, post-fabrication surface conditioning techniques (e.g. etching) could be more easily accessible and reproducible. In regards to etching methods which can improve the coherence times of NV centers in diamond, some previous research performed a wet surface etching technique (wet oxidative chemistry combined with annealing at 465 C) on bulk diamonds [31]. Nevertheless, there is currently no report of a reliable etching method for NV nanodiamonds aiming to improve their coherence properties. Hence chapter 5 shall focus on the improvement of electron spin properties of NV nanodiamond.

1.2 Relationship between the chapters

From here onwards the thesis will be divided into six chapters. Chapters 2 and 3 will give a fundamental introduction to ONF theory and its application, NF etching. Chapters 4 and 5 consist of NF etching experiments aiming to improve nanoscale fabrication and nanoscale sensing applications. More specifically, in Chapter 4, NF etching will be applied on organic photoresists (CAR) in order to gain a more fundamental understanding of how NF etching can modify a samples shape. NF etching has been performed on various inorganic materials already with significant results in terms of reduced surface roughness values. However, due to the high mass density and robustness of most inorganic materials, NF etching effects can often be difficult to observe. Therefore in this thesis organic photoresists will be used to study NF etching more thoroughly. Organic photoresists have a lower mass density than inorganic materials and it should therefore be easier to observe structural changes on them. At the same time, organic

photoresist used in the high-end lithography industry suffer from stochastic effects (in form of LER or structural misalignment), so it might be interesting to see whether NF etching has the potential to improve photoresist for industrial purposes. On a more experimental side, it will be interesting to find the significance of different wavelengths for NF etching, and the etching duration overall. The photoresists are hereby evaluated by an AFM, allowing us to observe surface changes. In addition to understanding how NF etching causes surface changes in samples, it would be nice as well to understand how NF etching affects the surface chemistry of samples. However, due to the small dimension (typically lower nanometer range) direct surface chemistry observation seems difficult (e.g. XPS, EDS). As such, in Chapter 5, the NV spin properties, which are directly dependent on the diamond surface chemistry, are being studied in order to (indirectly) derive the relationship between NF etching duration and surface chemistry modification. Hereby the ideal NF etching parameters (i.e. duration and wavelength), which showed the greatest structural change in the samples, obtained in Chapter 4, will be used again in Chapter 5.

Contrary to the previous two chapters, Chapter 6 describes an experiment in which ONFs are used for synthesis. This chapter focuses more on the fundamental limitations of NF-based processing techniques (i.e. etching, synthesis). In Chapter 4 and Chapter 5 a couple of etching parameters were not yet fully understood, such as the power dependency of NF etching. As such, Chapter 6 will use Au nanoparticles (average diameter of the sphere ~ 6 nm) which are an ideal source for the generation of ONFs. The reason why we use NFs for synthesis instead of etching is that synthesis is much easier detectable than etching. Hence, the NF-photosynthesized Ag along the Au NPs shall serve as an indicator for the intensity of ONFs. The experimentally obtained power-dependency of the NF-based

synthesis will be compared to its theoretical values, and will thus serve as further proof for the importance of ONFs for our reactions.

In Fig. 1.1 we can see a brief version of my research timeline over the course of my PhD. Promising results in the preceding chapters allowed me to dive deeper and deeper into NF based experiments and as a result obtain a general picture of how NF etching can influence various sample parameters.

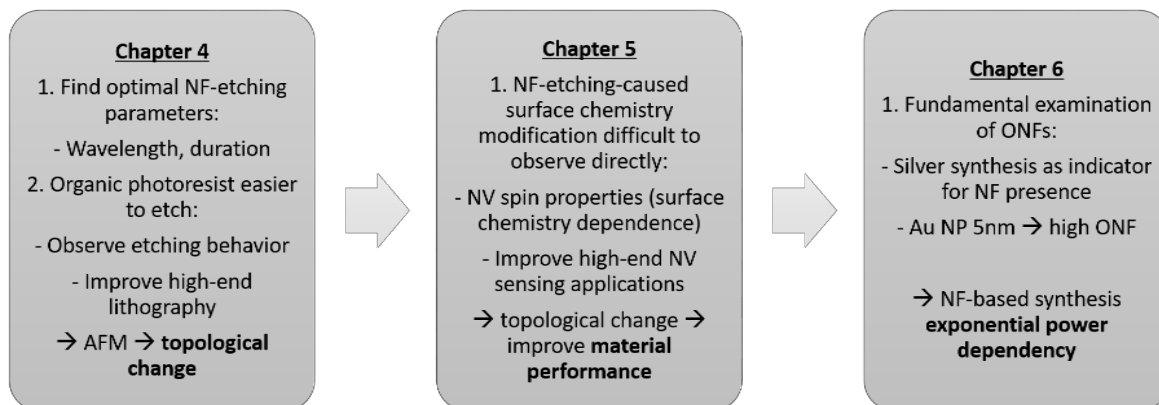

Figure 1.1. Connection between thesis experiments.

The last chapter briefly summarizes the results and significance of the previous chapters.

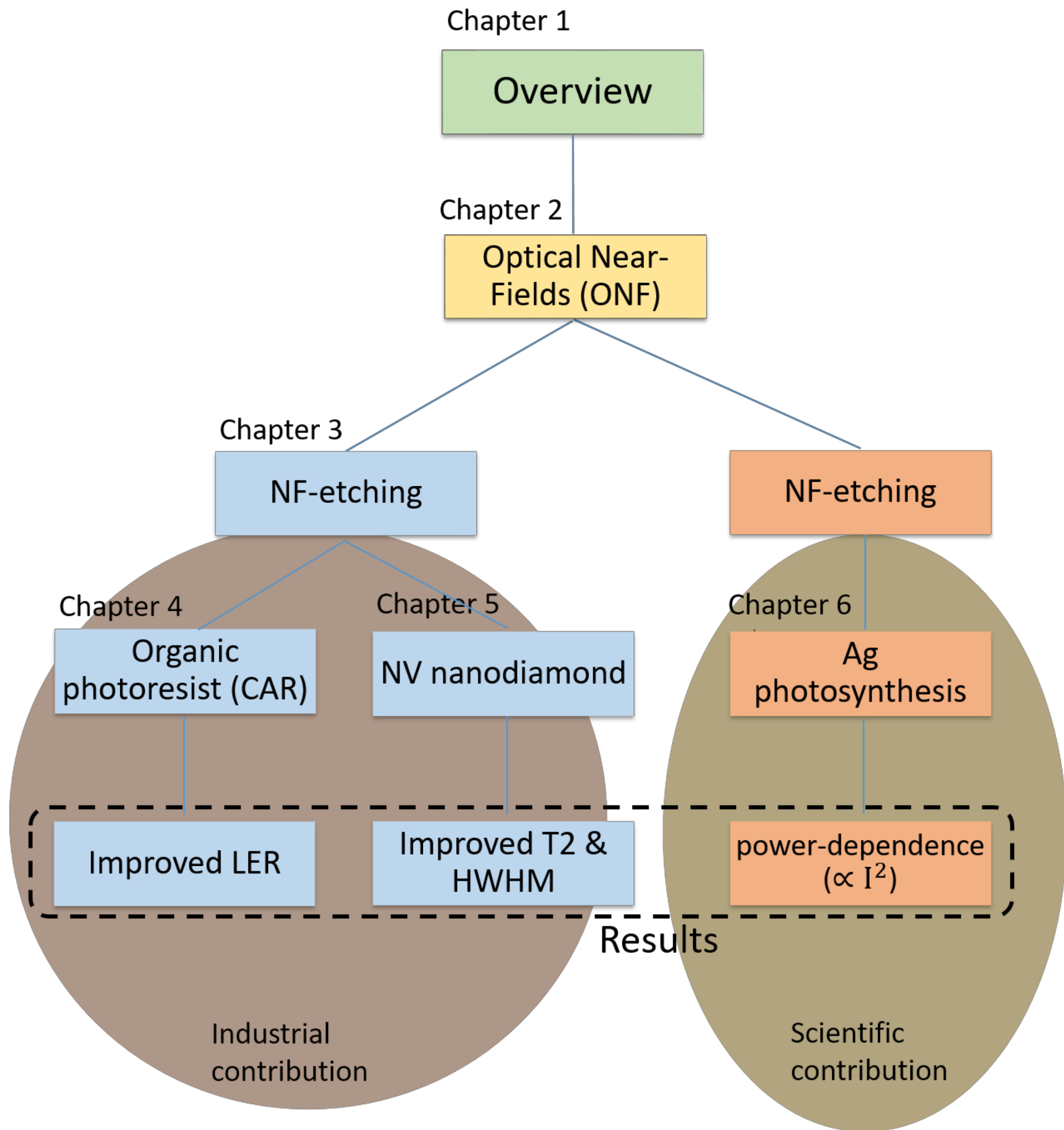

Figure 1.2. Structure of this thesis.

1.2.1 Chapter 2 Optical near-fields

This chapter will explain about the basic theory behind ONFs. The chapter will also include example applications which could potentially benefit from ONFs. Also, I will

explain more concretely which optical phenomena (e.g. ONF-based second harmonic generations) are important to understand for the following parts of the thesis.

1.2.2 Chapter 3 Fundamentals of NF etching

Chapter 3 dives more into the practical side of NF theory, namely NF etching. NF etching has previously been performed for improving surface conditions (i.e. reducing surface roughness) in flat samples as well as sharpen edge contrasts in three-dimensional objects.

1.2.3 Chapter 4 Reducing organic photoresist surface roughness

Chapter 4 shows NF etching applied in a high-end industrial application, namely sub-10nm photolithography using photoresists. For these next-generation fabrication techniques, roughness parameters play an increasingly crucial role (due to scattering losses), and I will demonstrate how NF etching can help to maintain low roughness parameters in the sub-10nm dimensions as well as reduce the amount of structural defects (i.e. bridges).

1.2.4 Chapter 5 Improving NV nanodiamond electron spin properties

Chapter 5 shows NF etching applied in another high-end industrial application, namely NV nanodiamond magnetic sensing. The effectiveness of these nanodiamond sensors is highly dependent their surface condition (i.e. low amount of noise). I will demonstrate how NF etching can help reducing the amount of surface noise, and thus increase their sensing capabilities.

1.2.5 Chapter 6 Synthesis of Ag nanoparticles by NF based photo-reduction of Ag^+

Chapter 6 is an attempt to directly proof the magnitude of localized ONFs, by taking advantage of a photosensitive silver-ion solution (whose reaction will be triggered by NFs). The fundamental results obtained in this chapter will improve further etching applications (by deepening our understanding of etching parameters) as well as generally give us a clearer insight about NF theory (from an experimental point of view).

1.2.6 Chapter 7 Conclusion and outlook

Chapter 7 is listing the conclusions from the three experiments, Chapter 4, 5 and 6, in addition to an overall conclusion of my thesis. This chapter also talks about the outlook of the experiments performed in this thesis.

Chapter 2.

Theory of optical near-fields

2.1 Optical near-fields

Optical near-fields (ONFs) are continuously receiving more and more attention due to their non-uniform properties and the related physical phenomena. In Fig. 2.1 we can see a simplified visualization of how ONFs are induced in sub-wavelength systems. The incoming far-field photon cannot propagate as usual through systems which have a smaller dimension than the photon itself. However the polarization of the incoming light, i.e. the direction of the electric field, let electrons in these sub-wavelength objects oscillate accordingly. A result is that the electrons within the sub-wavelength system distribute themselves along the system, in accordance to the incident light polarization, resulting in net charge differences across the sub-wavelength system. Equation 2.1 shows the general formula for induced electrical dipoles, as stated in Jackson`s Classical Electrodynamics [32].

$$E_{dipole}(\boldsymbol{r}) = \left[\left\{ 3(\boldsymbol{n}\cdot\boldsymbol{p})\boldsymbol{n}-\boldsymbol{p} \right\} \frac{1}{r^3} - \left\{ 3(\boldsymbol{n}\cdot\boldsymbol{p})\boldsymbol{n}-\boldsymbol{p} \right\} \frac{ik}{r^2} + (\boldsymbol{n}\times\boldsymbol{p})\times\boldsymbol{n}\frac{k^2}{r} \right] e^{ikr} \qquad (2.1)$$

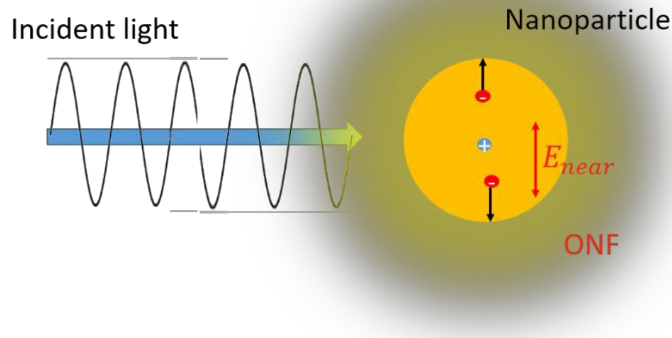

Figure 2.1. Localized ONF induced around a nanoparticle [33].

Scheme of induced localized ONF on a nanoparticle (sub-wavelength system) induced by incident light. (Reprinted with permission from M. Yamaguchi et al. Appl. Phys. Lett. 106, 191103 (2015). Copyright AIP Publishing LLC).

As mentioned before, Fig. 2.1 shows a simplified sketch of the far-field photon interaction with the sub-wavelength system (nanoparticle (NP)). The yellow sphere hereby represents the localized ONF which is induced across the nanoparticle by the far-field light source. More specifically, due to the polarization of the incoming far-field light, a dipole is induced across the nanoparticle with the following equation

$$P(t) = \frac{\epsilon_d-\epsilon_0}{\epsilon_d+2\epsilon_0} a^3 E_{ext}(t) \quad (2.2)$$

Where P(t) stands for the induced dipole, and E_{ext}(t) stands for the electric field of the far-field source. From the dipole equation we can deduct the following equation for the electric field of the ONF:

$$E_{near}(t) = \frac{1}{4\pi\epsilon_0}\left[-\frac{P(t)}{r^3} + \right.$$

3�[�P(�)]

�] (2.3)

From the equation it becomes apparent that effects of the ONF can only be fully seen at very close proximity to the ONF source.

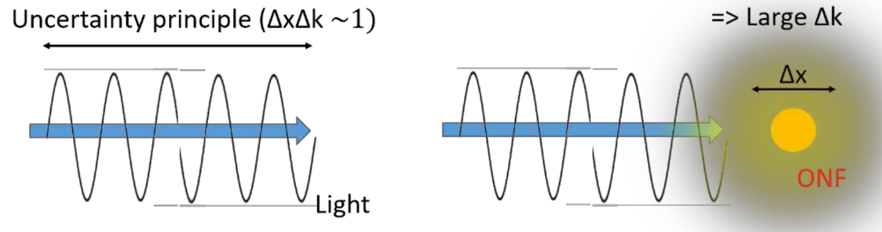

Figure 2.2. Uncertainty principle [33].

Uncertainty principle of the ONF (yellow sphere) photon. (Reprinted with permission from M. Yamaguchi et al. Appl. Phys. Lett. 106, 191103 (2015). Copyright AIP Publishing LLC).

Fig. 2.2 illustrates another interesting characteristic of the ONF photon. Due to the very small spatial displacement (Δx), the uncertainty principle commands that the particle shall have a consequently high wavenumber. This characteristic becomes relevant when considering ONF applications for e.g. indirect bandgap excitations.

The most relevant ways in which ONFs can interact with common applications are on a quantitative and a qualitative basis.

2.2 Quantitative difference through NFs

In this segment I would like to point out example applications in which ONFs have been shown to help improve the said applications (e.g. via signal enhancement).

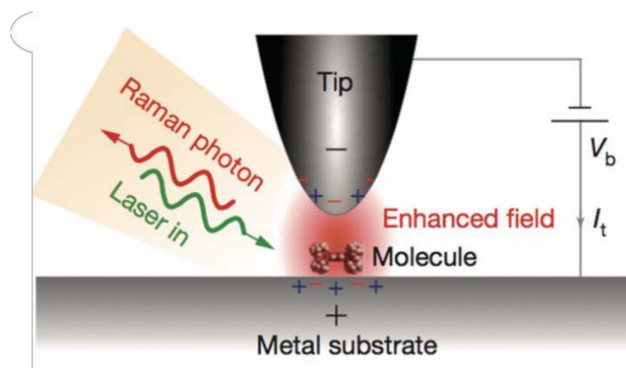

Figure 2.3. Surface enhanced Raman spectroscopy [34,35].

NF enhanced Raman spectroscopy (SERS). Surface-enhanced Raman spectroscopy produces inordinate enhancements compared to the conventional Raman spectroscopy.

Fig. 2.3 depicts a classical application based on ONFs; the NF enhanced Raman spectroscopy (or called surface-enhanced Raman spectroscopy (SERS)). SERS produces inordinate enhancements compared to the conventional Raman spectroscopy, due to the increased local electromagnetic field due to the electromagnetic properties of metal nanoparticles, including their strong potential for induced localized ONFs.

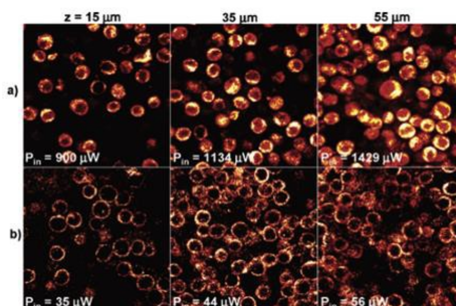

Figure 2.4. Two-photon spectroscopy gold nanorods [36].

Two-photon spectroscopy. Fluorescence samples consisting of a mix between cancer cells and gold nanorods. a) showing the image magnitude when assisting the spectroscopy with NFs, b) conventional image.

In Fig. 2.4 the authors demonstrated that combining their cancer cell samples with gold nanorods as a bright contrast agent for two-photon luminescence imaging can

significantly improve the measured signal. More specifically, it was found that the two-photon luminescence signal of the gold nanorods was by 3 orders of magnitude higher than the two-photon autofluorescence emission of the cancer cells themselves.

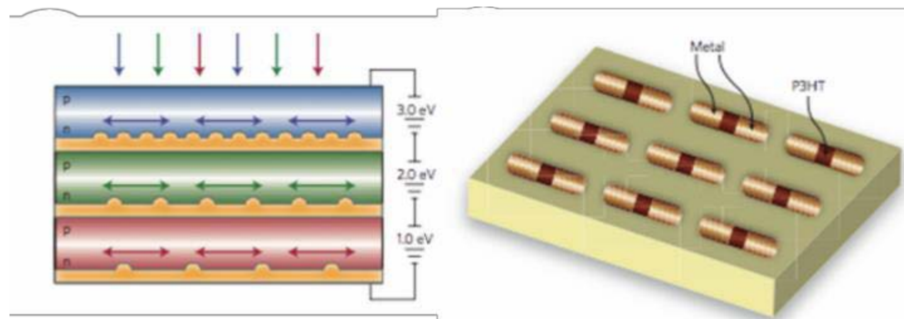

Figure 2.5. Plasmon based photovoltaic devices [37].

Improved energy conversion of photovoltaic devices based on plasmonics generated in the yellow layers between the potential layers of the photovoltaic devices.

In Fig. 2.5 we can see an application of photovoltaic devices in which plasmonic induced field enhancement from sub-wavelength objects along the intersection of the device was used in order to increase the absorption efficiency of said devices.

2.3 Qualitative difference through NFs

In this segment I would like to show how ONFs can qualitatively change applications due to the non-uniformity of its electric field

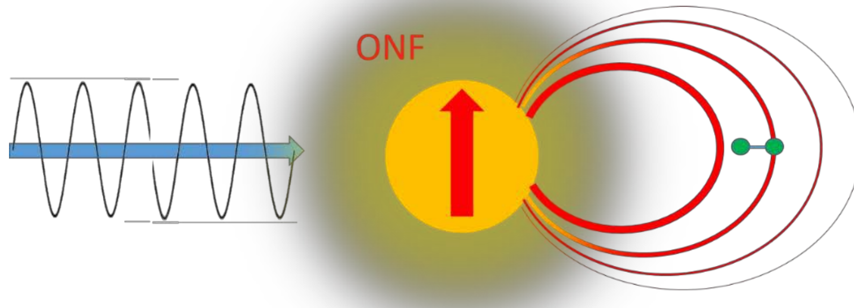

Figure 2.6. The non-uniformity of ONF.

Incident far-field photon (black wave) induces localized ONF (bright yellow) in the sub-wavelength system. The immediate surrounding of ONFs is exposed to a non-uniform electric field (red lines), allowing us to neglect the conventional dipole-approximation. (Reprinted with permission from M. Yamaguchi et al. Appl. Phys. Lett. 106, 191103 (2015). Copyright AIP Publishing LLC).

As can be seen in Fig. 2.6, due to the strong non-uniformity of the electrical field of ONFs, target objects in close proximity to the ONF cannot be any longer regarded to be in a simple dipole-approximation model.

More interestingly, phenomena such as the second harmonic generation (SHG) which under far-field conditions is strongly dependent on the symmetry of the object, can occur more easily under NF conditions.

The reason for this is that when regard a symmetrical model as well as an asymmetrical model, both under far-field conditions, and a symmetrical model cannot induce second harmonic generations. Under far-field conditions, second harmonic generations can only occur if the object has an asymmetrical geometry. However, due to the strong non-uniformity of the NF, second harmonic generations can also occur in objects with symmetrical geometry under NF conditions.

Chapter 3.

Near-field etching

3.1 Near-field (NF) etching principle

In this chapter I would like to outline the general motivation of our laboratory to improve the surface condition (esp. surface roughness) of various devices. We believe that as we move towards smaller sizes (lower nanoscale) there is an increasing demand to ensure that nanoscale devices have smooth surfaces in order to avoid scattering losses.

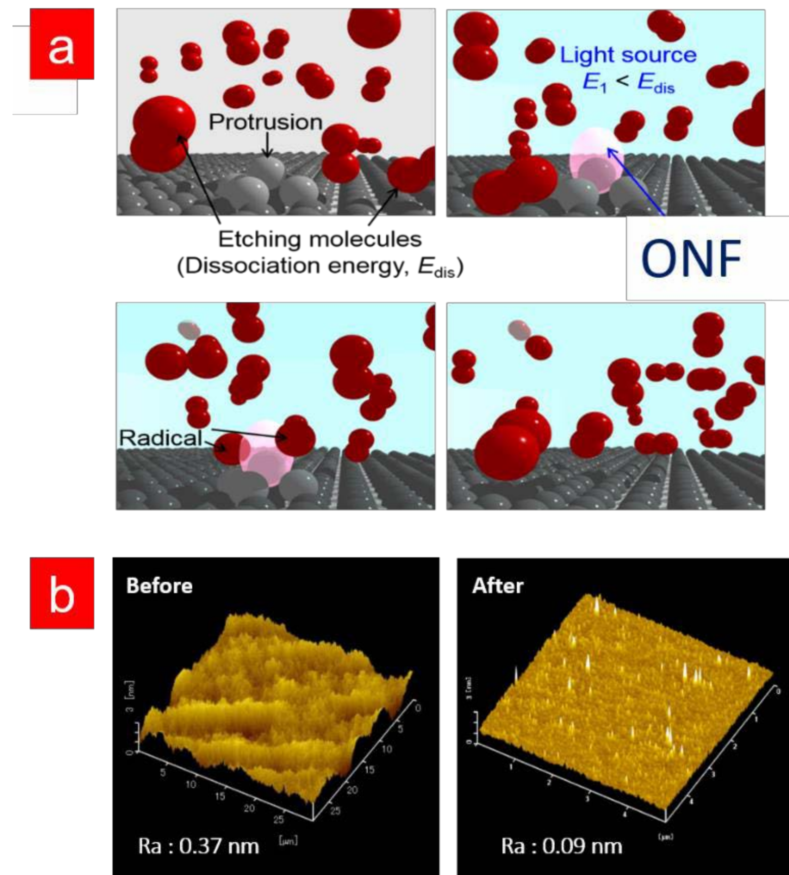

Figure 3.1. Scheme of NF etching [38].

(a) Scheme of how NF etching is assumed to work. Pink spheres represent the induced localized ONFs. The etching agent are gas molecules in the air. (b) Typical before and after image showing how NF etching can reduce the surface roughness.

NF etching is able to improve surfaces by removing surface impurities and protrusions and can thus help improve electrical and/or optical performance of nanoscale devices. As can be seen in Fig. 3.1a, it is assumed that the etching effect originates from radical gas atoms from the air. These strongly reactive atoms interact with the sample surface, resulting in etching. It is important to notice however that in order for the photo-dissociation of the gas molecules (into radical atoms) to happen, we need the ONFs. During NF etching the sample surface is being illuminated by an ordinary far-field light source, with the only requirement being that the photon energy of the far-field light source lays below the direct photo-dissociation energy of the etching agent (most often O_2 molecules) (see Fig. 3.2). The result is that the photo-dissociation can only occur whenever far-field photons are somewhat combined with NF photons, in order to reach the photo-dissociation level of the etching agent. In Fig. 3.1b we can see a typical AFM image of a surface which has been conditioned by NF etching. The NFs are induced on sub-wavelength objects, which in our example (Fig. 3.1a) are the protrusions along the sample surface. As a result, the photo-dissociation of the gas molecules only occurs in the direct vicinity of the localized ONFs (pink spheres), meaning that etching only occurs in the direct vicinity of the localized ONFs as well. It means that NF etching in theory is a nice self-regulating etching technique, hence more protrusions (higher roughness) means more induced localized ONFs and thus more etching, while less protrusions means less induced localized ONFs and thus less etching. NF etching is normally performed under ambient conditions, since we need the gas molecules in the air.

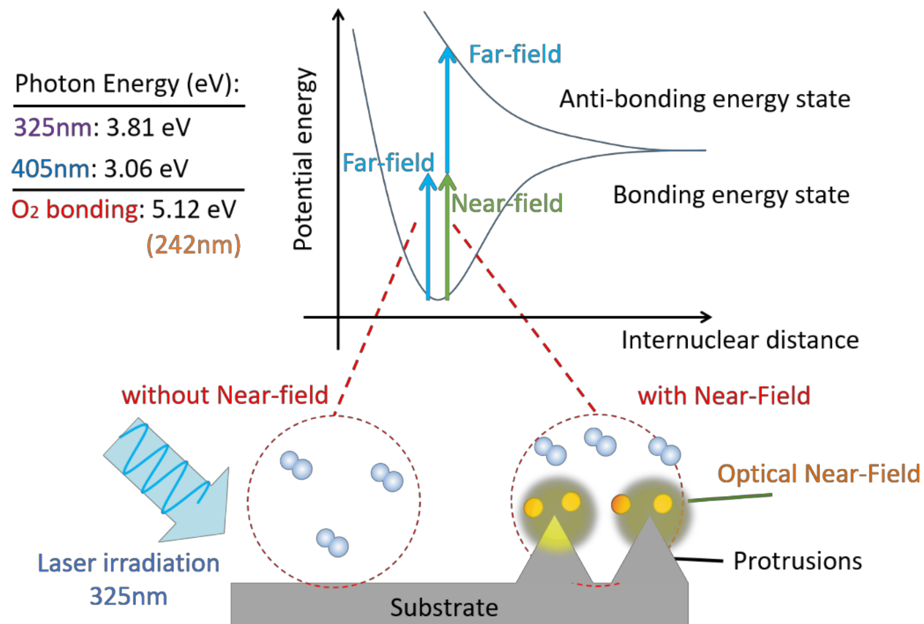

Figure 3.2. The photo-dissociation of O_2 by ONF [39].

Diagram of the photo-dissociation energy level of the O_2 molecule. The anti-bonding energy state can in theory only be reached with the additional energy of the localized ONFs (yellow sphere). (Reprinted with permission from M. Yamaguchi and K. Nobusada, Phys. Rev. B, 39, 195111 (2016). Copyright 2016 American Physical Society).

3.2 NF etching and other gases in air (besides O_2)

Since NF etching experiments are being performed under ambient conditions (room temperature, air, pressure, etc.) we need to consider the possibility of other common gases in air being a source for NF etching. As such, let us first look into the composition of our ambient atmosphere (Fig. 3.3).

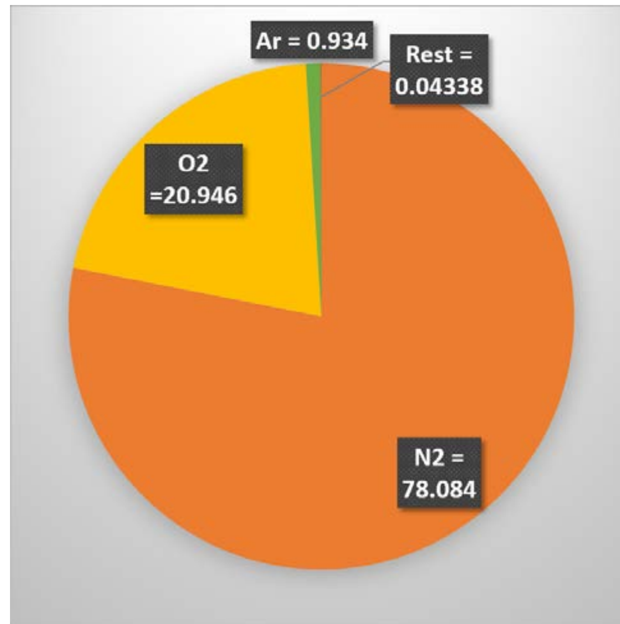

Figure 3.3. Atmospheric composition [40].

Diagram of the main constituents of Earth`s dry atmosphere.

Besides O2, we should also consider the impact of N_2 on our overall NF etching performance. Other possibly relevant gases (e.g. CO_2) are too sparse to be of further concern (Rest < 0.04338). N2 appears to have its dissociation energy at 9.765 eV (Fig. 3.4), and should thus be far outside of reach, considering the relatively low energy lasers being used for our NF experiments (typically 325nm He-Cd laser, 3.81 eV). We can thus conclude that O2 seems to be the only relevant atmospheric gas for the NF etching experiments presented in this paper.

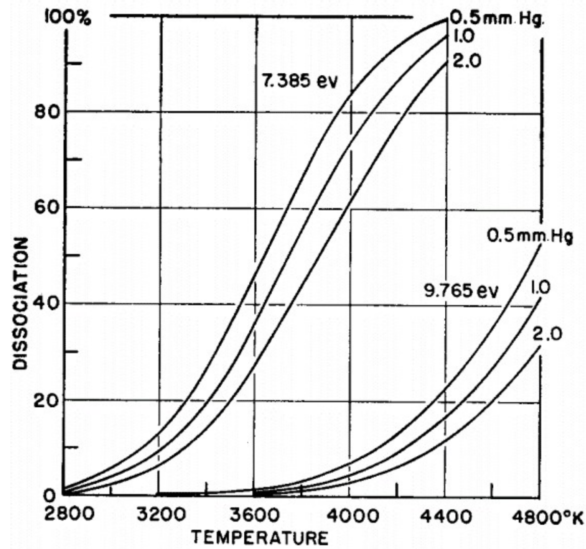

Figure 3.4. Theoretically calculated N_2 dissociation energies [41].

Dissociation curves for the two proposed values �$(N_2) = 7.385$ �V *and* �$(N_2) = 9.765$ �V*, where subsequent experiments hinted at the latter value being the most accurate one. (Reprinted with permission from J. M. Hendrie, J. Chem. Phys. 22, 1503 (1954). Copyright 1954 American Institute of Physics).*

3.3 NF caused dissociation of H_2O

Another potential contributor to NF etching could be the water contained in air. As such, let us first of all estimate the amount relative mass ratio of water (in form of humidity) to dry air (humidity excluded). Our experiments have been performed in Tokyo, where in summer relative humidity values peak at around 80%. When reading from the psychometric chart (Fig. 3.5) this would be equivalent to a humidity mass ratio (water/dry air) of approximately 1%. Moreover, outside of the summer, relative humidity values in Tokyo drop to around 50%. This would mean an even lower number of water molecules in ambient air. When considering that ambient air only consists of around 20% O_2, we obtain a H_20 (humidity) to O_2 ratio of approximately 5% at its peak, which means that humidity could have a small impact on NF etching.

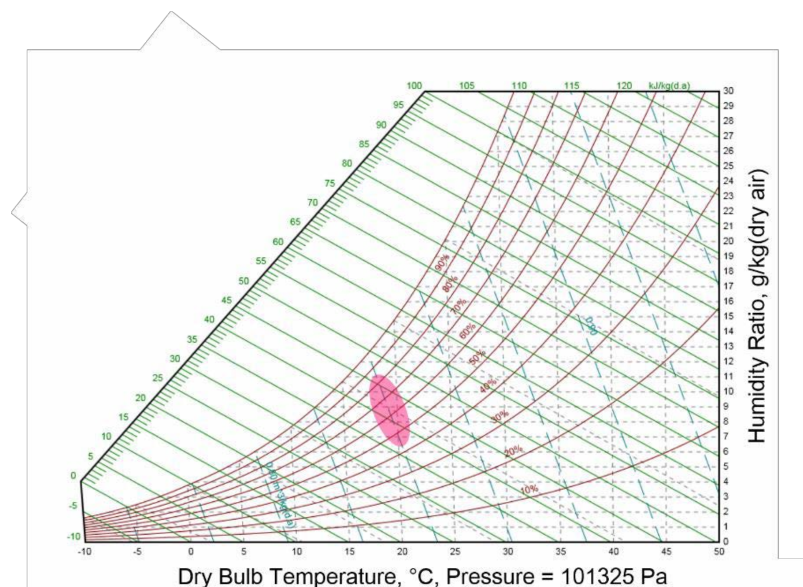

Figure 3.5. Psychrometric chart, sea-level pressure (101325 Pa) [42].

Pink area representing typical humidity values in Tokyo (between 50% and 80% relative humidity). Experiments are being performed under room temperature, 25 °C. (Reprinted with permission from © 2019 FlyCarpet Inc).

To understand whether H_2O can be photo-dissociated in our NF experiments, let us take a look at Fig. 3.6. P. Maksyutenko et al. in [43] have experimentally determined the dissociation energy of H_2O (i.e. bond energy of O-H in water) to be approximately 5.1 eV. More interestingly, they used a three-resonance laser excitation scheme to realize the O-H dissociation through vibrational, intermediate states. A direct photo-excitation of H_2O to its anti-bonding energy level would be forbidden under the common selection rules of the electric-dipole approximation. However, NF theory, due to its non-uniformity and large range of wavenumbers, cannot be described by the electric-dipole approximation model, and thus, although we do not use a three-resonance laser excitation scheme, we should be able to cause the photo-dissociation of H_2O with ONFs.

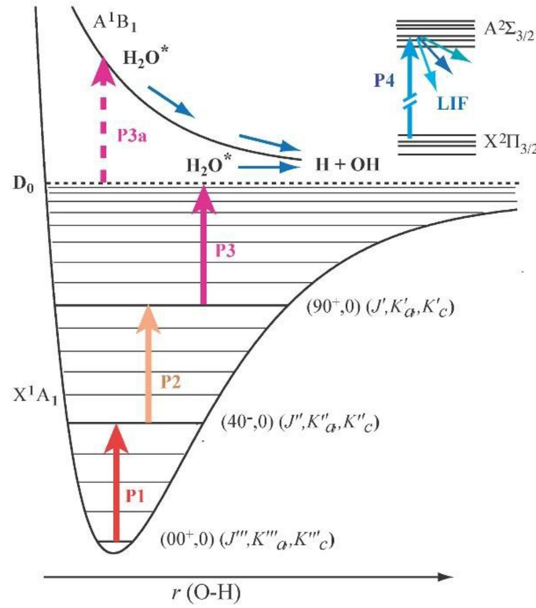

Figure 3.6. Dissociation energy of H_2O [43].

Triple-resonance laser excitation pulses were carefully chosen as to precisely excite the H_2O rotational-vibrational energy states. A process (direct photo-excitation) which is normally forbidden under the selection rules of the electric-dipole approximation model. (Reprinted with permission from [43]. Copyright 2006 American Institute of Physics).

3.4 NF etching on various materials

In the following we can see how NF etching has been shown to condition the surface of various materials, including silica substrates, gallium nitride (GaN) substrates as well as diamond substrates.

Fig. 3.7 shows the results of performing NF etching on a glass substrate. The far-field wavelength used for this experiment was 532 nm and the etching gas is assumed to be Cl_2, with a typical photo-dissociation wavelength of 400 nm. The experiment was performed under 100 Pa. The conclusion of the experiment was that nonadiabatic NF etching was able to drastically reduce the surface roughness of the silica substrate after 2 hours.

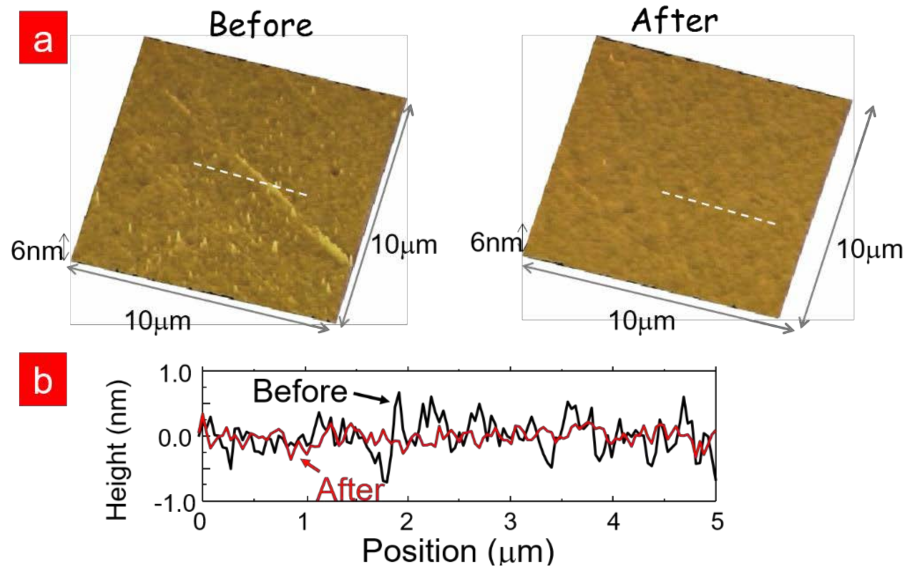

Figure 3.7. NF etching performed on a glass substrate [44].

a) NF etching performed on a glass substrate. The etching gas was hereby Cl_2. After NF etching image shows clear surface conditional improvements (smoother and less objects). (b) Cross-sectional profile indicating the surface change before (black) and after (red) NF etching. (Reprinted with permission from [44]. Copyright 2008 Springer-Verlag 2008.)

In Fig. 3.8 we can see NF etching performed on a single-crystalline diamond substrate grown under the high pressure and high temperature method. More specifically, the (111)-diamond substrate (Ib-type, absorption band edge of 3.02 eV) was prepared by cleaving of the bulk diamond. NF etching times for this experiment were 30 min and 60 min. The far-field wavelength used for this was 325 nm (He-Cd laser) and the etching agent are assumed to be ambient O_2 molecules

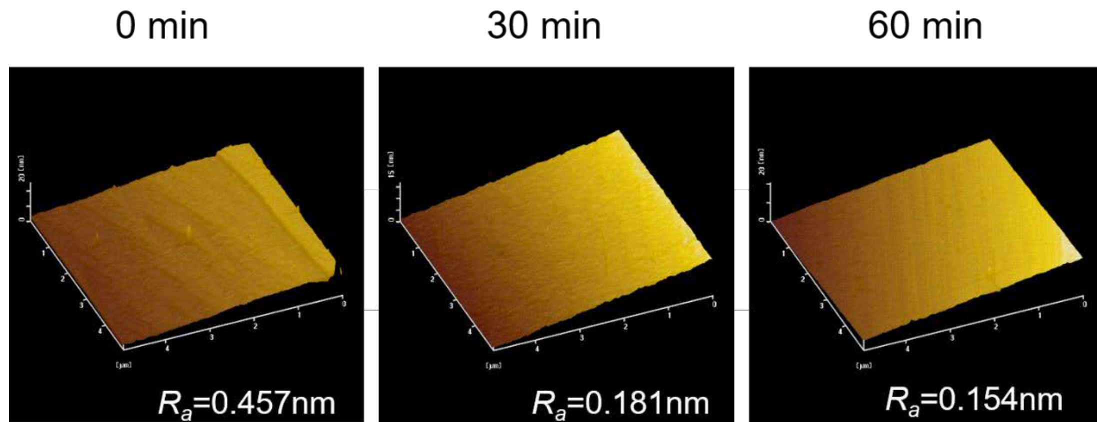

Figure 3.8. NF etching performed on a type Ib diamond substrate [45].

Change of surface roughness (R_a) over NF etching time performed on a type Ib diamond (111) substrate with a 5μm x 5μm scanning area. (Reprinted with permission from [45]. Copyright 2012 IOP Publishing.)

The conclusion of this experiment was that NF etching, performed with a 3.81 eV light source, was able to drastically reduce the surface roughness of the diamond substrate (from an initial R_a value of 0.457 nm to 0.181 nm after 30 min to 0.154 nm after 60 min of NF etching).

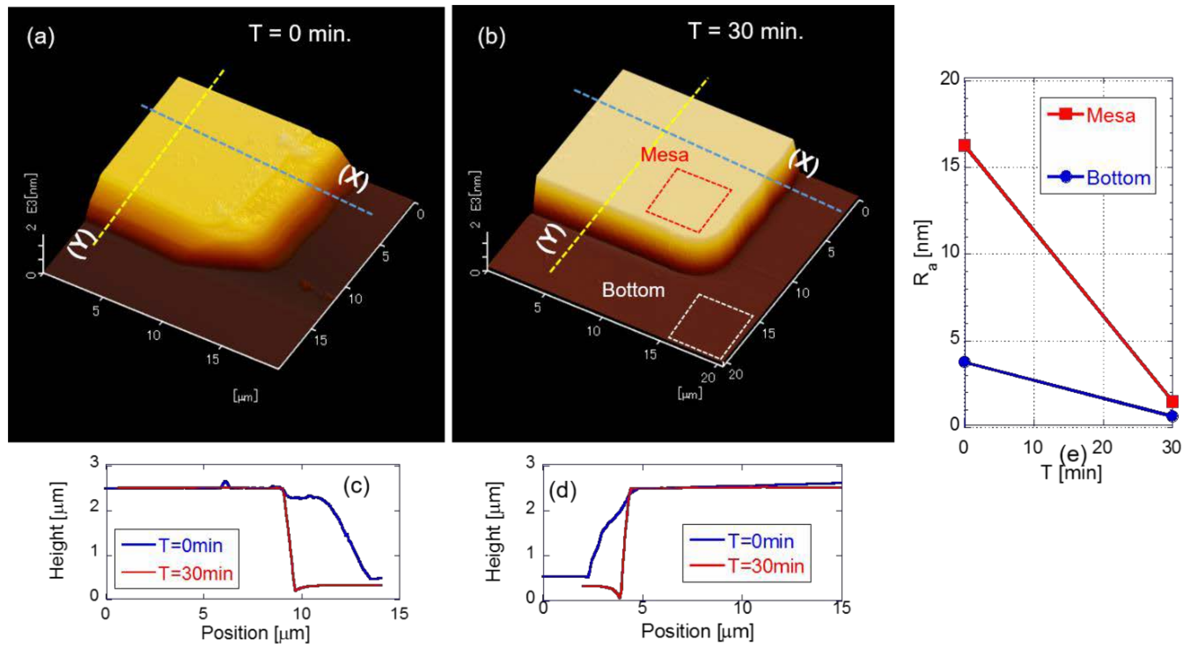

Figure 3.9. NF etching performed on a single crystal diamond substrate edge [46].

NF etching performed on a diamond substrate edge. The etching gas was hereby O_2. (a) Shows the diamond substrate edge before NF etching. (b) Shows the diamond substrate edge after 30 min of NF etching. (c) And (d) depict the cross-sectional diamond substrate edge profiles.(e) Comparing the roughness reduction between the mesa (red square) and bottom (white square) area.(Reprinted with permission from [46]. Copyright 2014 WILEY-VCH Verlag GmbH & Co. KGaA Weinheim.)

So far, both previous figures underline the effectiveness of NF etching in surface conditioning on various samples. Fig. 3.9 on the other hand also highlights the effectiveness of NF etching on three-dimensional surfaces, including convex, concave and periodic profiles. The NF etching experiment was performed again with the same He-Cd laser (325 nm) as the far-field light source and ambient O_2 molecules as the etching agent. The etching duration was 30 min. Figs. 3.9a and 3.9b indicate a clear change in the diamond structure after NF etching. The surface of the diamond does not only appear to be smoother, but also sharper across the edge. For a more precise view, Figs. 3.9c and 3.9d depict the

cross-sectional view of said edges. We can clearly see in both cross-sectional views that after 30 min of NF etching the edge has been sharpened immensely.

The conclusion of the NF etching experiment on the diamond substrate edge is that NF etching is not only able to modify flat surfaces, but also able to condition three-dimensional structures. Furthermore, the dependency of NF-generations on the amount of surface protrusions seems to be further highlighted when looking at Fig. 3.9(e). In it we see that mesa roughness was reduced in a higher rate than the bottom mesa. The reason for this seems to be the fact that the diamond mesa has a higher initial roughness value (and thus higher number of protrusions) than the diamond bottom.

Overall, past experiments have shown that NF etching can change surface conditions of various samples, mostly in terms of a reduced surface roughness. More interestingly, NF etching also appears to be able to change the shape of a three-dimensional structure (i.e. thinning sample by etching side-walls). Because NF etching rates should be strongly dependent on the amount of protrusions, we assume that during the sample fabrication processes (e.g. top-down), the sides are often left with a lower resolution, and thus higher roughness, than the center part of the sample. As such it would explain why NF etching appears to strongly interact with the side-walls (Fig. 3.9) while the height of the sample appears to be visibly unchanged. To confirm this theory, I would like to repeat the experiments from this chapter with a more suitable sample; organic chemically amplified photoresists (CAR). CAR structures (in our case horizontal line/trench patterns) have been produced by a top-down method (lithography) as well, and I thus suspect similarly rough side-walls (compared to its top side mesa) as with the diamond substrate edge. Furthermore, the organic photoresists, due to their lower mass-density and higher

porosity, are easier to be etched than most inorganic, crystalline materials. This would make them a more suitable NF etching indicator (easier AFM read-out), combined with the fact that reducing photoresist roughness values is of great interest in the high-end semiconductor industry (extreme ultra-violet (EUV) lithography). Through the experiments in the next chapter I hope to verify that NF etching can be used to realize three-dimensional structural change in target samples.

Chapter 4.

Reducing organic photoresist surface roughness

4.1 Background

Photoresists are the fundamental component in the lithography process for the creation of new devices. The so called RLS trade-off [47] states that the devices created by lithography have their resolution, line edge roughness and sensitivity in a trade-off relation. Especially in the face of increasing demand for smaller and smaller electrical components (below the 10 nm mark), it becomes crucial to ensure that the line edge roughness of the photoresists can stay small enough in order to avoid scattering losses of the nanoscale devices.

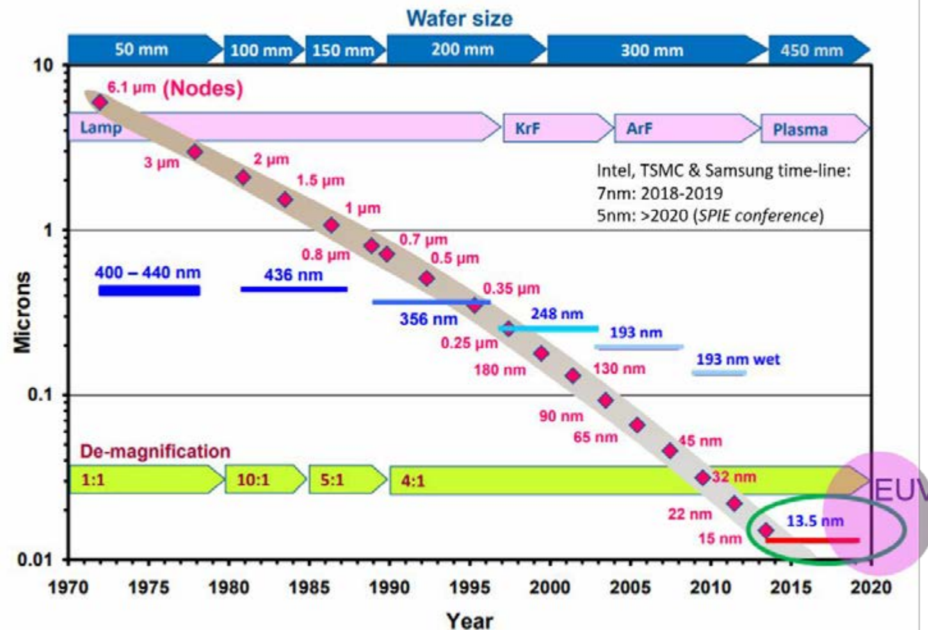

Figure 4.1. Wafer size time-chart [48].

Evolution and expected decrease of wafer sizes over time. Intel, TSMC & Samsung expecting 5nm nodes by 2020. (Reprinted with permission from [48]. Copyright 2012 SEMATECH Inc.)

Giving the current speed of size reduction in the high-end semiconductor industry, we are expected to reach node sizes of 5nm by the year 2020 [49] (Fig. 4.2). Sub 10 nm lithography relies on the Extreme Ultra-Violet (EUV) lithography technology. However EUV lithography suffers from a low output photon power [50] and as a compensation requires resists with high sensitivity. Due to their extremely high sensitivity [51], organic CAR are looking to become the EUV industrial standard as well.

EUVL extension concerns (2017) EUVL

2014	2015	2016	2017
1. Reliable source operation with > 75% availability	1. Reliable source operation with > 85% availability	1. Reliable source operation with > 85% availability	1. Resist resolution, stochastics, and sensitivity met simultaneously
2. Resist resolution, sensitivity & LER met simultaneously	2. Resist resolution, sensitivity & LER met simultaneously	2. Resist resolution, sensitivity & LER met simultaneously	2. Reliable source operation with > 90% availability
3. Mask yield & defect inspection/review infrastructure	3. Mask yield & defect inspection/review infrastructure	3. Keeping mask defect free	3. Keeping mask defect free
3. Keeping mask defect free	4. Keeping mask defect free	4. Mask yield & defect inspection/review infrastructure	4. Mask yield & defect inspection/review infrastructure

© IMEC

Figure 4.2. EUVL extension concerns (post 2017) [52].

Time-line of main problems for future EUV lithography. Current focus one resists with high resolution, reliable stochastics (errors, roughness) and high sensitivity. (Reptrinted with permission from [52]. Copyright © 2019 eMedia Asia Ltd.)

Unfortunately, organic CAR come with some great limitations, which is mainly the previously mentioned RLS trade-off relation. Since these organic CAR are multi-component materials (Fig. 4.3), they are prone to inhomogeneities and fluctuations. This means that organic CAR are especially susceptible to stochastic effects (i.e. noise/fluctuations) in low dimension and high resolution environments.

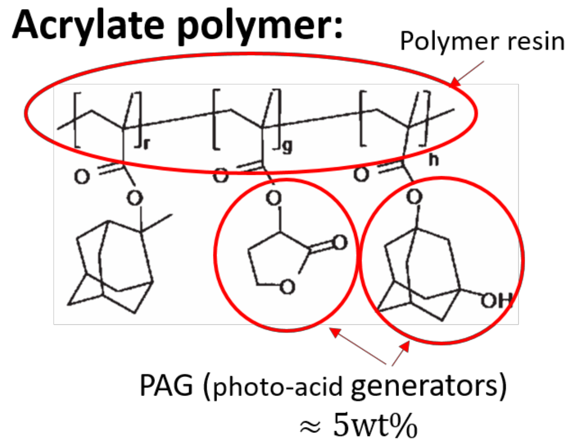

Figure 4.3. Chemical composition of organic CAR [53].

Main component of PR being constituted of polymer resin. Functional groups, e.g. photo-acid generators, stabilizers, surfactants, etc.) connected to the resin.

As can be seen in Fig. 4.3, the main component of CARs is there Acrylic polymer resin. Connected to the resins are normally various functional groups (such as photo-acid generators, stabilizers, surfactants, etc.) depending on the exact application of the resist. The mass density of organic photoresists is approximately 0.89 g/cm^3, which is significantly lower to e.g. the silicon, 2.32 g/cm^3, or diamond, 3.51 g/cm^3, mass densities. These low mass densities and feeble structures of organic photoresists make them a great candidate for NF etching as well, since it should be easier to see the etching effects as compared to more robust materials, such as diamonds.

The semiconductor industry often ends up focusing on two out of the three important parameters (RLS) (Fig. 4.4), often dictated by the lowest cost or highest availability on mass production scales.

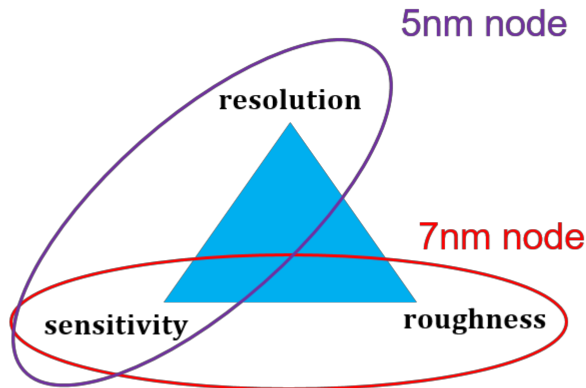

Figure 4.4. RLS tradeoff for EUV [54].

RLS tradeoff relationship between photoresist resolution, sensitivity and roughness for current high-end EUV lithography resists. (Reprinted with permission from [54]. Copyright 2018 Society of Photo-Optical Instrumentation Engineeers (SPIE).)

More precisely, the resolution of lithography is defined by the following equation:

$$CD = k_1 \frac{\lambda}{NA} \quad (4.1)$$

CD refers to the critical dimension of the system. The critical dimension is normally also written as two times the half-pitch (of the semiconductor device). The k_1 factor equates to process-related factors of the experimental setup, λ being the wavelength used

for lithography and NA represents the value of the numerical aperture of the lens.

Sensitivity [mJ/cm^2] on the other hand describes the amount of energy which is needed to generate a feature in the photoresist layer. A high sensitivity is especially important in EUV lithography where photon numbers are generally quite low.

The roughness of a photoresist is generally represented by its line-edge roughness (LER) value. The definition of the LER will be explained in more detailed in the following segment.

4.2 LER and other roughness values of photoresists

In Fig. 4.5 we can see how the LER and line width roughness (LWR) are usually being obtained from the resist profile.

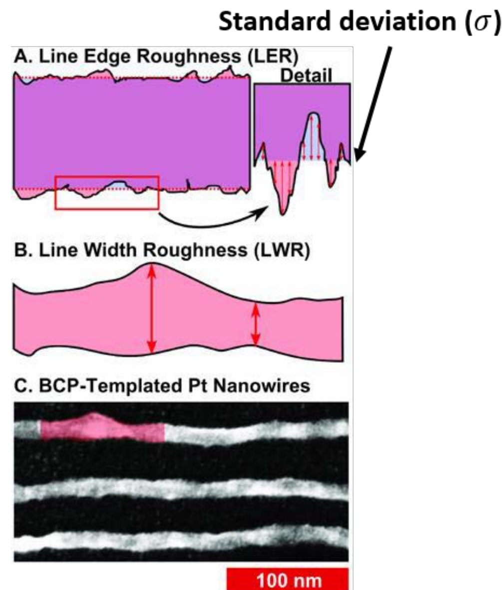

Figure 4.5. Evaluation of LER and LWR [55].

A. Calculation of LER by standard deviation of line edge profile. The LER is being calculated as 3 times the standard deviation. B. LWR evaluated from the variation of width of the photoresist. C. SEM obtained photoresist image showing Pt nanowires on Si wafer. (Reprinted with permission from [55].)

The LER value is obtained by observing the sides of the resist (perpendicular top-down view) and calculating their roughness (standard deviation) as can be seen in the red square in the above image. Unlike the LER, the LWR value is being obtained by concentrating on the spatial width of the resists.

I like to point out that the roughness values examined in NF etching experiments are also defined through the standard deviation of a specific area. Hence I believe that NF etching should be very well able to improve LER values of photoresists as well.

In order to understand why the roughness of resists play an important role in the final device performance, let us look at Fig. 4.6.

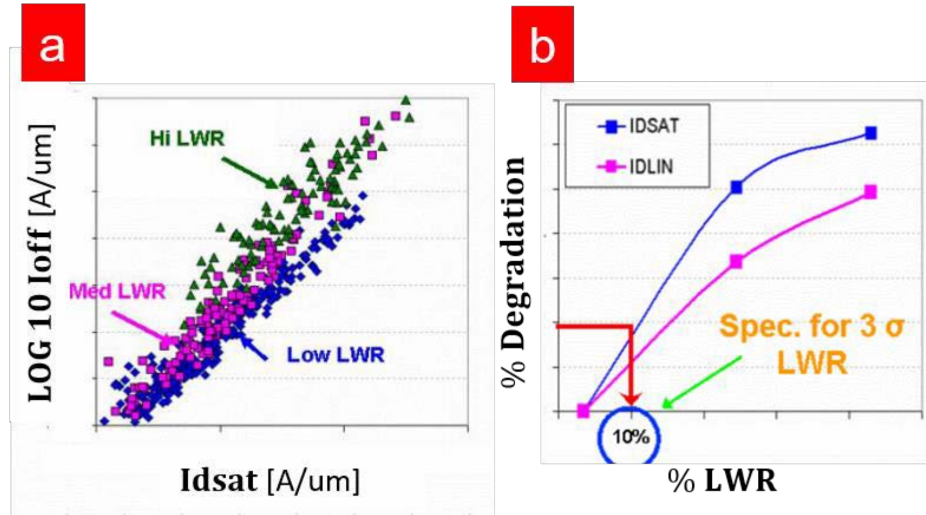

Figure 4.6. Negative impact of LWR on device performance [56].

Impact of LWR on Intel 65nm transistor performance. (a) High LWR showing strong exponentially increasing off-current/drive-current relationship. (b) transistor drive-current degradation due to LWR. (Reprinted with permission from [56]. Copyright 2007 Society of Photo-Optical Instrumentation Engineeers (SPIE).)

Fig. 4.6 shows the impact of high LWR values on the device performance. More specifically, in this case the performance of Intel`s 65nm node transistor was being observed. We can see in Fig. 4.6a that the off-current increases exponentially in respect to the drive-currents for high LWR values. In Fig. 4.6b we see that both drive currents degrade by over 2% for 3 σ LWR = 0.1 CD.

Besides the importance of minimizing LER and LWR values, device performance can also suffer through bridge and half-bridge building (due to local electric gradients causing leakage).

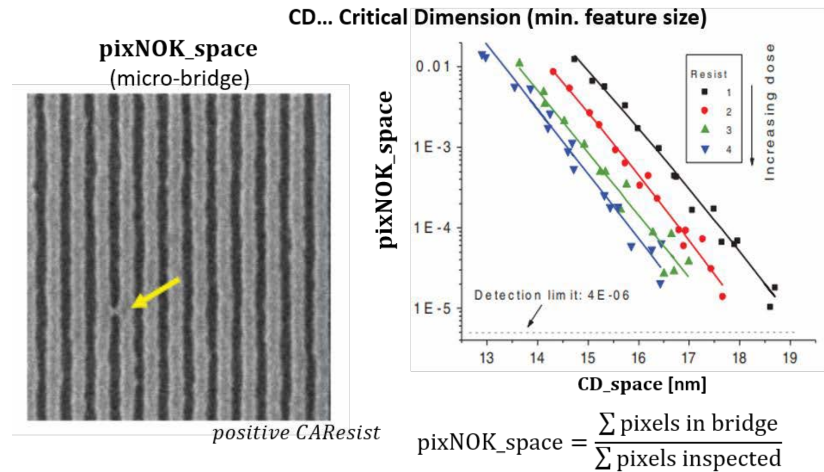

Figure 4.7. Relation between PR errors (bridges) and CD [57].

(left) Image showing bridges between the single wire structures (yellow arrow). (right) Increase of erroneous structures (e.g. full- and half-bridges) with decreasing CD values. (Reprinted with permission from [57]. Copyright 2017 Society of Photo-Optical Instrumentation Engineers (SPIE)).

Full and half-bridges are a great concern to future lithography processes with low CD. In Fig. 4.7 the proportion of bridges (sum of bridge pixels over total pixel sum) has been analyzed over decreasing CD values. We find that generally the number of bridges over healthy structures increases linearly with the reduction of CD values. .

4.3 NF etching on photoresists

In this chapter I would like to apply NF etching with the goal to improve the surface roughness of the photoresists, as well as control the structure width in order to tackle bridging problems. I believe that NF etching can improve the surface condition (roughness) of the photoresists due to the fact that NF etching has been previously proven effective in smoothening various kinds of materials and surfaces. Also, the experiments on the diamond substrate edge have shown that NF etching can reduce structural width, which would be

interesting if repeated successfully on organic photoresists. Previous research suggests that the NF etching has already proven to be successful in reducing surface roughness and producing atomically flat surfaces in a wide range of components, such as GaN, as well as flat and shaped glass and diamond [38,58], while also showing that it can be effective on flat as well as patterned surfaces.

The fundamental theory behind the NF etching suggests that the etching is caused by radicalized gas atoms, which in ambient conditions are most often oxygen atoms. More concretely, these gas molecules can be dissociated under illumination at a specific wavelength (for O_2 molecules 5.12 eV) [59], with the resulting reactive oxygen interacting with its immediate surrounding. If the material is chosen properly, as well as the etching gas agent, the reaction of the radical gas atoms with the sample surface will result in effective etching of the sample surface, as the radical gas atoms interact (in form of etching) and afterwards re-combine themselves with the etched atoms resulting in new gas molecules.

Exciting the O_2 molecules with a photon energy of 5.12 eV (242 nm) will result in direct photo-dissociation, which on the other hand should result in conventional adiabatic etching of the sample surface. However, NF etching does not rely on the conventional photo-dissociation of the O_2 molecule by an incident photon energy of 5.12 eV but instead relies on the localized ONFs to ultimately enable the photo-dissociation of the O_2 molecules. For that reason, we should use a laser energy with a higher wavelength than 242 nm (5.12 eV), in order to avoid direct dissociation of the gas molecules. In this case, we decided to use the etching laser wavelength of 325 nm, whose photon energy is below the O_2`s 5.12 eV. Current research in NF theory explains that localized ONFs due to its

non-uniformity can cause various novel NF limited phenomena, such as two-step excitations by making use of intermediate states in molecules which are normally forbidden under the traditional dipole approximation. These dipole-forbidden transitions can be ignored when looking at ONFs instead of conventional far-field systems.

To sum up, although the incident laser photon wavelength (325 nm) is below the photo-dissociation wavelength of O_2 molecules (242 nm), owing to dipole-forbidden vibrational state transitions of localized NF photons, we assume that the photo-dissociation of O_2 molecules can still be caused. In addition, these localized ONFs are believed to be primarily present within protrusion (sub-wavelength systems) of the sample surface, when excited by a far-field light source. Therefore, the photo-dissociation of the O_2 molecules and its resulting etching of the sample surface, occur mainly at places with high protrusion densities. While the exact physical explanation for the ONF related energy up-conversion is yet to be found, current NF research hints at the possibility that energy up-conversion could be due to two-photon absorption, rather than the absorption of single photons, despite with much lower probability [60].

For this experiment we used an EPIC 2096 ArF photo-resist (organic), which is chemically amplified (CAR), and has its inherent photo-reactiveness to photons around 193 nm wavelength [61]. One reason why we chose this material for our to-be-etched sample is that they are first of all quite easily obtainable, and also because organic photoresists are commonly used for the production of nanoscale electrical components. As mentioned previously, having a RLS trade-off relation means that lithography with very fine resolution will result in a worse SR, so in this experiment we will try to improve the surface roughness of the organic photoresists with NF etching. Improving the SR of the

photoresist during lithography would mean that the semiconductor end-product would be improved as well. Another reason is that with this experiment we will be able to deepen our understanding of NF etching, as organic photoresists (due to its porosity) can probably be used more easily as an NF-etching indicator, compared to the sturdier inorganic materials. Also our etching technique hasn't been performed on organic photoresists yet.

4.4 Experimental

For this experiment, using interference lithography, the photoresists, EPIC 2096 ArF Photoresist (positive-type), were prepared (Fig. 4.8).

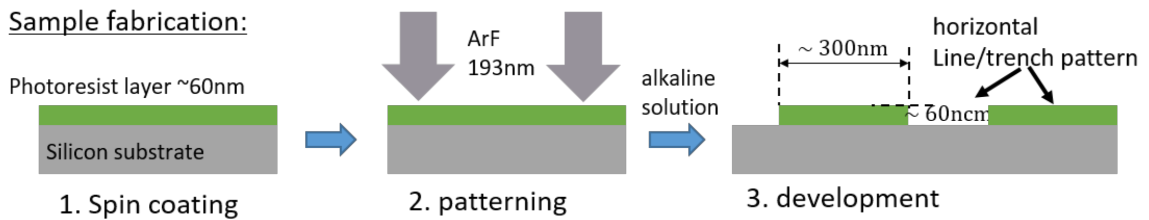

Figure 4.8. Organic photoresist fabrication sequence.

Photoresist layer spin coated on top of silicon substrate. Patterning performed via an ArF laser light source. Subsequent development of photoresist by alkaline solution.

Their typical absorption spectrum edges at around 310 nm. This chemically amplified resist was specifically chosen as to have an absorption edge below the 325 nm wavelength, which will be used (alongside 405 nm) as the incident far-field light source, in order to avoid a direct photochemical reaction of the photoresist with the light source. As the incident continuous-wave, also called CW, far-field light source we used two different lasers: Firstly, a helium-cadmium (He-Cd) laser with a 325 nm wavelength and photon energy of 3.81 eV, and secondly a GaN laser with a 405 nm wavelength and photon energy of 3.06 eV. The He-Cd laser has a power density of 0.8 W/cm^2 and the GaN laser

has an overall excitation power of 39 mW. As mentioned in previous chapters, we chose two lasers whose photon energy lays well below the photo-dissociation energy of the O_2 molecule, so that we may avoid normal adiabatic etching. In case of the He-Cd laser, the emission line for wavelengths outside 325 nm is by a factor of 10^{-4} times lower than 325 nm, and thus we can exclude the possibility that other wavelengths were causing the O_2 dissociation.

The exposure time of the photoresist to the far-field light sources, and thus the NF etching times, were up to two hours long (three intervals within 0-120 min). In case of the NF etching measurement performed under vacuum conditions, before exposure to the lasers, the sample was set up inside a hermetically sealed vacuum box. By the so-called purification of the air inside the vacuum box, the oxygen density was below the tens of ppb mark. With the purification process, we first of all completely remove the air inside the vacuum box, and afterwards replace it with N_2 gas (until the initial air pressure inside the vacuum box has been restored). This was repeated for ten times, meaning that the end result is a low-oxygen air within the vacuum box. Note that there are approximately 5 ppb O_2 molecules inside the N_2 tank itself, so removing O_2 completely using this method is impossible. The NF etching was performed while leaving the sample within this low-oxygen environment within the vacuum box. The vacuum box was carefully selected as to be transparent for both of our laser wavelengths.

In general, after NF etching (more specifically, for the intervals 0, 60 and 120 min.) we used an atomic force microscope, also simply called AFM, produced by Hitachi-Hitech-Science Corp., in order to check the effectiveness of NF etching by examining the photoresists (Fig. 4.9). We usually observe 4 μm areas, and the resolution is typically 256

× 256. Our AFM`s Sample-intelligent-scan mode, further improves the AFM imaging by strengthening image contrasts. Furthermore, masking and tilt correction features were used to further improve the measurement precision. Most important parameters, such as SR and cross-sectional values, mentioned in the next part, were all obtained with the AFM inbuilt software.

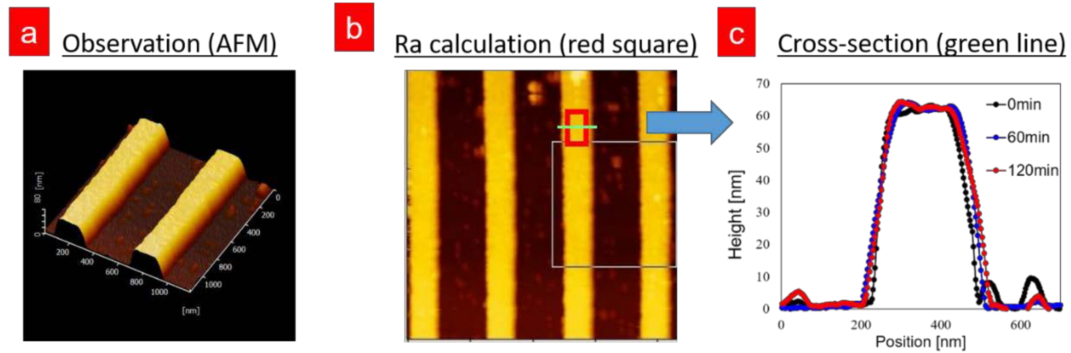

Figure 4.9. Photoresist evaluation sequence [61].

(a) AFM measurement of organic photoresists (b) top-down image of photoresist. Top of photoresists evaluated for surface roughness (red square). 4 values obtained per measurement point. (c) cross-sectional view of photoresists (green line in (b)). (Reprinted with permission from F. Brandenburg et al. Beilstein J. Nanotechnol. 8, 784-788 (2017). Copyright 2017 Brandenburg et al.; licensee Beilstein-Institut.).

Fig. 4.9 depicts the sequence order of the photoresist evaluation. First of all, the photoresists were observed under the AFM (Fig. 4.9a). Next (Fig. 4.9b), from top-down view, the surface roughness was obtained for a specific area (red square). Also, cross-sectional images of the photoresists were obtained (green line) as can be seen in Fig. 4.9c.

FDTD Simulations were obtained from the Poynting for Optics (Fujitsu).

4.5 Results and Discussion

Before checking the photoresist for SR and cross-sectional values, we obtained general images of its structure for before and after NF etching (Fig. 4.10). Figure 4.10a is the initial shape of our photoresist, without applying any NF etching. In Fig. 4.10b we can see the shape of our photoresist after applying NF etching with the He-Cd laser. The NF etching results for 405 nm can be found in Fig. 4.10c, showing the photoresist substrate surface before NF etching, and Fig. 4.10d, showing the photoresist substrate surface after NF etching. As always, we performed the experiment under ambient condition, since the etching component is believed to be originating from the O_2 molecules. When taking a look at our figures (Figs. 4.10a, b) it becomes apparent how the width of the photoresists has been reduced after applying NF etching with 325 nm. However, when checking the AFM images for the effectiveness of the 405 nm laser source (Figs. 4.10c, d) we can notice that there seems to be no big change in the shape of the structure (the opposite to 325 nm). The next step for the 405 nm experiment was to check and compare the surface of the photoresist from closer up (Figs. 4.10e and 4.10f), as indicated by the white square in seen in Figs. 4.10b and 4.10c. What we can notice in the zoomed up images, although rather subtle, is the change of the smoothness of the samples after applying our technique. More specifically we seem to have to greatest change in smoothness with the 405 nm laser source.

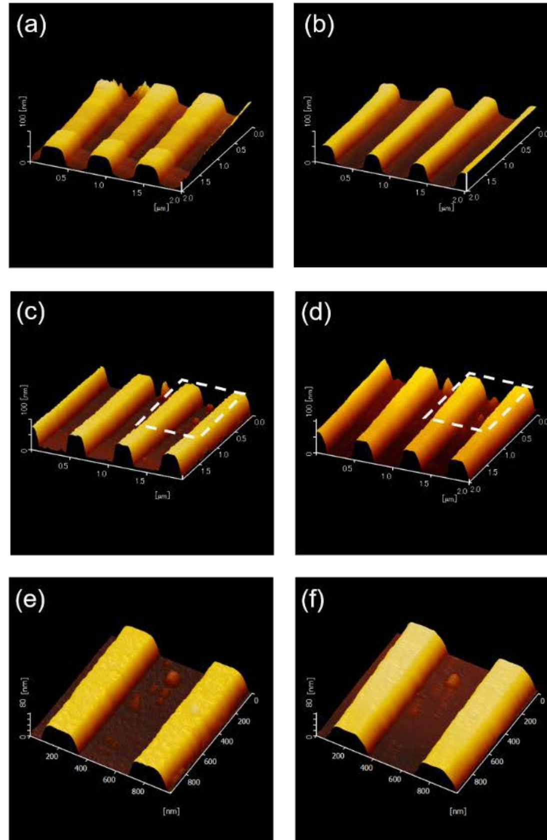

Figure 4.10. 3D AFM images of photoresists before and after NF etching [61].

3D-AFM images of the photoresist. Initial state of the photoresist (a) as well as its state after 2h of illuminating it with the 325 nm laser source (b). In accordance to (a) and (b), (c) and (d) show the states of the sample after illumination with the 405 nm laser source. (e) and (f) showing enhanced images of the white area depicted in (c) and (d), respectively. (Reprinted with permission from F. Brandenburg et al. Beilstein J. Nanotechnol. 8, 784-788 (2017). Copyright 2017 Brandenburg et al.; licensee Beilstein-Institut.)

Figure 4.10 only gives us an approximate estimation of the extent of the NF etching effect on parameters such as surface smoothness and overall structural shape. In order to have a more detailed view, we should look at Fig. 4.11, which lets us understand more clearly how our technique changes the profile of the samples. Figure 4.11a illustrates the structural change induced by the 325 nm light source. What we can immediately see is a drastic reduction of the overall photoresist width over NF etching time. The photoresist diameter of approximately 400 nm for before NF etching has been reduced down to about

250 nm diameter width for the after 120 NF etching time. Fig. 4.11b in principal repeats this measurement, but this time for the 405 nm light source. What we can see here is that there appears to be no change of the structural shape of the photoresists with increasing NF etching duration. Interestingly enough, although both laser sources are too weak to cause direct O_2 dissociation, it seems that they somewhat influence the sample shape, especially when considering the 325 nm results. However, we still remember that the surface texture of the photoresists appeared to have changed when looking at Figs. 4.10c-f, so for now we shouldn't exclude to possibility of photoresist etching caused by the 405 nm light source. We need to take note that the NF caused photo-dissociation of the O_2 molecules is likely a combination of the conventional far-field photon from the light source (325 nm or 405 nm) and the locally induced ONFs in sub-wavelength objects on the photoresist surface. While we don't know the exact phenomena which is attributing to the photo-dissociation from the NF side, i.e. whether it is due to multiphoton absorption, second harmonic generations, etc., we can argue that since 325 nm is much closer to the direct dissociation wavelength 242 nm from an energy perspective, that naturally 325 nm should consequently have a higher NF etching ratio than the GaN laser (405 nm).

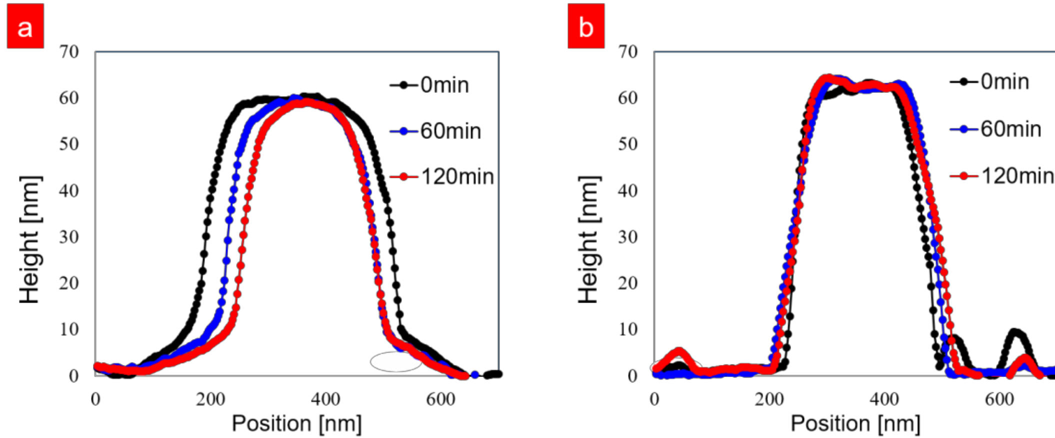

Figure 4.11. Cross-sectional image of photoresist during NF etching [61].

Cross sectional evaluation of the photoresist shapes for 0h (black), 1h (blue) and 2h (red) of etching. Left figure (a) representing the results for 325 nm and the right figure representing the results for 405 nm. (Reprinted with permission from F. Brandenburg et al. Beilstein J. Nanotechnol. 8, 784-788 (2017). Copyright 2017 Brandenburg et al.; licensee Beilstein-Institut.)

What seems further interesting is the fact that the photoresist side-walls were etched but seemingly the photoresist top not. To understand this point more clearly, the same experiment has been simulated (Fig. 4.12) in order to understand the distribution of the electric field along the photoresist surface. Just as in the real experiment, the lasers were linearly polarized as well. We calculate the peak values of the electric field intensity at the photoresist side-walls to be ~2860 mV/m. This is only slightly more than the electric field intensity at the top of the photoresist (~1720 mV/m), which equals a factor of ~1.66. From the results we calculate the non-uniformity |dE/dr|. The value of |dE/dr| at center of the resist and the edge of the resist were 0.322 mV/m^2 and 1140 mV/m^2, respectively, meaning that non-uniformity at the edge of the resist has 3540 times large and resulted in higher etching rate in the side wall. In addition to that, the fact that in Fig. 4.11 for visualization purposes the photoresists have been significantly stretched along their height-axis, leads us

to assume that ONFs are more commonly induced at the side-walls of the photoresists. A further factor could be that the photoresist material (multi-component based) have due to gravitational compression have a higher density in the z-direction (height-axis) than the x-direction. Lastly, due to the nature of their manufacturing process (lithography), the sides most likely have higher roughness values than the top of the photoresist, meaning that ONFs would be induced at a higher rate at the side-walls as well.

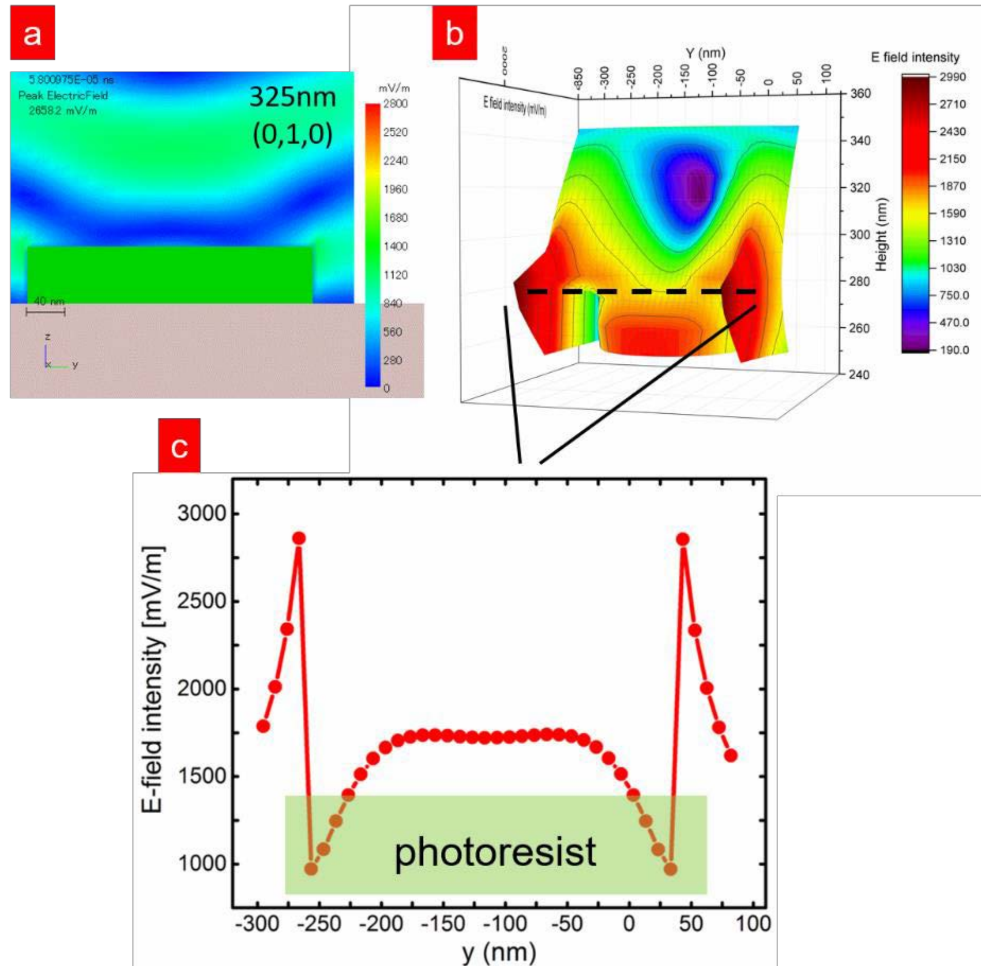

Figure 4.12. Simulation of photoresist exposure to 325-nm laser.

Simulation based on linearly polarized 325 nm CW laser source (perpendicularly from above photoresist surface, y-polarized) showing distribution of electric field along the photoresist surface. The minimum grid size was hereby 1 nm (a) Showing photoresist (green rectangle) on top of silicon substrate (grey area) and the E-field intensity distribution from the incoming light wave. (b) 3D surface heatmap of the E-field intensity around the photoresist, showing high intensity at the side walls. (c) Cross-section profile of E-field intensity (black line, see (b)) showing clearly that E-field intensity is stronger at the photoresist side-walls than on the top of the resist.

For a more precise analysis of the surface smoothening of the photoresists by each laser, I have evaluated the surface change of the photoresists using the AFM software (Fig. 4.13). So what we can see in the following graph (Fig. 4.13a) is that both lasers were clearly able to improve the surface smoothness of the photoresists over the 120 min duration.

Please note that we have a variance in the initial surface roughness across photoresist samples. This is simply due to the nature of their fabrication, as well as limitations to the AFM analysis capabilities. That also explains why starting SR value in Fig. 4.13a are so different between the 325 nm and the 405 nm samples. This might make it less practical to directly compare the effectiveness of NF etching between the 325 nm and the 405 nm laser sources. However, we can definitely conclude that both lasers were successful in smoothening the sample. Experiments with 405 nm appear to have improved the surface smoothness at a greater ratio than the 325 nm one, however we should also consider that it had a higher initial SR value, meaning that it could have had a stronger presence of localized ONFs along its surface than the 325 nm sample. At the same time, we need to keep in mind that Fig. 4.11 showed that NF etching with 325 nm was drastically changing the cross-sectional shape of the photoresist, meaning that etching took place on a high rate. Since atom layers were removed at such a great rate for the 325 nm experiment, it could have been difficult to realize finer surface etching of the photoresists. The 405 nm experiment on the other hand showed little to no cross-sectional change of the photoresists in Fig. 4.11b, meaning that etching took place on a smaller rate. We could argue that due to its lower energy, the 405 nm experiment etched the samples at a lower rate. This probably explains why it resulted in an overall better smoothening of the photoresist (compared to 325 nm, who etched at a much higher ratio). The 405 nm experiment most likely only had effect on the outmost layers of the sample, hence resulting in their very low surface roughness, while 325 nm removed layer by layer with its higher etching ratio. Again, we should mention that for future experiments it would be nice to have similar initial SR values amongst all samples.

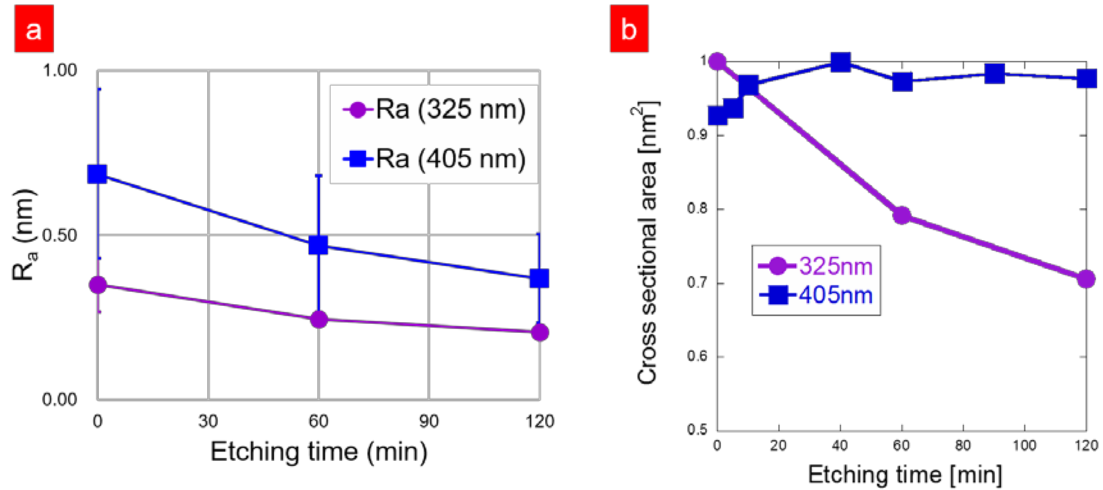

Figure 4.13. Surface roughness evaluation over NF etching time [61].

(a) Surface roughness (R_a) evaluation over a total period of 2h. Blue line representing the results for 405nm and purple line representing the results for 325nm. The total removed area can be seen in (b). (Reprinted with permission from F. Brandenburg et al. Beilstein J. Nanotechnol. 8, 784-788 (2017). Copyright 2017 Brandenburg et al.; licensee Beilstein-Institut.)

What we can also see in Fig. 4.11 and Fig. 4.13 is that the etching effect appears to be saturating with increasing time. It's quite possible that with increasing NF etching duration, the amount of sub-wavelength objects on the sample surface decreases, meaning that localized ONF are occurring on a lower rate. This saturation has also been observed in previous NF-etching experiments, for various materials and shapes.

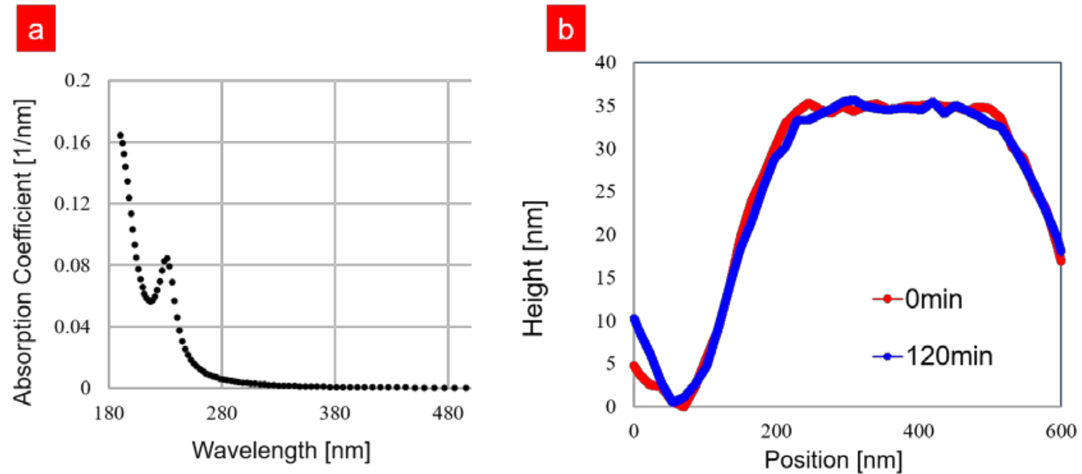

Figure 4.14. Inherent organic photoresist absorption spectrum [61].

(a) The absorption spectrum of the EPIC 2096 ArF photoresists, with its main absorption edge at around 250 nm. (b) 325 nm experiment repeated with vacuum conditions, showing that O_2 is integral to the etching effect. (Reprinted with permission from F. Brandenburg et al. Beilstein J. Nanotechnol. 8, 784-788 (2017). Copyright 2017 Brandenburg et al.; licensee Beilstein-Institut.)

In Fig. 4.14a we can see that 325 nm and 405 nm are far outside the absorption edge of the photoresists, meaning that their natural sensitivity to ultra-violet light can safely be excluded as a reason for the structural change. Furthermore, to check the importance of O_2 molecules, I repeated the same NF etching experiment (325 nm), but this time under a low-oxygen (near-vacuum) environment. The results can be seen in Fig. 4.14b. What we can immediately see is that the drastic cross-sectional width loss of Fig. 4.11a was not replicated. Fig. 4.14b underlines that O_2 is an integral component of the etching effect of the photoresists. We conclude that other explanations for the structural change of the photoresists (such as an inherent UV sensitivity of the resists or silicon substrate heating due to laser) can be safely excluded with the results shown in Fig. 4.14.

To briefly sum this chapter up, we were able to control the structural width of the photoresists when using the 325-nm laser source. Hence NF etching could be promising as a counter-measure for reducing the amount of full and half-bridges in the increasingly smaller CD values in the high-end semiconductor industry (Fig. 4.15).

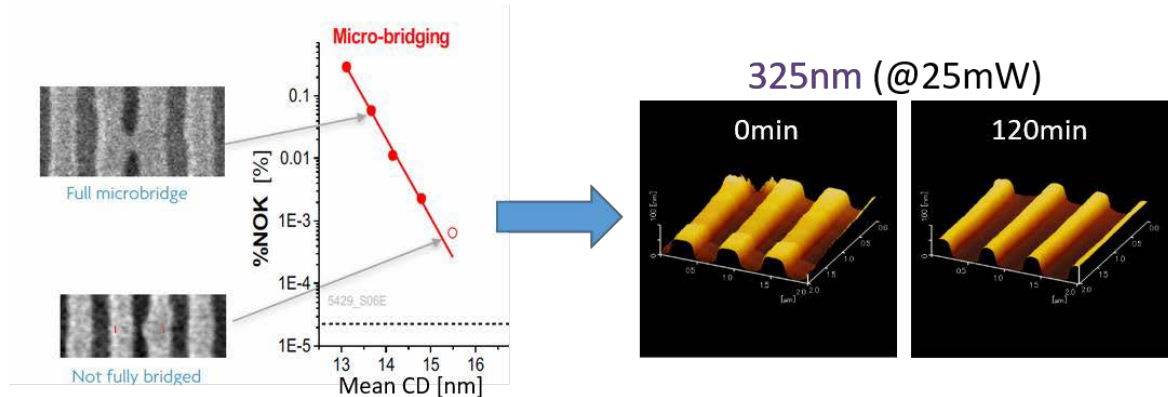

Figure 4.15. Potentially reducing full- and half-bridges with NF etching [62].

(left) images showing that the proportion of bridge defects increases with decreasing CD values. (right) Structural width control with 325nm laser. (Reprinted with permission from [62]. Copyright 2018 Society of Photo-Optical Instrumentation Engineeers (SPIE).)

Furthermore, both lasers (325nm and 405nm) were able to reduce the roughness value at the top of the photoresists. The initial roughness values for the 325-nm and 405-nm experiments were different, so a direct comparison between them should be avoided. However, both seem effective in reducing roughness values.

Since the LER value is, just like the roughness value in our experiments, obtained by the roughness standard deviation, our experiments serve only as an indirect proof of the effectiveness of using NF etching to reduce LER values. Also, side-walls should have higher initial roughness values, resulting in an even higher intensity of ONFs and thus etching rate, meaning that we should be able to repeat the roughness reduction results at the photoresist side-edges.

Should NF etching establish itself as a reliable tool for the high-end lithography industry, production costs could be reduced (since companies could focus more on the other two parameters, resolution and sensitivity; RLS tradeoff relation) and possibly even smaller node sizes could be achievable (e.g. diminishing impact of stochastic effects, thus bypassing current limitations).

We further note that the cross-section view (over NF etching time) differs between the previously obtained results for the diamond substrate edge and the photoresists. While the edges of the diamond substrate appeared to sharpen over NF etching duration, we were not able to reproduce the same phenomena for the photoresists. One possible reason for this could be the fact that the single-crystal structure of the diamond substrate is favorable for having a seemingly clean-cut side profile. While the diamond edges, after NF etching, seem very sharp (and thus like a suitable breeding ground for ONFs), the structure might appear slightly rounded when zooming up to the nanometer range. On the other hand, the cross-sectional profile of the organic photoresists doesn't seem to get as sharp-cut as that of the diamond substrate. Reasons for this could be that the organic photoresists are a multi-component material, which results in stochastic fluctuations along the sides of the sample. In other words, since it consists of wildly arranged molecules it might be difficult to realize a perfectly clean-cut profile (Fig. 4.16a).

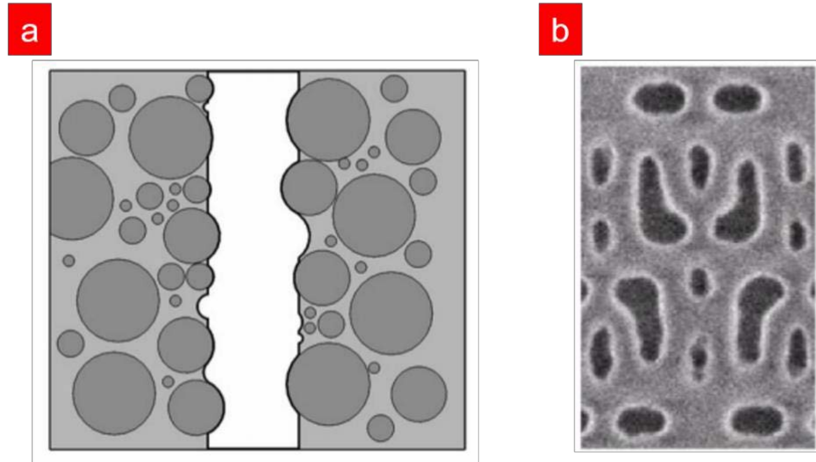

Figure 4.16. Challenges in using NF etching for high-end lithography [63, 57].

(a) Illustration showing stochastic distribution of polymer composites and the resulting edge roughness (b) Typical wafer photoresist structure showing components of various shapes (Reprinted with permission from [63] and [57]. Copyright 2016 Springer Science+Business Media Dordrecht & Copyright 2017 Society of Photo-Optical Instrumentation Engineeers (SPIE).

A possible limitation for using NF etching as a technique to improve photoresist lithography is its yet not fully understood structural etching behavior. Since we assume that the inherent material differences between diamonds and organic photoresists are the reason for their different post-NF etching shapes (clean-cut, sharp edge diamond vs. overall rounded photoresist), a material dependency seems apparent. High-end lithography offers a wide spectrum of photoresist candidates (organic CAR, metal oxide photoresists, nanoparticle photoresists, etc.), so before using NF etching on a larger scale, the NF etching shape-building behavior should be checked for each respective resist first. In the case of organic CARs another problem is the fact that only a simple continuous trench-line pattern of photoresist has been studied. Here NF etching was able to reduce roughness values and also reduce the overall resist width. However, real-life industrial lithography uses photomasks of various shapes, resulting in a wide range of photoresists structures as well

(Fig. 4.16b). While NF etching seemed effective in for the simple line-trench pattern model, wafers are usually a combination of various shapes and thus finding common etching parameters for improving the overall device performance could prove difficult. We can see in Fig. 4.16b that when applying NF etching for long durations we risk losing the smaller structures in the middle. Also, NF etching might interfere with the pre-intended shape of the structures, such as the L-structures in Fig. 4.16b. Since NF etching should be the most intense at places parallel to the E-field polarization of the laser source, having structures stretched along multiple axes risks having more etching, and thus structural changes, on one axis than the others.

Chapter 5.

Improving NV nanodiamond electron spin properties

5.1 Background

The NV center is one of over 100 known defects inside the diamond lattice. Those defects are impurities within the crystal-lattice of the diamond. Especially the NV center has proven to be promising for a future single-photon source which can work under ambient temperatures. For an all-encompassing recent review about NV centers please refer to [64]. Possible applications could be found in quantum computing [65], quantum cryptography [66] as well as a nano-dimensional sensing. Since in this Chapter we focus on nanodiamond based NV centers, sensing applications are especially interesting. The reason why we focus on nanodiamonds rather than bulk diamonds is that NV centers in nanodiamonds are surrounded by more surface area. The NV spin performance (i.e. T_2 time) is dependent on the diamond surface state (i.e. paramagnetic noise). So by studying nanodiamond NV centers, we hope to find a relationship between NF etching and NV performance.

Unfortunately, nanodiamond NV centers suffer from shorter coherence times compared to bulk diamonds [67], making them rather impractical for quantum sensing applications, which require extremely long coherence times [68].

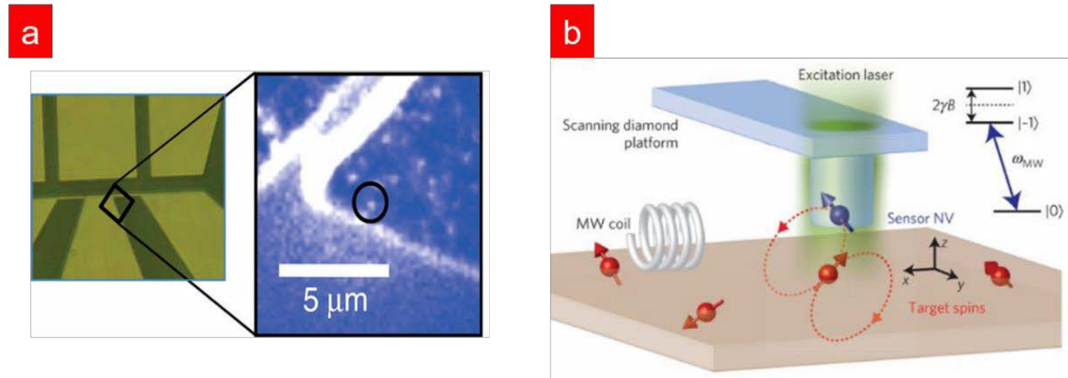

Figure 5.1. NV center applications [69,13].

(a) *(left) Image showing coplanar waveguide on diamond containing NV centers.(right) spatial fluorescence image (obtained through confocal microscopy setup) showing NV center distribution along diamond mesa. Bright spots (=fluorescent) hereby representing NV centers. (Reprinted figures with permission from [69]. Copyright (2019) by the American Association for the Advancement of Science.) (b) Scheme of scanning NV magnetometer. NV spin (blue) couples itself with nearby spins (red), effectively changing its larmor precession. (Reprinted figures with permission from [13]. Copyright (2019) Springer Nature Publishing AG.)*

5.2 Structure of the NV Center

Naturally formed as well as synthesized diamonds contain a wide range of structural as well as material impurities. It is possible to classify the diamond in dependence on the degree of contamination by alien atoms [70]. An important class is the diamond type 1b. Inside the 1b diamond lattice, the nitrogen atoms are evenly distributed within the diamond lattice, and they don't occur in agglomerations. This is one of the reasons why it is possible to detect so many different nitrogen-related defects inside diamond. One of the most famous defects inside the diamond lattice is the NV center, and it is also one of the most promising defects, especially for single photon source applications. Basically speaking, the NV center is a complex compound made up of a single nitrogen atom in connection with a neighboring vacancy.

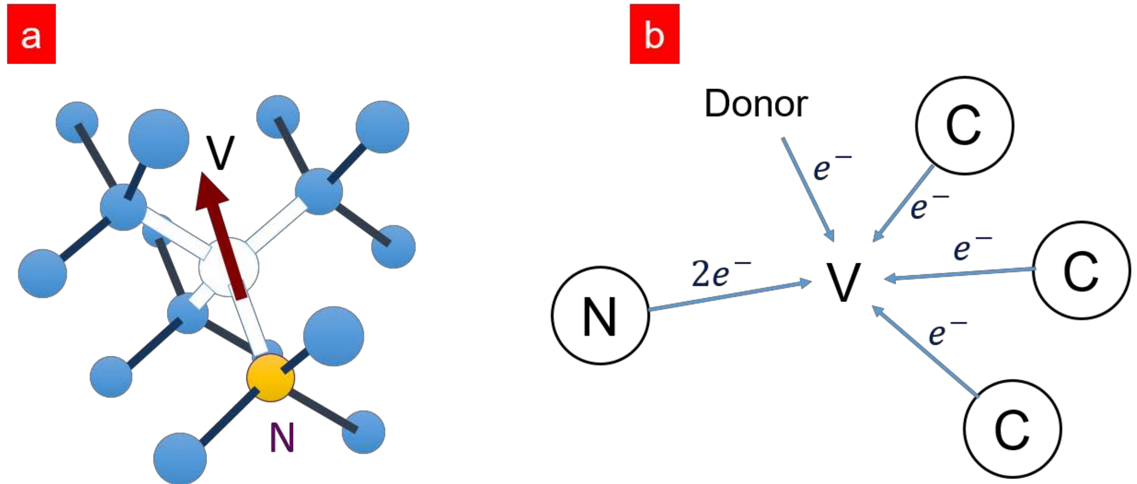

Figure 5.2. NV center configuration [71].

(a) NV center orientation within the diamond lattice. Its orientation (red) is determined by the axis connecting the vacancy and the nitrogen atom. (Reprinted with permission from [71]. Copyright (2009) American Physical Society.) (b) Electron configuration of a NV center inside the diamond lattice. The negatively charged NV center consists of 6 electrons.

5.3 Readout, AC and DC Sensing with NV centers

The NV center is currently one of the most promising candidate to revolutionize our sensing capabilities. Due to the NV's atomic size it can be brought into closest proximity to magnetic test objects, and furthermore the single NV center possesses a fluorescence which is strong enough to be seen through the confocal microscopy (or wide field microscopy) setup. Under visible illumination (usually 532 nm) (Fig. 5.3a) the NV center exhibits a fluorescence signal, which depends on its electron ground state alignment, normally ranging between 650-750 nm. Fig. 5.3b illustrates in principle how NV centers are being detected with a confocal microscopy setup. The confocal microscopy setup picks up the fluorescence signals from NV centers within its light cone, meaning a typical width (y-direction) of around 1-2 µm at its focal spot. The confocal microscopy setup uses pinholes as well, in order to only collect NV signals from the focal plane.

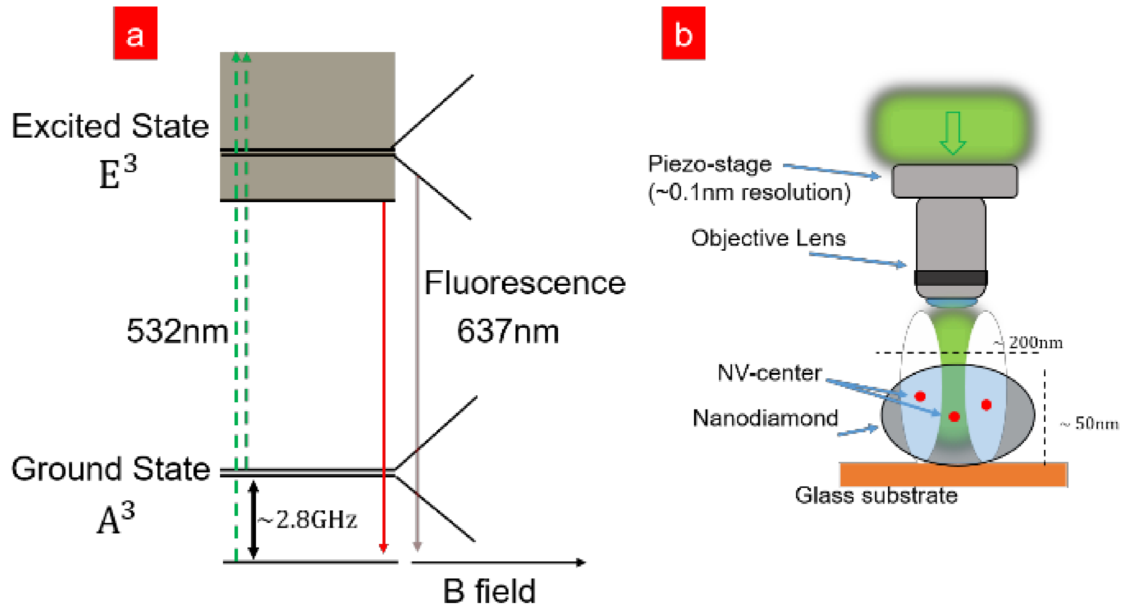

Figure 5.3. Energy levels of NV center and illustration of confocal setup.

(a) The electron energy levels of the NV center. The zero-phonon-line emission of the NV center amounts for 637nm. Triplet ground state showing the zero field splitting value (2.8 GHz). Magnetic fields cause Zeeman splitting of spin degeneracies. (b) Illustration of confocal microscopy sensing of NV nanodiamond. NV signals detected within the confocal volume (green cone).

The ability to optically detect NV centers (and read-out its energy levels), alongside other unique characteristics such as long coherence times at room temperature and well-defined optical transitions, are what makes the NV center so attractive for various fields, such as medical science, quantum science, quantum computing, bio-sensing and many more. Fundamentally speaking, the NV can be described as a high-sensitivity nano-magneto-sensor, and the reason for this is its unique electronic band structure. As mentioned previously, the NV center possesses a triplet ground state, with three possible m states [-1, 0, +1]. Under normal conditions (no external magnetic field) the degeneracies of the ground state [-1] and [+1] are not divided, but as soon as the magnetic field strain increases (especially alongside the NV's axis), the spin states [-1] and [+1] are split further

apart in dependency of the magnetic field (Fig. 5.4). This effect is also called the Zeeman effect. Lastly, it is possible to locate the energy locations of the spin states [-1] and [+1] by applying microwaves equivalent to their respective energy level differences (ODMR or ESR measurements), effectively meaning we can use NV centers as magnetic field sensors.

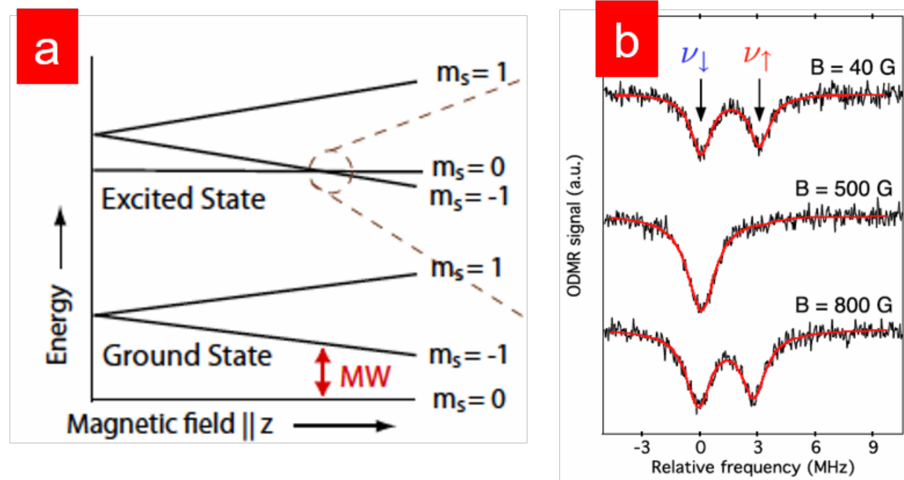

Figure 5.4. Zeeman splitting of spin degeneracies [71].

(a) Illustration of Zeeman splitting of the ground state and excited state degeneracies (m=±1). (b) The NV ESR recorded at different magnitudes of magnetic fields. Fitting lines (red) obtained by Lorentzian functions. (Reprinted with permission from [71]. Copyright (2009) American Physical Society.)

When neglecting weak hyperfine interactions of the NV center with nearby ^{14}N and ^{13}C nuclei, the Hamiltonian of NV centers is defined by [72]:

$$H = D\left(S_z^2 - \frac{1}{3}S^2\right) + \gamma_e B(\cos\theta S_z + \sin\theta S_x) \quad (5.1)$$

Where D (= 2.87 GHz) represents the zero field splitting (B = 0), $\gamma_e = 2.8$ MHz/G represents the gyromagnetic ratio (Zeeman) and θ represents the angle between the magnetic field and the NV axis (the axis connecting the Nitrogen atom to the vacancy).

Within the diamond crystal structure, the NV center can be oriented along four possible crystallographic axes: [111], $[\bar{1}\bar{1}1]$, $[\bar{1}1\bar{1}]$ or $[1\bar{1}\bar{1}]$ (Fig. 5.5a).

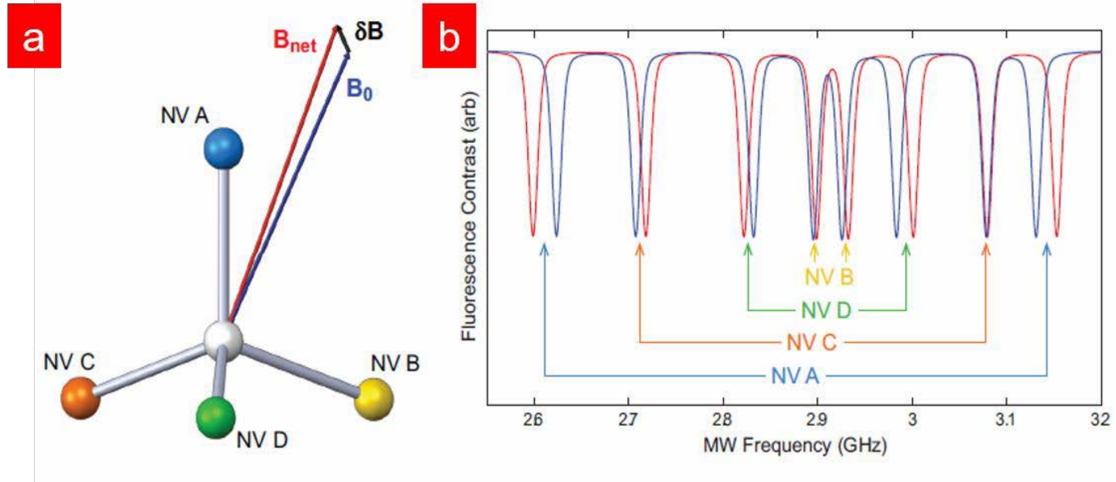

Figure 5.5. ESR based DC Magnetometry with NV ensemble [73].

(a) Illustration showing detection of vector magnetic field. (b) DC magnetometry based on NV ensemble. NV centers with parallel symmetry axis to the magnetic field vector experience highest splitting (NV A) ((a)&(b)Reprinted with permission from [73]. Copyright 2013 Linh My Pham)

From Eq. 5.1 we understand that the closer a magnetic vector is aligned to the NV axis, the stronger the overall splitting. As such, when the confocal volume contains multiple NV centers of various orientations, their general ESR spectra (Fig. 5.5b) can give away the vector information of an unknown magnetic field [73].

In principle, the sensitivity for DC magnetic sensing using ESR is defined by [74]:

$$\eta_{DC} \sim \frac{h}{g\mu_B}\frac{\Delta\nu\sqrt{t_m}}{C\sqrt{I}} \quad (5.2)$$

Where C is a numerical parameter related to the lineshape of the NV resonance (Gaussian lineshape ≈ 0.7 or Lorentzian lineshape ≈ 0.77 [74]), a the ESR fluorescence contrast, $\Delta\nu$ representing the resonance linewidth (also referred to as FWHM in this thesis)

and

representing the measurement time. $\Delta\nu$ can be further decreased by reducing the laser power (avoiding power broadening) and increasing the free induction dephasing time T_2^*, however eventually reaching a limit value, defined by T_2^* as well. To get the DC sensing sensitivity dependence on T_2^* we can rewrite Eq. 5.2 as [74]:

$$\eta_{DC} \sim \frac{2\hbar}{g\mu_B}\frac{1}{C\sqrt{T_2^*}} \quad (5.3)$$

From Eq. 5.3 the importance of long coherence times for sensing applications becomes apparent.

For T_2 (spin echo) based AC magnetometry, instead of just relying on the free induction dephasing of the NV spin (NV spin dephasing after being brought to its superposition state by a $\frac{\pi}{2}$-pulse, see Bloch sphere), additional techniques are being implemented in order to prolong the T_2 time and thus improve phase accumulation. The most common technique, Hahn-Echo, uses an additional π-pulse after some time of the initial $\frac{\pi}{2}$-pulse, flipping the coefficient of the net phase accumulation from positive to negative. Constant coefficient DC magnetic fields would hereby simply be cancelled out. As such, the idea is to time the π-pulse with the frequency of the target AC magnetic field, and thus ideally have a synchronized flipping of coefficients. The result will be a net phase accumulation through two separate phase accumulation times (before and after the π-pulse).

In principle, the sensitivity for AC sensing applications is defined by [75]:

$$\eta_{AC} \approx \frac{\pi\hbar}{2g\mu_B}\frac{1}{C\sqrt{T_2}} \quad (5.4)$$

Where T_2 (see Appendix B4) stands for the Hahn-Echo coherence time.

ESR based AC sensing can also be realized, where we find target signals as follows (Fig. 5.6): First of all the ESR (or ODMR) of the NV spin will be obtained by setting the MW energy to the same value as the NV ground state energy (Fig. 5.6a). After applying an AC magnetic field (B_{ac}) the fluorescence signal will start oscillating since the local magnetic amplitude affecting the NV center changes (Zeeman effect). The fluorescence over time signal will be obtained through a photo detector (Fig. 5.6b). Lastly, the target AC magnetic field signal will be read-out after bringing the raw time date into frequency domain.

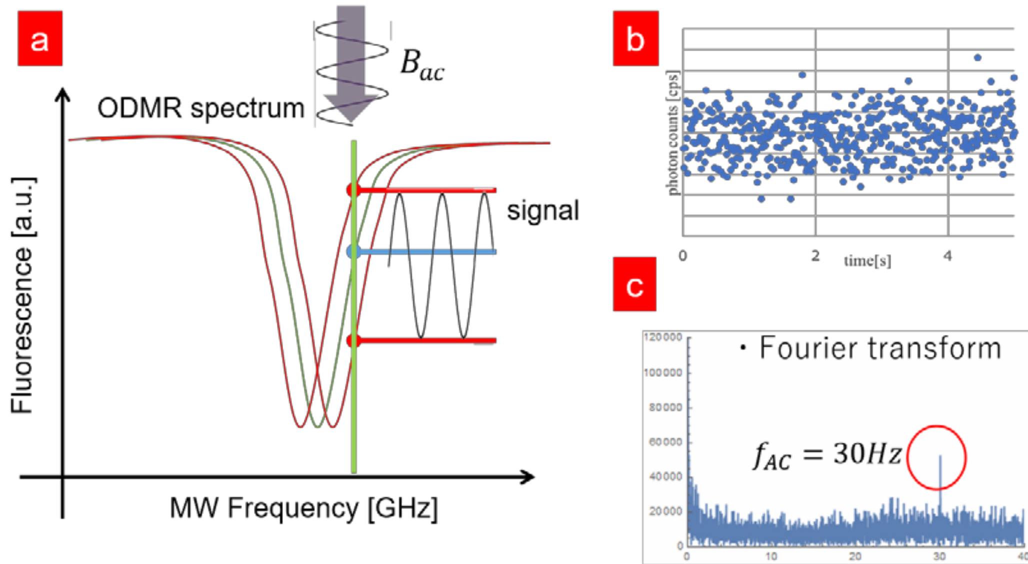

Figure 5.6. ESR based AC Magnetometry.

(a) AC B-Field causes vibration of NV ESR signal. (b) Time-dependent fluorescence signal detected through photodetector. (c) Transformation into frequency domain, detection of target signal (red circle).

Looking at Eq. 5.3 and 5.4 we can expect improved magnetic sensitivies when prolonging the NV coherence times. And since the coherence times are dependent on the surface state of the diamond (i.e. paramagnetic noise), we expect that NF etching should be able to prolong coherence times by removing impurities from the NV nanodiamond surface. Spin echo based NV magnetometry should especially benefit from prolonged T_2

values. ESR based NV magnetometry should especially benefit from reduced FWHM values.

5.4 Surface noise influence on NV spin properties

Whenever a system is in the quantum coherence state, it is basically in a superposition and can therefore be used for quantum operations. The most common NV center coherence time measurement is done by the Hahn Echo method. Generally speaking, T_2 is the time required until the total signal reaches $\frac{1}{e}$ of its initial value (see appendix B).

NV centers close to the surface (<10 nm) have their spin coherence time strongly influenced by surface impurities and paramagnetic defects. As a result, NV charge stability suffers [76], the ESR lines are being broadened [77] and general shorter coherence time for NVs close to the surface as compared to deeper ones [78].

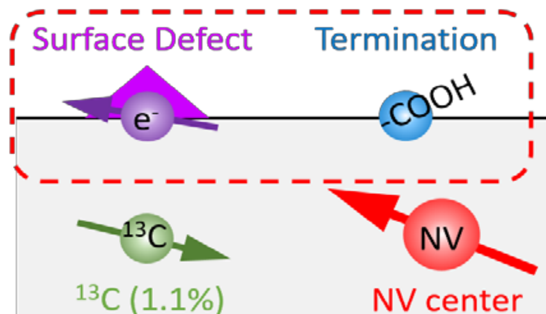

Figure 5.7. Common T_2 limitations of NV centers.

Illustration of the most common factors limiting the NV T2 coherence time. Surface defects and termination groups targetable by surface conditioning techniques.

Fig. 5.7 depicts some of the classic limitations to the NV T_2 time. Surface defects [79] and termination groups [80] hereby play a significant role. An even greater limitation

to the NV T_2 time originates from neighboring ^{13}C atoms within the diamond lattice. However we will only concentrated on the surface impact in this chapter.

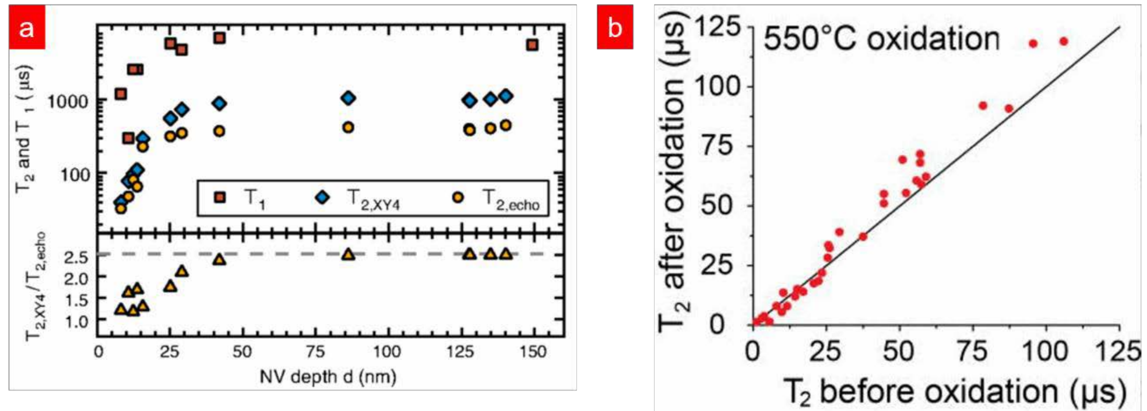

Figure 5.8. Surface depth dependence of T_2 [78] and [81].

(a) Coherence time values over NV depth, showing strong surface influence on the T_2 performance. (Reprinted with permission from [78]. Copyright 2014 American Physical Society). (b) Improvement of T_2 coherence time via thermal oxidation at 550 ° C. (Reptrinted with permission from [81]. Copyright 2014 AIP Publishing LLC.)

The studies performed in Fig. 5.8 underline the importance of the diamond surface state for T_2. Fig. 5.8a depicts the general dependency of the coherence time to the NV depth [78]. We can see that deeper NV centers exhibit longer coherence times, because they are not influenced by surface effects. In Fig. 5.8b we can see how thermal oxidation impacts overall T_2 performance [81]. In that study it was shown that etching the NV bulk-diamond surface for 1 hour at 550 °C improves the overall T_2 performance.

Unfortunately, not many NV surface conditioning studies have been performed for NV nanodiamonds. Furthermore, sensing applications would benefit from having its NV sensor as close as possible to its target molecule (which is partly a reason why

nanodiamonds are often preferred in bio-sensing applications in addition to their higher mobility). Hence the problem cannot simply be avoid by relying on deeper NV centers.

5.5 NF etching on NV nanodiamonds

From the results observed in chapter 4, we believe that nanodiamonds can be structurally modified in a similar way. It is expected that NF etching will cause a size reduction of the nanodiamonds, and with it a removal of possible spin noise on the diamond surface (Fig. 5.9).

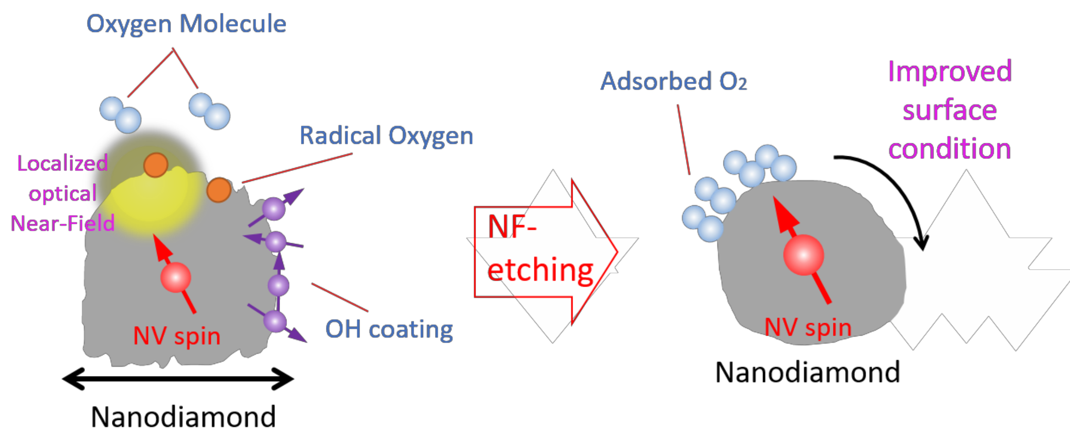

Figure 5.9. Scheme of NV nanodiamond surface conditioning by NF etching.

Scheme of how NF etching could improve the electron spin properties in NV nanodiamonds. NF etching is able to condition the surface of the nanodiamonds, reducing the amount of structural defects and parasitic objects.

The reason why we think that NV nanodiamond electron spin properties can be improved by NF etching is that T_2 is limited by fast fluctuations (those which cannot be refocused by refocusing techniques, e.g. Hahn-Echo) which can originate from flip-flops of spins along the diamond surface. This lets us assume that the T_2 time of the NV nanodiamond is directly

dependent on the amount of noise on the surface of the diamond. I would like to note that there has been recent research indicating that the main contribution to the decoherence of the NV center in diamond originates from neighbouring nitrogen impurities within the diamond itself, close to the NV center itself [67]. Regardless, the method applied in this paper could still be interested for other color defects and qubit candidates, which are more dependent on the surface noise conditions than the NV center. In order to reduce the impact of the surface on the electron spin properties of the NV center, I would like to apply the NF etching method. Instead of the obvious dynamical decoupling method, which has also been proven to reduce the impact of surface noise [82], I would like to use the NF etching method, which has proven to be effective in surface conditioning. The reason for choosing the 325 nm laser as the far-field source is that previous research indicates that NF etching based on a 325 nm light source has been successfully used for even etching diamonds [83], all of course under ambient conditions. This chapter will demonstrate that under sufficiently long NF etching times (325 nm), a visible size reduction of the nanodiamonds, a decrease of the FWHM value of the ODMR spectrum and increase of the NV T_2 coherence time was achieved. All these observations confirm the effectiveness of NF etching as a surface conditioning technique, more specifically in the case of the NV nanodiamond, for removing parasitic magnetic noise on the diamond surface.

As mentioned before, NF etching was used as an attempt to improve the electron spin properties of the NV nanodiamond. During far-field light irradiation, ONFs are locally induced at sub-wavelength objects (i.e. nano-scale surface protrusions), which interact with the surrounding O_2 molecules, and are even assumed to cause the dissociation of said molecules, in addition to the far-field photon energy. The dissociation of the O_2 molecules

results in two highly reactive radical oxygen atoms, which will interact with its immediate surrounding, and in our case causes the etching of the outmost layers of the nanodiamond. Generally speaking, the ONFs have non-uniform properties, meaning that the conventional dipole-approximation cannot be applied for them, which can result in the excitation of dipole-forbidden states in molecules and thus trigger reactions such as NF based second harmonic generations [84]. When considering the fundamental concept of NF etching, it is crucial to remember that the photon energy of the far-field light source (325 nm, 3.81 eV) has to be lower than the photo-dissociation energy of the etching gas molecule itself, in this case O_2 (242 nm, 5.12 eV) [85-88]. What this means is that the etching effect is dependent on locally induced ONFs, instead of mere conventional adiabatic etching by direct photo-dissociation of the O_2 molecule through a strong far-field light source. NF etching has been shown to be effective for both, conditioning diamond substrates as well as nanodiamonds [89].

5.6 Experimental

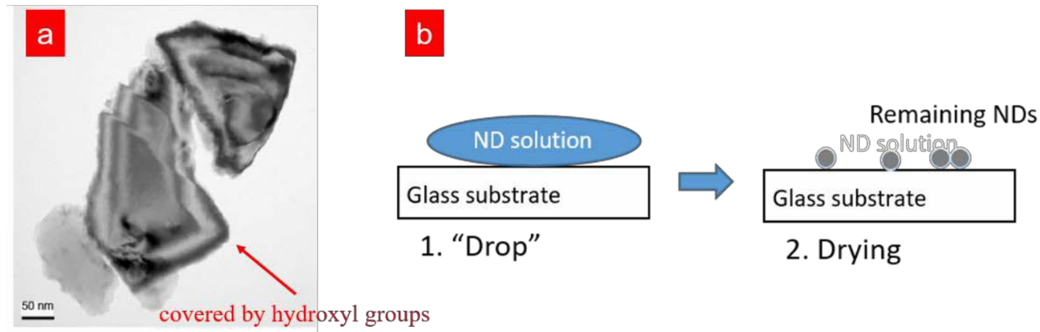

Figure 5.10. Fabrication of nanodiamond samples [90].

(a) TEM image of OH-coated monocrystalline nanodiamonds (Reprinted with permission from [77]. Copyright 2013 IOP Publishing Ltd). (b) Illustration of sample fabrication. After ultrasonic rinsing, the nanodiamond solution will be dropped on the glass substrate.

In this experiment (Fig. 5.10) the NV nanodiamonds were irradiated by a He-Cd laser (325 nm, 8 mW) under ambient conditions, i.e. atmospheric conditions with O_2 molecules assumed as the etching agent. The size of the nanodiamonds were depending on the experiment type typically between 50 and 200 nm. As described in the Method section, the nanodiamonds were dispersed on top of a Si substrate. The rFND (50-nm, containing single NV) were used for the AFM and T2 measurements, while the cFND (typically 200-nm, containing approximately 500 NV, obtained through milling (8000M, SPEX) of microdiamond powder) were used for the FWHM measurements. Both nanodiamond types were initially covered by hydroxyl groups. Afterwards, the nanodiamonds were exposed to UV laser irradiation. It appears that over UV laser irradiation duration the size of the nanodiamonds has been reduced, including a possible improvement of the electron spin properties. Anyways, we first would like to check the degree of the structural size change of the nanodiamond over NF etching time

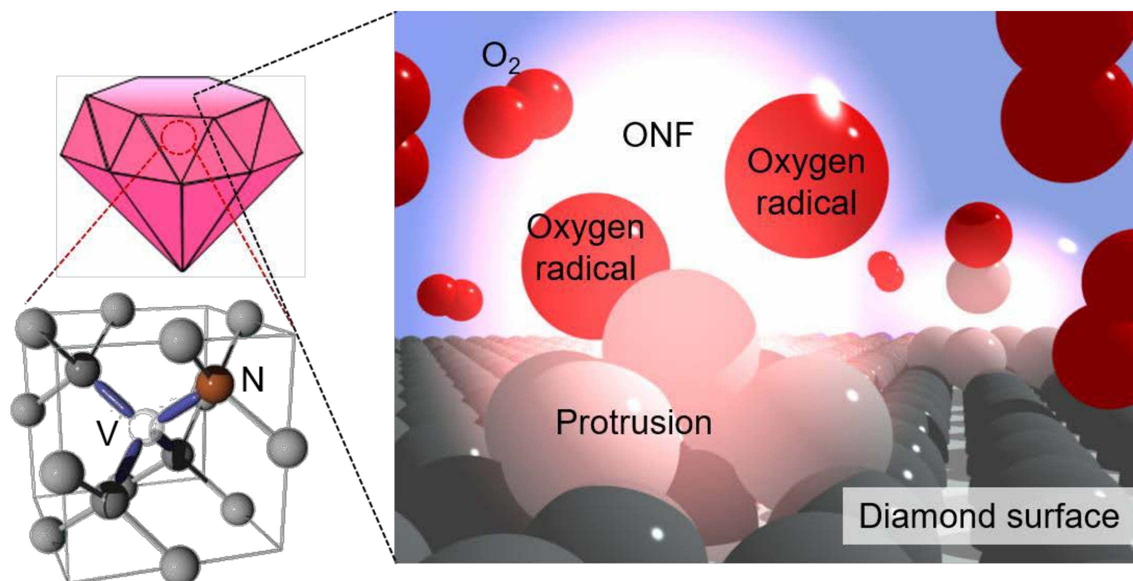

Figure 5.11. Scheme of NF etching on diamonds surfaces [91].

A schematic view of NF etching on the NV nanodiamonds. ONFs are generated by the He-Cd laser (3.81 eV) irradiation at the nanoscale protrusions on the nanodiamond surface. Since the photon energy is below the O_2 dissociation energy (5.12 eV), O_2 is only dissociated at the protrusions, thus allowing selective etching (Reprinted with permission from F. Brandenburg et al. Sci. Rep. 8, 15847 (2018). Copyright 2019 Springer Nature Publishing AG)

5.7 Results and Discussion

In Fig. 5.12 we can see the degree of size reduction of the nanodiamonds over the NF etching duration. It is important to notice that we are especially interested in the parallel-axis (p) (i.e. parallel to the He-Cd laser polarization (E), rather than the perpendicular-axis (s). Accordingly, the white dashed-lines in Figs. 5.12a and 5.12b represent the parallel-axis and the perpendicular-axis of the laser polarization. Fig. 5.12a shows a typical nanodiamond before we applied NF etching. Its diameter is roughly 200 nm [92]. In Fig. 5.12b we can see the exact same nanodiamond observed in Fig. 5.12a, but this time after 90 min of NF etching exposure. What can be immediately seen here is that the size of the nanodiamond between these two time-stamps has been drastically changed.

After 90 min NF etching the diameter of the nanodiamond appears to have fallen to around 100 nm, roughly halved when compared to before etching. In the following part, Fig. 5.12c, the cross-sectional area change along the parallel-axis and the perpendicular-axis has been observed over the NF etching time-intervals. The data was obtained and averaged for 8 individual nanodiamonds. The changes along the parallel-axis and the perpendicular-axis were observed since previous research indicates that NF etching should mainly occur along the laser-parallel polarization axis. What we can see is that within the initial NF etching interval (0-30 min) the area has been approximately halved (52% for p-axis and 62% for s-axis). Over longer NF etching the size doesn't appear to change as drastically as in the initial time interval. After 60 min of NF etching the size along the p-axis was reduced to 46% and along the s-axis to 63%. Lastly, after 90 min of NF etching the size along the p-axis was finally reduced to 42% while the area along the s-axis was reduced to 56%. What we can also see is that in accordance to my previous study (Chapter 4), again, the NF etching effect appears to saturate over etching time. I would like to note that it would of course be nice to have longer NF etching times in order to deepen our understanding of the saturation effect of NF etching over long very periods, however this proves to be extremely difficult to realize in praxis (due to great difficulty in keeping the AFM locked onto the same nanodiamond).

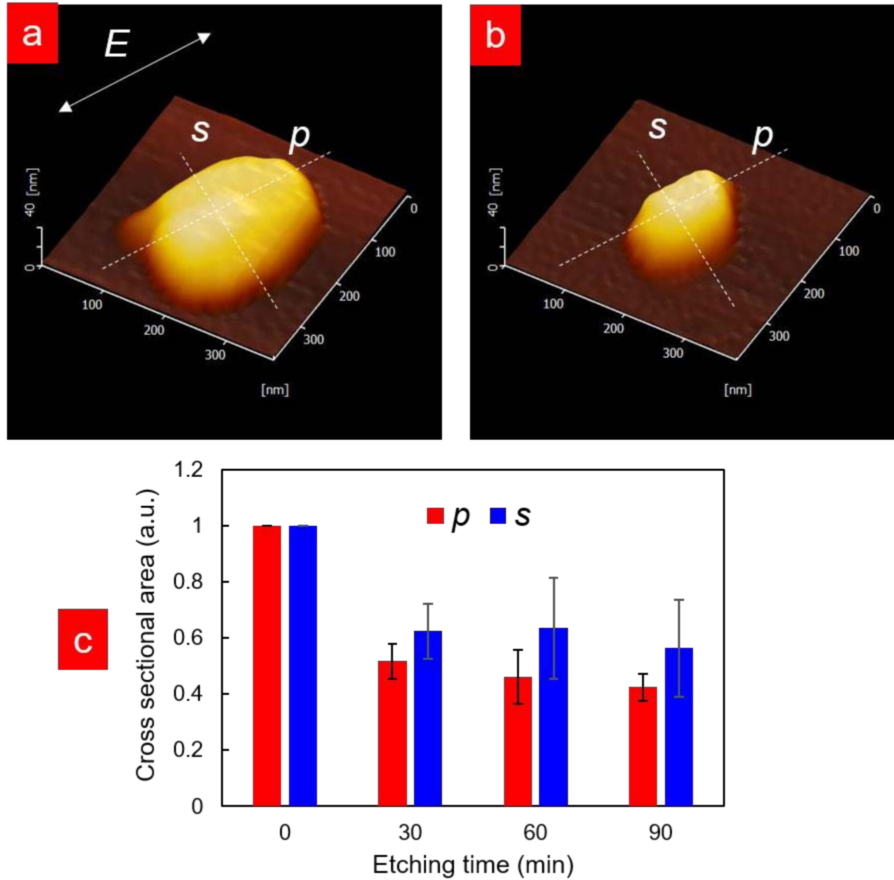

Figure 5.12. Size reduction of NV nanodiamonds [91]

AFM images of the nanodiamonds, comparing their size before (a) and after 90 min (b) of He-Cd laser illumination. The comparison in size has been further examined through AFM in (c) by comparing the cross-sectional area of the nanodiamonds along the presumed parallel laser polarization axis (p-axis) and the presumed perpendicular laser polarization axis (s-axis), showing a general decrease in the cross-sectional area over illumination time. (Reprinted with permission from F. Brandenburg et al. Sci. Rep. 8, 15847 (2018). Copyright 2019 Springer Nature Publishing AG)

In Fig. 5.13 we more specifically observe the change of the ODMR spectrum and its connected FWHM value for the NV nanodiamonds over NF etching time. Fig. 5.13a shows the time-averaged ODMR spectra for 500 s. When looking at Fig. 5.13 we have to remember that all the data has been obtained from the same NV nanodiamond, containing 500 NV, for each NF etching interval. What we can immediately see in Fig. 5.13a is that

the FWHM of the ODMR spectrum appears to be decreasing with ongoing NF etching exposure. To read out the exact FWHM we need to create a fitting of the raw data seen in Fig. 5.13a. This was been done by a single Lorentzian fitting of the raw ODMR spectrum in Fig. 5.13a. As a result, we were able to gain a more detailed view of the effective change of the FWHM value, and this is shown in Fig. 5.13b. In Fig. 5.13b the dots are representing the average FWHM value for each NF etching interval. The error bar hereby represents the variance of the raw data points from their Lorentzian fitting in Fig. 5.13a. So, when looking at Fig. 5.13b, we can see that the initial value of the FWHM was around 23 MHz and decreased gradually over the NF etching time until it reached its lowest value at around 19.6 MHz after a total NF etching time of around 90 min. This means an effective ~15% reduction, i.e. improvement, of the FWHM value compared to its initial value. What is interesting however, is that after longer NF etching times than 90 min the FWHM value seems to increase again, in the end reaching a value of approximately 20.5 MHz for etching times up to 150 min. Another thing we have to take note of is that the NF etching as a side effect also reduced the total contrast of the NV nanodiamonds (by reducing the net number of NV centers). This is an unfortunate side-effect of the size reduction of the NV nanodiamonds. Regardless, in theory we could prepare larger NV nanodiamonds with a larger number of NV centers as well, in order to mitigate the contrast reduction side-effect caused by the sample size reduction due to NF etching. Another idea would be to take into account the typical NF etching ratio, and ensuring that future samples have the majority of their NV center populations deeper inside the nanodiamonds. In this case, NF etching would only condition the surface of the nanodiamonds, i.e. remove parasitic objects, while the total amount of NV centers would stay nearly same. That is why we believe that our

technique can generally improve the sensitivity of NV centers (by reducing its FWHM value) while simultaneously keeping the ODMR contrast constant.

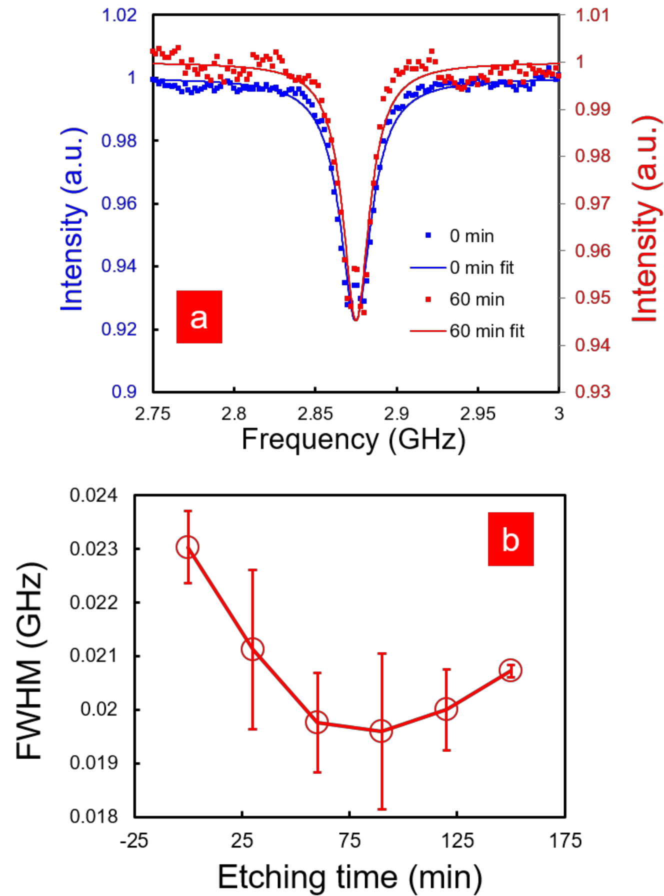

Figure 5.13. ODMR spectrum and FWHM value of NV center [91]

(a) ODMR spectra before (blue solid line (left-hand vertical axis); 0 min.) and after (red solid line (right-hand vertical axis); 60 min) NF etching. (b) FWHM value of the ODMR spectrum as a function of the NF etching time. (Reprinted with permission from F. Brandenburg et al. Sci. Rep. 8, 15847 (2018). Copyright 2019 Springer Nature Publishing AG)

In Fig. 5.14a-c we consider the change of the Hahn-Echo T_2 coherence times of the NV nanodiamond for before and after NF etching. In general, the accumulation time for the Hahn-Echo T_2 algorithm was 1000 s. Again, it should be noted that all Hahn-Echo

signals were obtained from the same nanodiamond (single NV center type). In Fig. 5.14b we can quickly see that the coherence time recess seems to be slower than in Figs. 5.14a and 5.14c, thus we can say that Fig. 5.14b appears to have a longer T_2 coherence time than the other two figures. In order to be able to extract the exact T_2 coherence time for each graph, we had to use an exponential fitting for each graph. The points (splatters in Figs. 5.14a-c) seen in each graph is the raw data obtained by the Hahn-Echo measurement. They were fitted to an exponential function $f(t) = \exp[-t/T_2]$. In order to simplify the change of T_2 coherence times, the T_2 coherence times were plotted as a function of the NF etching time in Fig. 5.14d. All of the nanodiamonds used for the T_2 coherence time measurement were only containing a single NV center on average and the error bar in this case simply represents the variance of the raw data from their exponential fit from Figs. 5.14a-c. What stands out immediately is the fact that the T_2 coherence time appears to be increasing with the NF etching duration. Initially, the T_2 coherence time was approximately 1600 ns for 0 min. After NF etching was applied the T_2 coherence time increased up until its peak of around 2000 ns after 60 min of NF etching. That is an increase of the T_2 coherence time of about 25%. Interestingly, the T_2 coherence time started to drop again after that, for longer NF etching times. It finally hit its bottom value of around 1400 ns (~87.5% of its starting value at 0 min) for NF etching times longer than 120 min.

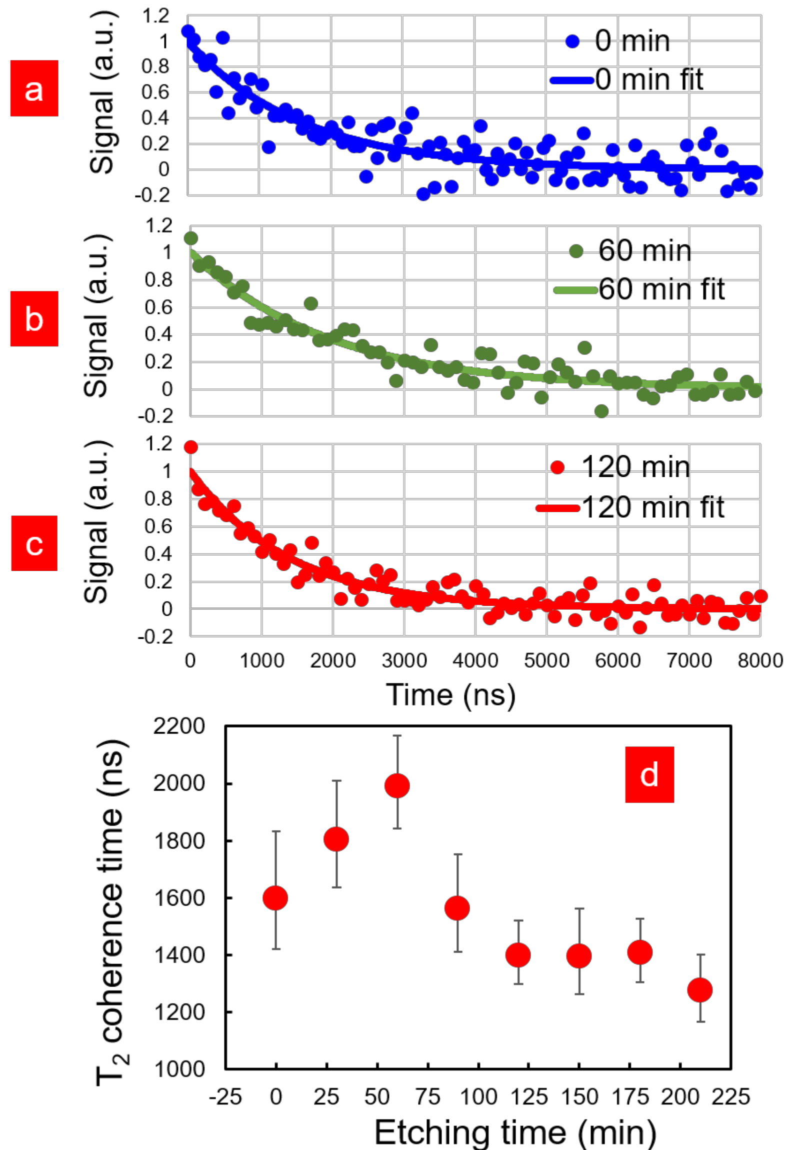

Figure 5.14. T_2 (Hahn Echo) coherence time of NV center [91]

Normalized Hahn-echo signals (dots) before (a), after 60 min (b), and after 120 min (c) of NF etching, with exponential fitting curves (lines). (d) The measured Hahn-echo T_2 of the single-NV nanodiamond as a function of the NF etching time. (Reprinted with permission from F. Brandenburg et al. Sci. Rep. 8, 15847 (2018). Copyright 2019 Springer Nature Publishing AG)

Another interesting aspect we can consider when looking at the effect of NF etching on the NV nanodiamonds are its Cathodo-Luminescence (CL) values. For this experiment

the 200-300 nm nanodiamond (containing 500 NV) was used. The 325 nm laser power was constant at approximately 30 mW. In Fig. 5.15a we can see that with increasing NF etching time the intensity ratio of the cathode-luminescence increases as well. The intensity ratio reaches its peak value after around 60 min NF etching, which equals an increase of slightly more than 100% of its initial value. After the 60 min mark, the intensity ratio starts to drop of again, in similar fashion to the results for the T_2 coherence time and the FWHM value. The reason for this drastic change of its CL signal can be derived from the strong impact of non-radiative defects on the CL (Fig. 5.15b).

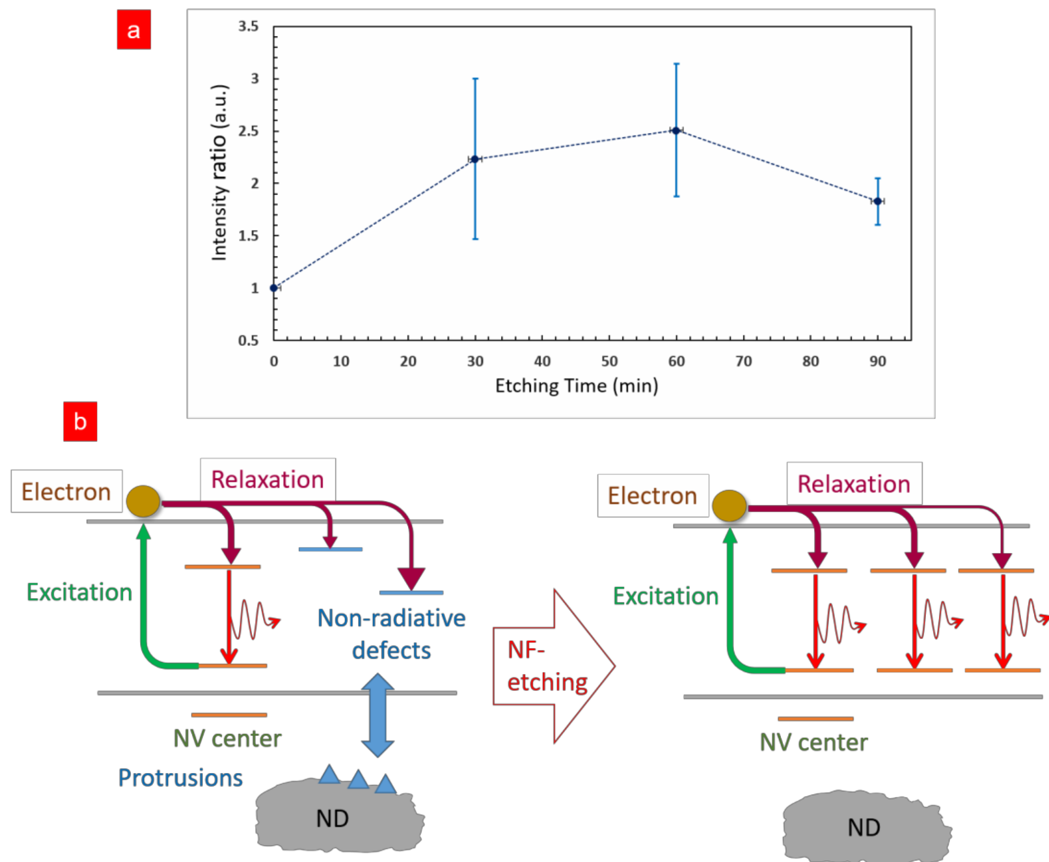

Figure 5.15. CL value of NV nanodiamonds

(a) CL signal of the NV nanodiamond over NF etching time (b) Scheme of how NF etching improves CL signals by decreasing the amount of non-radiative defects along the nanodiamond surface.

In the following Fig. 5.16 we can see the impact of NF etching on the overall photoluminescence signal of the NV nanodiamonds. The photoluminescence observed in Fig. 5.16a belonged to the 50 nm nanodiamond type (containing only a single NV center) and we can easily see that NF etching did not remove the NV center. The intensity ratio of the photoluminescence stays approximately same throughout the whole NF etching duration. In Fig. 5.16b we can see the general photoluminescence spectrum of the before mentioned nanodiamond. From its photoluminescence spectrum we can clearly see that the signal does indeed originate from a NV center.

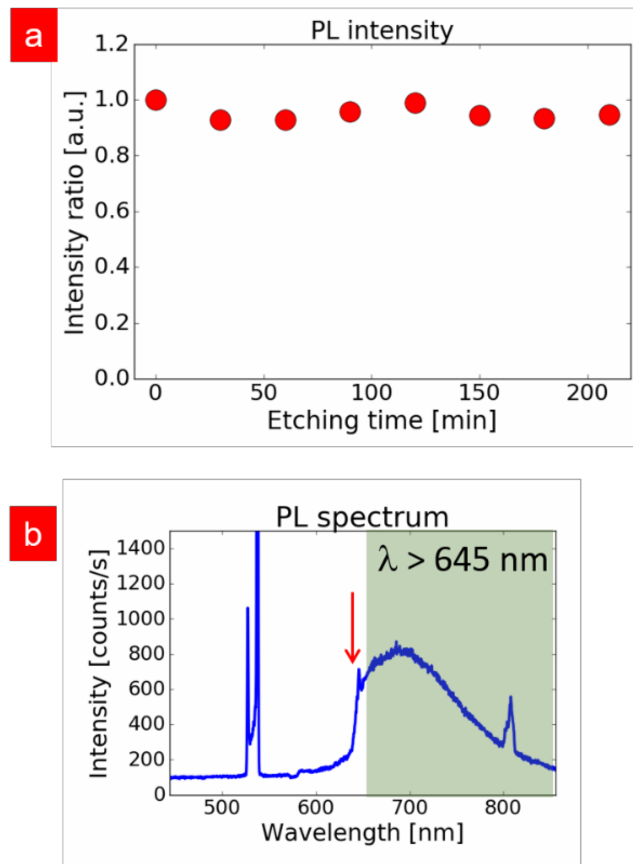

Figure 5.16. Photoluminescence intensity spectrum of NV nanodiamonds

(a) Photo-luminescence signal of the NV nanodiamond over NF etching time (b) Photo-luminescence spectrum showing the typical NV center vibrational band reaching up until the infrared wavelengths.

What has been demonstrated by the results is the fact that NF etching is indeed capable of increasing the T_2 coherence time of NV nanodiamonds as well as reduce the FWHM value of NV nanodiamonds, thus increasing the sensitivity. Both improvements happen on a relatively early time-frame, until they peak at around 60 min for the T_2 coherence experiment and around 90 min for the FWHM value experiment. We can conclude from Fig. 5.13b and Fig. 5.14d that there is a specific time interval for specific NV nanodiamond samples in which their respective electron spin property (T_2 coherence time or the FWHM value) can be greatly improved by NF etching.

In regards to the reason for why NF etching could possibly change the values of the T_2 coherence time as well as the FWHM value, the following comes to mind. It has previously been shown that especially the ODMR spectrum strongly depends on the state of the diamond surface. This has been especially true in cases where the NV center was close to the diamond surface [93]. When looking at the effectiveness of NF etching for improving FWHM values, we need to keep in mind that the FWHM value is limited by the internal distortion of the nanodiamond, and can thus not be reduced beyond a certain limit.

When considering the change of the T_2 coherence time, we can explain its change in a similar fashion to the explanation for the change of the FWHM value. In general, the NV center is affected by its magnetic environment. So for NV centers which are very close to the diamond surface, the surface noise could play a quite large role in its T_2 coherence time. However previous research has already shown that NF etching is able to condition sample surfaces, including diamond samples. It has also been shown many times that NF etching is able to smoothen sample surfaces, by e.g. removing structural impurities. Now in case of the NV nanodiamonds, due to the nature of its fabrication, there could be

structural defects as well as termination groups along the surface of the nanodiamond, which both can affect the NV centers T_2 coherence time. So logically, NF etching should be able to reduce the amount of structural defects as well as termination groups at the nanodiamond surface over ongoing etching duration. The impact of surface defects has been previously shown already [79]. Generally speaking, surface defects can create a defect level in the band gap of the diamond, which will then be occupied by an electron whose spin will influence the NV centers spin. Surface termination groups have also been shown the affect the spin coherence time of NV centers in diamond, as previous research has concluded that attached atoms to the diamond surface can influence the NV centers in it [80,94]. Another parasitic component along the NV nanodiamond surface is its dangling bonds. These dangling bonds are not able to covalently bond with another partner and are therefore occupied by unpaired electrons whose spin interact with the NV center [95]. Also, we have oxygen molecules which naturally adsorb themselves onto the diamond surface. Those oxygen molecules have a paramagnetic nature [96] and thus also affect the NV center spin. By considering these parasitic components, we can explain the improvement of the NV nanodiamond electron spin properties by the removal of said parasitic components by NF etching. More specifically, during the early time-intervals of NF etching, a lot of the nanodiamond surface defects as well as termination groups (or coating residue) could have been removed by NF etching. This should have happened in a steady rate up until the 60 min mark for the T_2 coherence time experiment and until the 90 min mark for the FWHM value experiment. For even longer NF etching durations than that, we found that the NV nanodiamond electron spin properties got worse and worse. This could be explained by an increased number of dangling bonds and adsorbed oxygen molecules

along the nanodiamonds surface. The adsorbed oxygen molecules theory seems especially likely since the NF etching eliminates termination groups as well as carbon atoms resulting in energetically unstable dangling bonds along the nanodiamond surface. These energetically unstable dangling bonds could attract reactive compounds in the air, which will then further affect the NV spin. One theory which we can definitely exclude as a possible explanation for the decrease of NV electron spin properties is the removal of too many NV centers by NF etching, since in e.g. Fig. 5.14 we received an NV signal throughout the whole NF etching distance as well as by pointing out the result in Fig. 5.16a. In regards to the different peak marks of the NF etching duration for T_2 coherence time (60 min) and FWHM value (90 min) we can simply point to the fact that we used two different types of nanodiamonds. The nanodiamonds for the T_2 coherence time experiment were around the size of 50 nm and only contained a single NV center on average. The nanodiamonds used for the FWHM value experiment on the other hand were larger nanodiamonds (200-300 nm) and included a higher number of NV centers (approximately 500 NV centers per nanodiamond). The reason for using two different nanodiamond types is simply that the NV-dense nanodiamond is much more suitable for ODMR applications, while the single NV nanodiamond is more interesting for specific applications such as quantum computing applications, where we are only looking for a single photon source.

The improvement of the cathode-luminescence signal depicted in Fig. 5.15 can be explained in similar fashion to the improvement of T_2 coherence times and FWHM values. NF etching conditions the nanodiamond surface and reduces the amount of structural defects along it. It seems therefore logical that the cathode-luminescence signal can be increased as well, since it is generally restricted by non-radiative defects on its surface.

To briefly sum up this chapter, NF etching could help improve the sensitivity and T2 time for various NV ND based applications, however our experiments have shown some great limitations to NF etching as well. First of all, the post-NF etching diamond surface is likely to re-adsorb gases and water in the air, which will negatively influence the NV spin performance. The optimal NF etching time in this experiment was found to be 60 min (T_2) and 90 min (FHWM), however electron spin values were obtained immediately after NF etching was performed. So in order to say how robust our technique is for improving NV sensing long-term, the electron spin values should be measured and compared again after some time (e.g. $T_{2,60min}$ vs $T_{2,60min(+1week)}$). Overall, the post-NF etching-benefit robustness is not well understood yet.

Another problem stems from the NV sensing performance for higher etching times. While we found that spin performance peaked at 60 min (T_2) and 90 min (FHWM), the increase was followed by a subsequent decrease of spin performance parameters (reaching even lower values than the initial state). In Fig. 5.16 we try to sum up this behavior. A possible reason for this could be that the benefits from NF etching (removal of surface defects, termination, etc.) saturate after a specific time, and the effects of dangling bonds and adsorptions start to overtake. We also need to consider the fact that NV centers close to the surface generally perform worse [78], and NF etching reduces the NV center depth. Reasons for this seem to be beyond the impact of surface impurities, and rather an issue of the charge loss of the NV^- centers (conversion to neutral NV^0) [97].

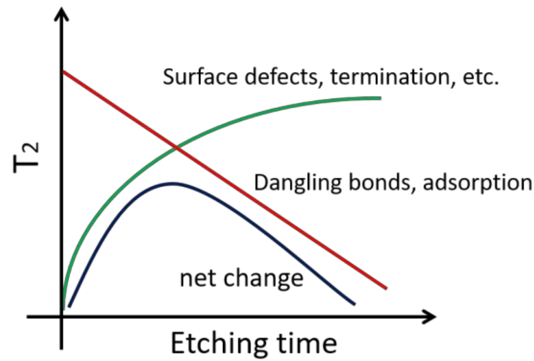

Figure 5.16. Net T_2 change over etching time

T_2 diminishing effects (NF etching caused increased adsorption and dangling bonds) overtake T_2 improvement after a certain time, resulting in an adverse effect on NV spin performance.

Another issue with NF etching improved NV sensing stems from the fact that stems from the fact that most bio-sensing applications immerse their NV NDs into liquids. In that case, the benefits of surface cleaning from NF etching could quickly be cancelled out again. Lastly, the peak performance NF etching time appears to differ between ND samples (60 min vs 90 min). When considering that NDs differ for each sensing application, the optimal NF etching time needs to be readjusted for each experiment as well. Adding to that, even NDs of the same type suffer from natural structural (i.e. size) and material (NV number) variances. Therefore, it might be that optimal NF etching parameters should be found for each respective NV ND.

However, some practical limitations aside, NF etching could be able to push some applications just enough to reach a new dimension of sensing (Fig. 5. 17). Also NV bulk diamonds should in principle be improved by NF etching as well, due to the same reasons as NV NDs (surface noise removal). In addition to that, NV qubit applications are often

performed under cryogenic conditions, hence re-adsorption impacts might be reduced as well.

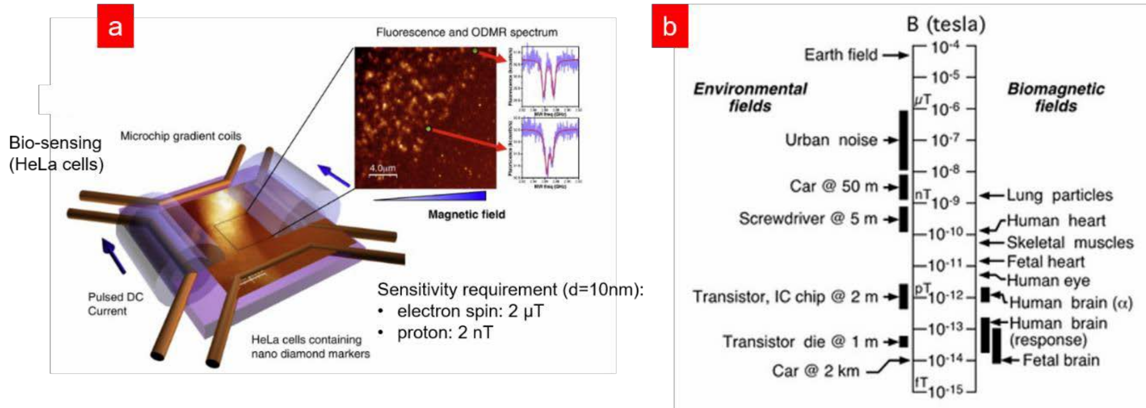

Figure 5.17. Target sensing applications for NF etching [98, 99]

(a) HeLa cells experiment based on NV ESR sensing. Inset showing fluorescence signal of NV NDs including their individual ESR spectrum. (Reprinted with permission from [98]. Copyright 2014 Elsevier Ltd.) (b) Magnetic field sensitivity requirement for various applications, showing that especially bio-sensing applications require extremely high sensitivities (Reprinted with permission from 99]. Copyright 2003 Elsevier Ltd.).

Chapter 6.

Synthesis of Ag nanoparticles by NF based photo-reduction of Ag^+

6.1 Background

Although in our previous experiments we have proven the effectiveness of e.g. NF etching on surface conditioning, there has first of all still not been a direct proof of NFs for those experiments, and secondly, the parameters needed for NF etching are still quite unclear. For example, we know that NF etching can be achieved by illuminating the sample surface with light sources lower in energy than the direct photo-dissociation energy level of the etching agents, however the exact importance of parameters such as the wavelength and light power are still unclear. Furthermore, we would like to examine whether NF etching has a linear or non-linear dependency to the incident laser power. Understanding the power dependency of NF etching might help us understand what exactly causes the photo-dissociation in the first place (e.g. second harmonic generation, two-photon absorption, etc.) All these possible candidates should increase differently (i.e. linearly, exponentially, etc.) with increasing power.

6.2 ONF power dependency

Previous research has tried to examine the power dependency of NF etching by observing the change of the etching rate on nanodiamonds depending on the incident laser power. This time, instead of applying NF theory for the etching of samples, we would like to synthesize something with the help of NFs. The general idea is basically that etching is overall difficult to evaluate, due to the sturdiness of inorganic materials, especially when considering the theoretically low magnitude of localized ONFs when looking at a

macroscopic scale. Hence we decided to synthesize silver nanoparticles (NPs) with the help of ONFs. In Fig. 6.1 the NF etching experiment has performed with three different far-field laser powers (0.5, 0.9 and 3.0 mJ). The far-field light source for this experiment was a nano-second laser of 266 nm (pulse width = 20 ns), with ambient O_2 molecules (242 nm) as the etching agent. In the bottom images of Fig. 6.1 we can clearly see that the overall sample surface appears to have been etched by the nano-second laser.

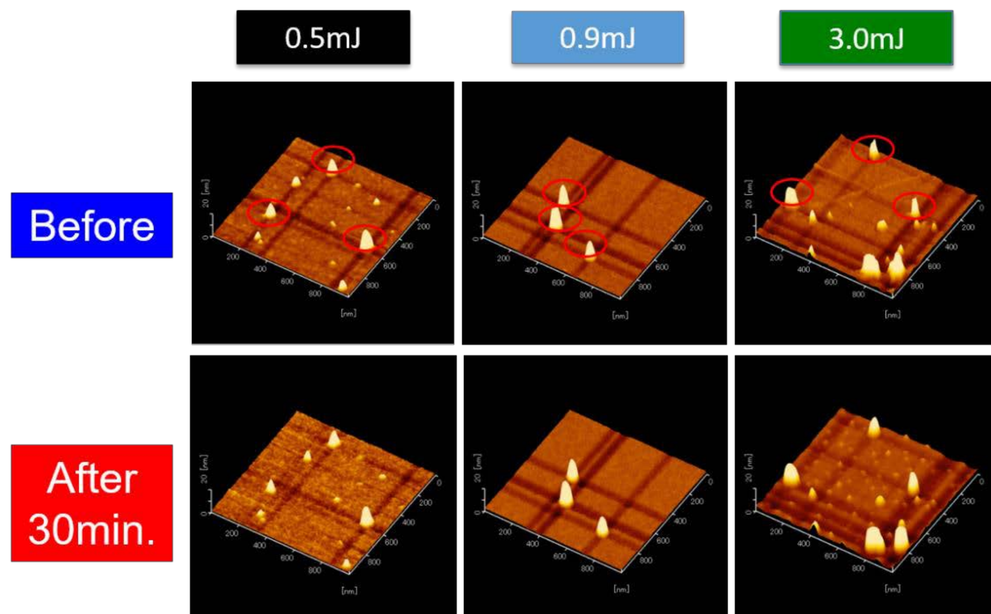

Figure 6.1. Nano-second laser power-dependent etching [100].

(top) AFM images of nanodiamonds before NF etching. (bottom) AFM images of nanodiamonds after NF etching. (Reprinted with permission from [100] Copyright 2017 Springer-Verlag GmbH Germany)

For evaluating the volume reduction of the nanodiamonds, let us look at Fig. 6.2a.

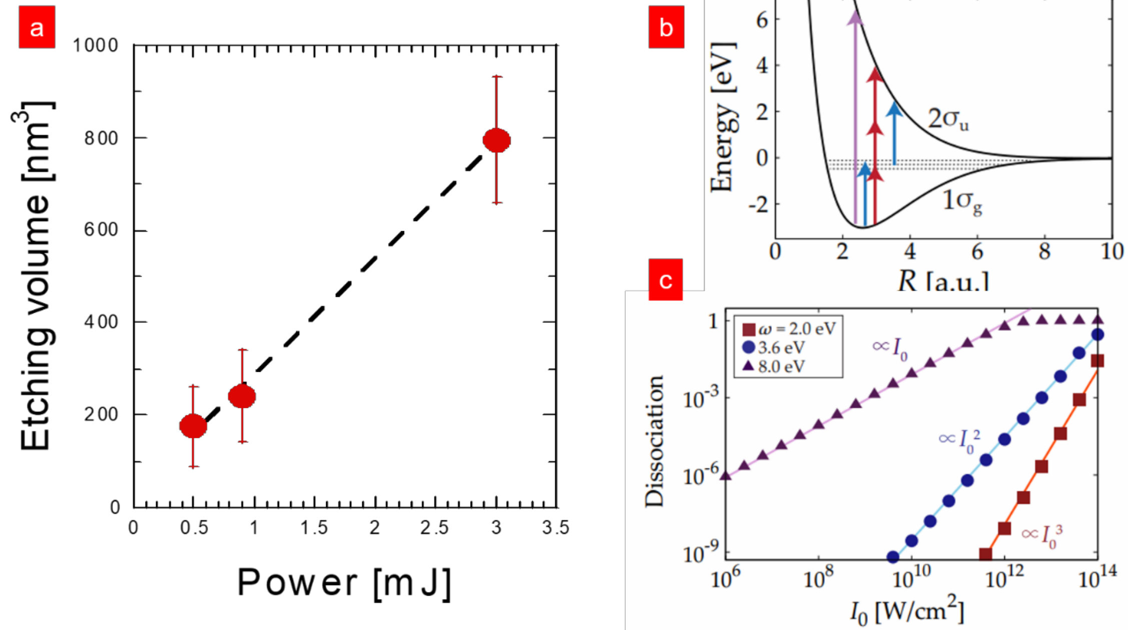

Figure 6.2. Power dependency of ONFs [100] and [38].

(a) Etching volume of the nanodiamonds linearly-dependent to the nano-second laser power (Reprinted with permission from [100] Copyright 2017 Springer-Verlag GmbH Germany). (b) Dissociation energy for H_2^+ *obtained from Born-Oppenheimer equation. (c) Dissociation over laser input power shows non-linear dependency for ONFs ((b)&(c) Reprinted with permission from [38]. Copyright 2016 American Physical Society.)*

In Fig. 6.2a, the etched volume seems to increase linearly with the laser power. However, we need to consider the fact that we used a nano-second (pulse width = 20 ns), instead of a continuous, laser for this experiment. These are naturally more reactive with sample surfaces and thus makes it difficult to conclude the power relationship of NFs when using continuous lasers. In his paper [38] M. Yamaguchi and K. Nobusada calculated the dissociation rate of H_2^+ in dependence of laser power (Figs. 6.2b-c), based on a non-Born-Oppenheimer Schrödinger equation. Hereby they found that the non-uniform ONF opens an additional, electric-dipole forbidden, excitation path, which reaches the dissociation

band through vibrational states. Also they found that the H_2^+ dissociation via this additional path has a $\propto I^2$ dependency on the ONF power *I*.

By using Au NPs (average diameter of 6nm) as an ONF source (under the far-field illumination) in combination with a Ag-ion solution (high quantum yield) I hope to photosynthesize Ag by the ONFs around the Au NPs. NF based synthesis was chosen over etching, since it is easier to evaluate the change under microscopy (higher rates). Then by evaluating the synthesized Ag volume over ONF power I hope to experimentally confirm the $\propto I^2$ dependency which was theoretically calculated by M. Yamaguchi and K. Nobusada. Additionally, the results in this chapter will gives us future insight for the experiments in Chapter 4 and Chapter 5 as well, since the results in this chapter help us to obtain the ONF power dependency. After that, the experiments in Chapter 4 and Chapter 5 could be performed again as a power-dependent experiment, and compared with the dependency obtained in Chapter 6.

6.3 NF based silver synthesis

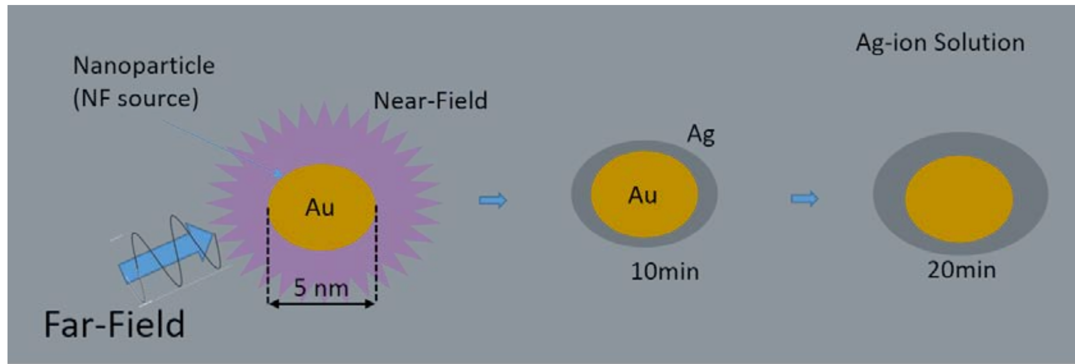

Figure 6.3. Scheme of NF based silver reduction amongst gold NPs

Principle of silver synthesis by ONFs. Pink sphere representing the locally induced ONF outside the gold NP.

The silver ions are solved in a photo-sensitive solution, and can be reduced to charge-neutral agglomerates when illuminated by the right wavelength. The core principle is depicted in Fig. 6.3. Au NP (~ 6 nm) are submerged into a photo-sensitive silver ion solution. The photo-initiator, Irgacure 819, has a close to unity quantum yield for its photo-cleavage [101]. The solution contains 0.1 wt% $AgNO_3$ and 0.2wt% Irgacure 819. The wavelength of the far-field light source has to be above the absorption spectrum of the solution, meaning that there is no direct photo-generation of silver aggregates due to the far-field light source. Similar to the principles of Chapter 4 and Chapter 5, the photochemical reaction is caused as a combination of the far-field photon and the NF photon. The ONFs are induced across the Au NPs. Contrarily to Chapter 4 and Chapter 5 (NF based etching), ONFs are used in order to synthesize silver aggregates along the Au NP surfaces (NF based synthesis). The Au NPs are evaluated through a transmission electron microscope (TEM) and evaluated in size and shape before far-field illumination

and after far-field illumination. In other words, TEM observed silver aggregates along the Au NP surface are used as an indicator and direct proof for the existence and quantity of the localized ONFs. The Au NPs were chosen to be ~6 nm since they show the lowest natural absorption (Fig. 6.4) for the wavelength we used (since we want to exclude other optical phenomena, such as conventional plasmon resonance).

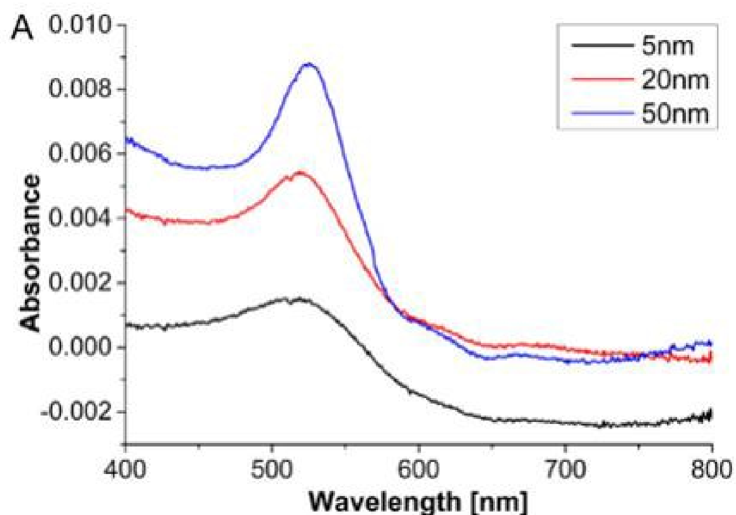

Figure 6.4. Plasmon resonance spectrum for gold nanoparticles [102]

Absorption spectrum for Gold nanoparticles of varying sizes; 5nm (black), 20nm (red) and 50nm (blue). (Reprinted with permission from [102]. Copyright 2015 Elsevier B.V.)

6.4 Results and Discussion

Before testing the effectiveness of NFs for photo-inducing silver nanoparticles, I decided to check the general effectiveness of the silver-ion solution by simply inducing silver nanoparticles with a far-field light source. For this purpose, I used a far-field source of 325 nm wavelength (He-Cd laser). In Fig. 6.5 we can see how photo-induction of silver nanoparticles looks like through the TEM. In Fig. 6.5a we have a typical TEM image of the before-illumination state, in which we can only see a couple of gold nanoparticles,

which are included in the initial solution. After just illuminating the sample for around 120s, we can see a now typical TEM image of the solution (Fig. 6.5b) that shows that a vast amount of silver nanoparticles has been induced within the solution.

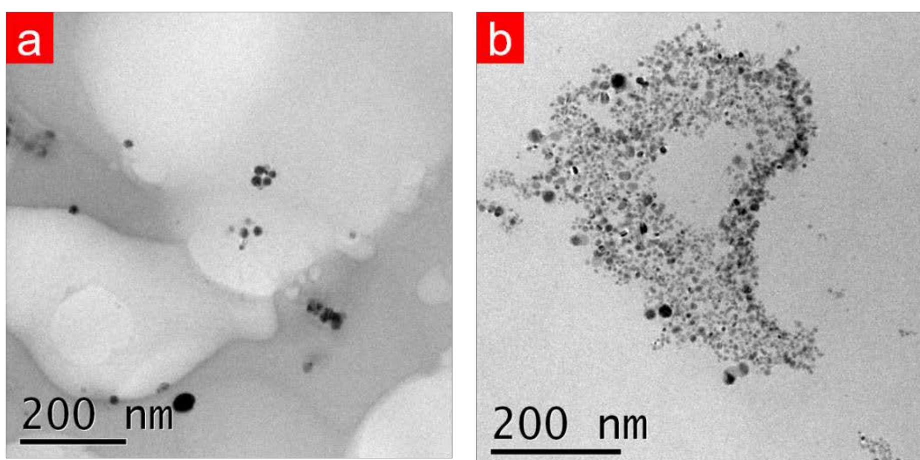

Figure 6.5. Silver nanoparticle synthesis caused by 325 nm light absorption

(a) Typical TEM image before illuminating the photo-sensitive solution with a 325nm laser. Visible are only a couple of gold nanoparticles. (b) showing typical TEM image after 120s of 325nm illumination. We can clearly see that a great amount of silver nanoparticles was induced.

This result confirms that the silver-ion solution can be used as an indicator for photo-induction.

In the following section experiments have been performed with an 808 nm light source, where the exact same gold nanoparticles have been observed before and after exposure. Hereby, and for all the following results, the values (e.g. diameter or volume increase) for each single laser power have been obtained as follows. An Au NP containing TEM grid has been observed through the TEM and its Au NP dimensions were measured. Afterwards, the TEM grid was being exposed to the respective laser wavelengths and powers while being submerged in the photo-sensitive silver-ion solution. After drying, the TEM grid was again observed under the TEM and the exact same Au NP from before were

checked in dimension again. This procedure happened once for every TEM grid, i.e. two TEM observations for each TEM grid or simply put; before and after light exposure. Three TEM observations for the same TEM grid are highly difficult to perform, due to the fragility of the grids. The result is that we cannot observe the dimensional change of the exact same Au NP over all laser-power-steps. So I decided to plot the relative dimensional change (since the observed Au NP for each power step are different from each other, and also have different initial dimensions) for each laser-power interval. Overall this type of setup allowed us to follow individual Au NPs for a precise understanding of the volume change (i.e. silver synthesis along the Au NP surface) over laser power, meaning it allows us to deduct their correlation behavior.

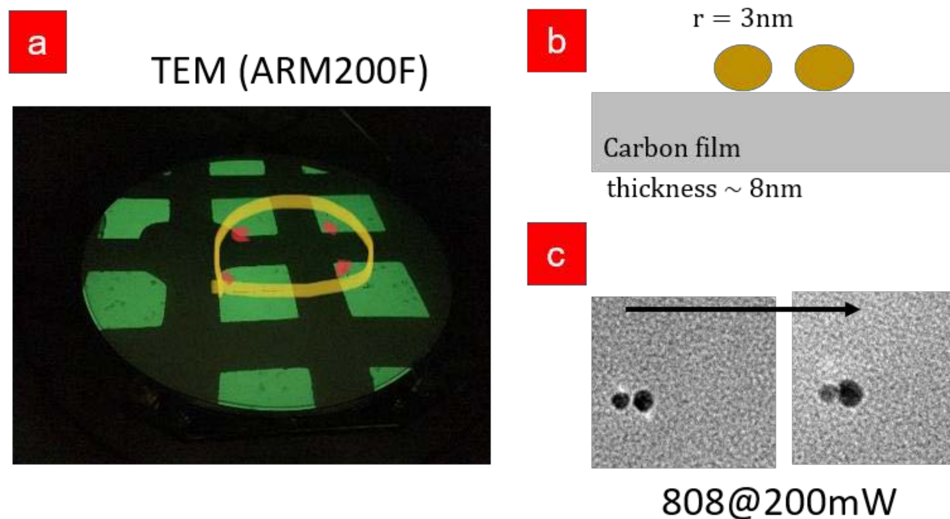

Figure 6.6. TEM image of Au NPs observed for topological changes

(a) TEM grid image showing markers for relocating Au NPs after experiments (b) cross-section of TEM grid, showing sample fragility due to thinness. (c) Sample image showing size change of Au NPs after 808nm exposure.

Fig. 6.6a shows how the same Au NPs can be relocated between experiments. The middle of the TEM grid (black circle) allows us to navigate to the same locations again. In

Fig. 6.6b we see the cross-section of the TEM grid and the attached Au NPs. Overall, the carbon film below the Au NPs is extremely thin and fragile, hence repeated exposure to the solution and laser illumination increases the risk of tearing the carbon film. Fig. 6.6c shows how the Au NPs change after illumination. The size increase is due to the deposition of photo-synthesized Ag (confirmed by EDS, see Appendix C4). The diameter increase after illumination is obtained by a computer vision software (National Instruments) (see Appendix C3).

In Fig. 6.7a we can see a typical TEM view of our Au NPs. The mean diameter and standard deviation of every single Au NP observed in this section can be seen in Fig. 6.7a as well. Those values were obtained from the histogram of the Au NP size as show in the inset of Fig. 6.7a. On the right-hand side (Fig. 6.7b) we see a brief scheme of how the ONF is expected to photo-induce the silver synthesis. The silver synthesis should only occur within the ONF, and as a result the Au NP size is expected to grow (attached Ag). In this section we use an 808 nm laser (exposure time: 15min @200mW, power density: 133mW/cm^2) and a He-Cd laser (325nm) (exposure time: 1.5min @9mW, power density: 144mW/cm^2).

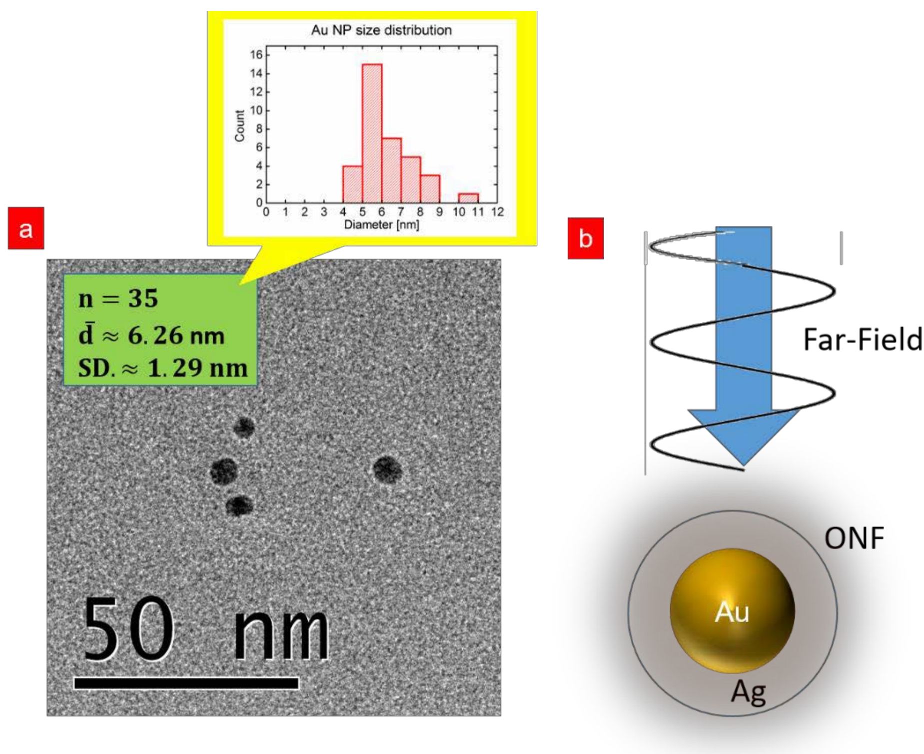

Figure 6.7. Initial size distribution of Au NPs

(a) In total 35 distinct Au NPs were observed. Inset showing Au NP size distribution (b) Scheme of particle growth (i.e. Ag synthesis (blue sphere)) within the ONF (orange sphere).

In Fig. 6.8a the relative increase of the maximum Feret-Diameter (i.e. the maximum diameter) of each gold nanoparticle has been plotted versus excitation power. The Volume in Fig. 6.8b has been calculated from the mean radius value in Fig. 6.8a. We can see in Fig.

6.8b that the relative volume increase appears to have a $\propto I^2$ dependency. Our $\propto I^2$ dependency seems to be dependent on a single measurement point (I=2000mW), however this value represents the mean volume increase for 5 individual Au NPs, and should therefore be reliable. This result is rather interesting because in Fig. 6.2a [100] a linear dependency over laser power was found. From the absolute added volume for each step,

we estimate the average number of added Ag-atoms per second on a single Au NP to be 10.47(@200mW) and 496(@2000mW).

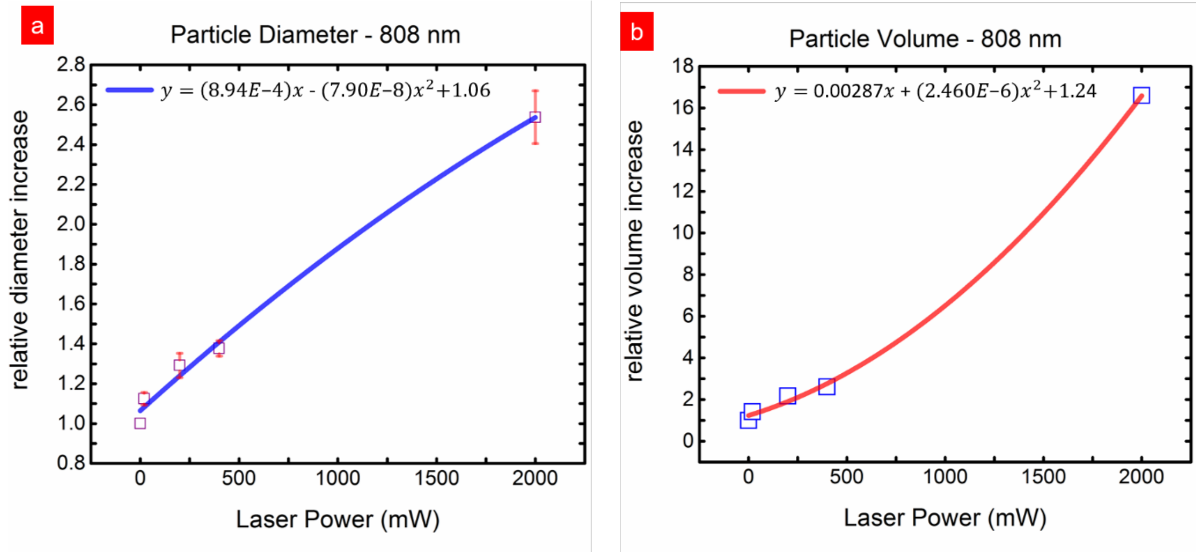

Figure 6.8. Power-dependency for ONF-based Ag synthesis

(a) Relative increase of Au NP diameter (pink squares. (b) Relative increase of Au NP volume (pink squares) shows rising behavior of $\propto$ �^{2} *(I: excitation power).*

In order to ensure that photo-synthesis is being caused by ONFs, previous experiment (808nm @200mW) was repeated without including the photo-sensitive agent, Irgacure 819. Fig. 6.9 proofs that NF-effects outweigh thermal effects and thus confirms that our reaction is mostly ONF dependent.

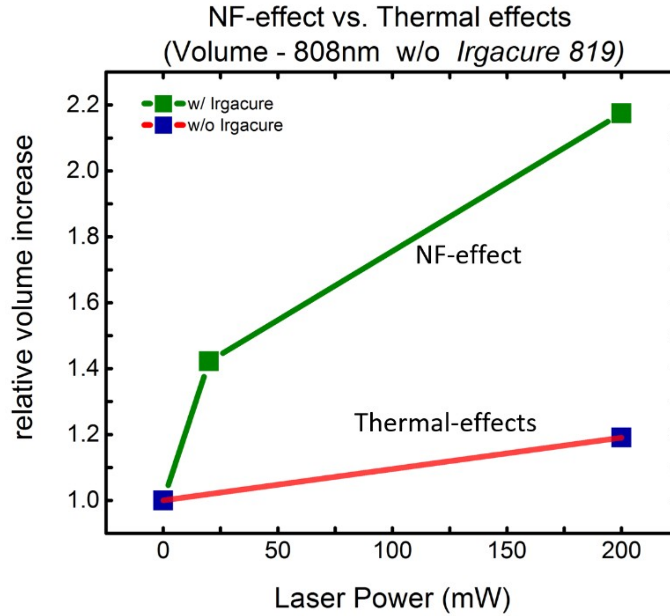

Figure 6.9. NF-effects vs. Thermal-effects in Ag synthesis

The 808nm experiment (200mW laser-power) compared between with Irgacure 819 (green squares) and without Irgacure 819 (blue triangles).

In the following, Fig. 6.10a, shows the relative volume dependence of FF-based excitation (Fig. 6.10b). Comparing the relative volume increase between 808nm (ONF) and 325nm

(FF), we conclude that ONFs behave non-linear ($\propto I^2$) to laser power while FFs show a saturating power-dependency, with t1=8.37482. ONF-based photoreaction is dependent on forbidden intermediate energy levels, i.e. the absorption of various photons, so the I^2 seems to be natural. It seems also obvious that the power-dependency of FF-based photoreaction will saturate, since at some point the incoming photons far outweigh the available Irgacure 819 in the vicinity of the Au NPs (ONF is not saturated due to much lower number of total photoreactions).

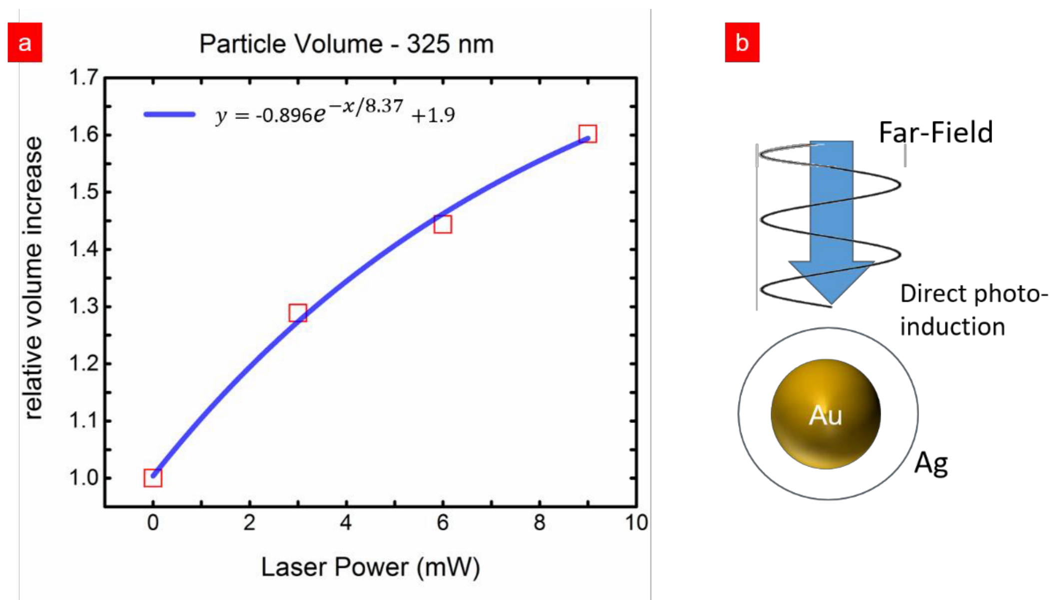

Figure 6.10. Power-dependency for FF-based Ag Synthesis

(a) Normalized increase of Au NP volume (pink squares) shows saturation for far-field based excitation (t_1 = 8.37482). (b) Scheme of particle growth (i.e. Ag synthesis) induced directly by far-field light exposure.

To illustrate how the FF-based photoreaction saturates, Fig. 6.11 should be understood first. In a back-of-the-envelope calculation the amount of average Irgacure 819-molecules and

Ag^+-atoms at any given time within the vicinity (~2� �of an Au NP (see Fig.6. 11b), is approximately 0.929 and 0.229 for Irgacure 819 and Ag^+, respectively. Hereby the value 2nm should be a good guess since the average length of the Irgacure 819 molecule is around 1nm. These values further make it seem very reasonable that a saturation value for FF-based synthesis exists.

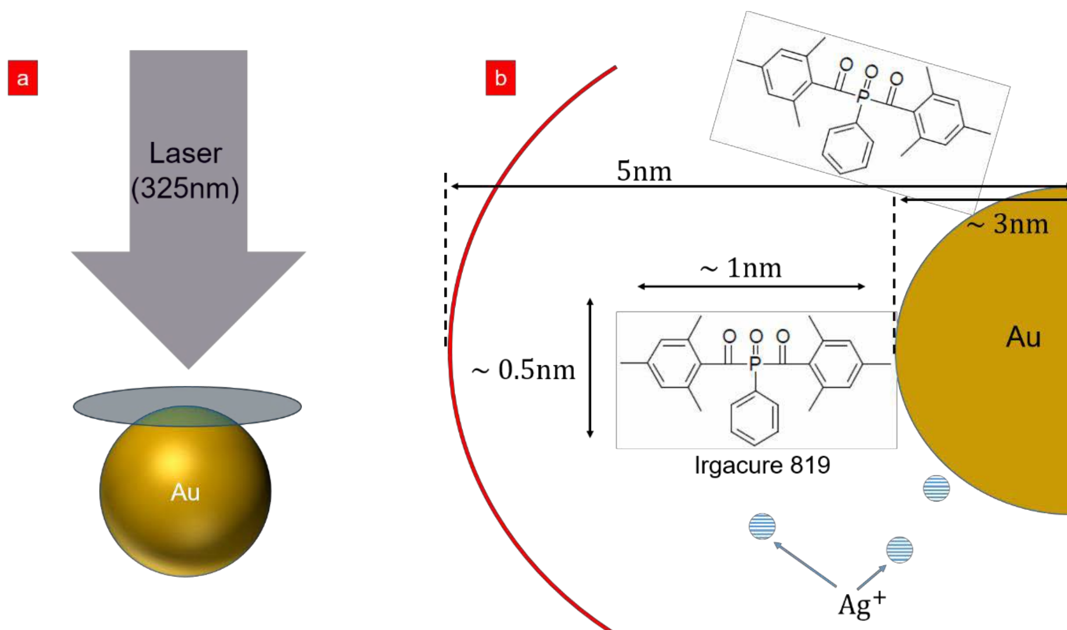

Figure 6.11. Illustration of FF saturation due to limited availability of photo-components.

(a) Amount of photons (blue circle) that will cause saturation, (b) due to scarcity of free photo-components (i.e. Irgacure 819 & Ag^+)

There are some obvious limitations to this experiment however. First of all, since the Au NPs increase over exposure time, the system does not have the same conditions anymore (i.e. resonance shift and change of net collected photons) and a comparison between different power-steps gets more ambiguous. In Fig. 6.8, we saw an overall increase of the Au NPs from 6 nm diameter to approximately 15 nm diameter. Although Fig. C.2b in Appendix C indicates that the absorption spectrum for Ag NPs in similar size (e.g. 10–30 nm) is quite similar, we still have a change of collected photons over different particle sizes. Furthermore, Fig. 6.12 shows the simulated electric field intensity (under 808nm light irradiation; linearly polarized) amongst the Au NPs depending on their size. We can see (Fig. 6.12a) that under the same laser conditions, 2) and 3) appear to have a higher local electric field intensity peak than 1) (note that in Fig. 6.12a the dark red spheres represent

the additionally attached Ag onto the Au NPs). 2) and 3) are compounds, consisting of an Au core (identical to 1)) and Ag outer mantles.

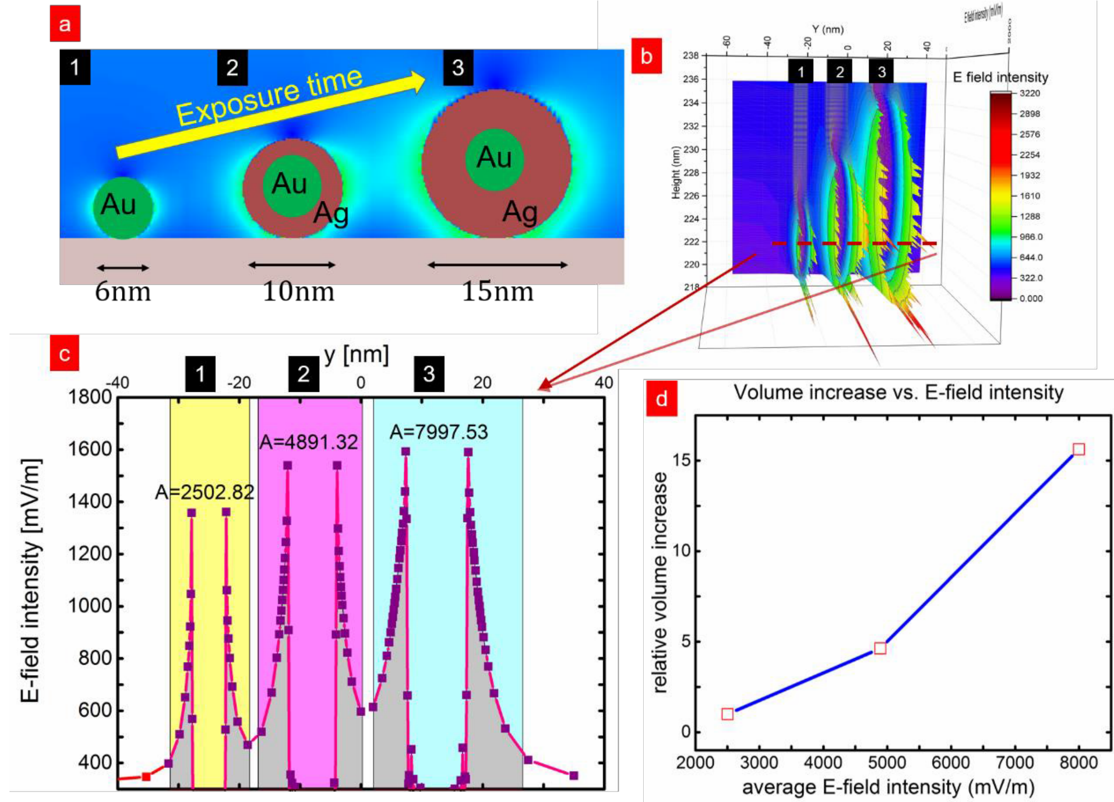

Figure 6.12. Simulation of size dependency of 808nm experiment

(a) Size distributions for Au NPs 1)-3). 1) consists purely out of Au (green), while 2) and 3) have an additional Ag mantle (dark red) y-polarized 808nm CW laser perpendicular to ground substrate (grey).The minimum grid size was hereby 0.1 nm. (b) 3D surface heatmap of E-field intensity around the Au NPs showing higher peak intensities as well as overall intensity volume for larger spheres. (c) Cross-section (red line, see (b)) depicting E-field intensity integrated above baseline (E-field intensity=300). (d) Showing relationship between volume increase and average E-field intensity (from (c)).

Fig. 6.12c depicts the cross-section area of the electric field intensity around each NP. In [112] the surface plasmon resonance (SPR) related scattering cross-section (σ_{sca}) and adsorption cross-section (σ_{abs}) for metal nanoparticles was found to increase by $\propto d^6$ and $\propto d^3$, respectively (d = particle diameter). This means that the calculated

values ��� and �� for our (d=15nm)-NP should be $9^6 = 531441$ times higher for ��� and 729 times higher for �� than the (d=6nm)-NP. However, the results in Fig. 6.12d directly contradict these assumptions. We can thus assume that the Au/Ag NPs are off-resonant for the 808nm excitation. As such, the $\propto I^2$ dependency obtained in Fig. 6.8b should not be caused by the changing resonance properties of the particles.

In addition to having a changing system (size), the results in Fig. 6.8 indicate that there is a rather significant difference between the theoretical starting value (at position I = 0) and the first measured step (I = 20mW). This error margin could stem from fact that the computer vision software is not able to perfectly transform the raw TEM image into an identical binary image, since the Au NPs borders in the TEM image are always slightly blurred. Furthermore, while Fig. 6.9 shows that thermal effects are rather small for measurement steps between 20mW and 200mW, future experiments should include the thermal effects for higher laser powers 400mW and 2000mW as well, in order to conclude that the non-linearity is indeed due to ONFs. Lastly, the ONF power dependency ($\propto I^2$) in [38] was directly obtained (H_2^+ molecule photo-dissociation). However, in our case ONF based Irgacure 819 molecule dissociation will need to chemically interact with Ag-ions first and then congregate around the Au NPs, before it can be evaluated, adding more layers of complexity.

Interestingly, Fig. 6.8b and Fig. 6.2a show a different dependency on the ONF power. One could speculate that due to their smaller size and their generally higher optical resonance, Au NPs should have relatively stronger ONFs than Nanodiamonds.

To sum up, the results obtained in this chapter hint at a $\propto I^2$ dependency (Fig.6.13a), and could therefore potentially be a confirmation of the simulated ONF power dependency (Fig.6.13b). However limiting factors need to be more thoroughly understood first.

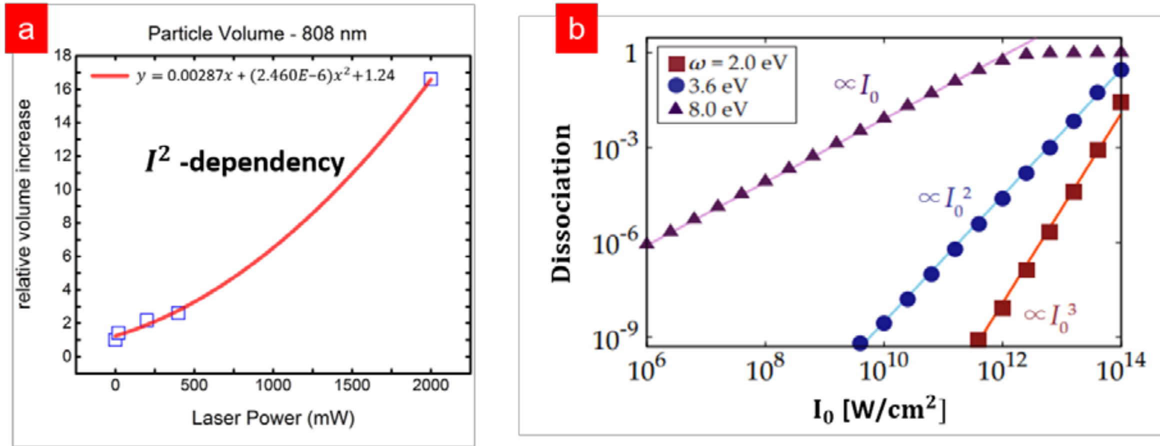

Figure 6.13. Theoretical and experimental ONF power-dependency comparison [38]

(a) Results for 808nm light source hinting at a ∝ I^2 power dependency. (b) Theoretical model showing a ∝ I^2 power dependency for ONF caused 2-step excitation (Reprinted with permission from [38] Copyright 2016 American Physical Society.)

Chapter 7. Conclusion and Outlook.

7.1 Summary and outlook for Chapter 4

In Chapter 4 we were able to control the structural width of the photoresists when using the 325nm laser source. Hence NF etching could be promising as a counter-measure for reducing the amount of full and half-bridges in the increasingly smaller CD values in the high-end semiconductor industry. At the same time, both lasers (325nm and 405nm) showed that they were able to reduce the surface roughness at the top of the photoresists. In principle, this means that NF etching can be used as well in order to improve LER and LWR values. Successfully using NF etching to reduce stochastic effects in EUV lithography would greatly relieve the RLS tradeoff relation, meaning that companies are able to focus on other aspects while saving production costs. The currently only thing keeping CARs from manifesting themselves as the industrial standard for EUV as well is their high roughness. However, we need to consider that industrial applications rely on more complex resist patterns. Since NF etching was only studied on the continuous line/trench pattern, examining the NF effects first on more complex pattern compounds would be useful.

7.2 Summary and outlook for Chapter 5

In Chapter 5, the NF etching parameters from Chapter 4 with the greatest etching rate (325nm) are applied on NV NDs, resulting in a structural change of the NDs as well. The NV spin performance, which is negatively affected by surface noise, seems to be improved initially with NF etching times, but decreases again with ongoing etching times. The peak NV spin performance value was hereby found to be 60 min for the T2

measurement and 90 min for the FWHM measurement. NF etching could be useful for improving NV sensing applications, however long-term post-NF etching NV spin performance stability needs to be further studied.

7.3 Summary and outlook for Chapter 6

In Chapter 6, the results for the 808nm laser hint at an I^2 power-dependency (ONF), while the results for the 325nm laser let us assume a saturating power-dependency (FF). However, changing conditions due to the Au NPs size increase (resonance shift & higher photon collection) might complicate a direct comparison between the power-steps. The impact of thermal effects for higher laser powers (e.g. 400mW and 2000mW) should also be examined, in order estimate its overall contribution to the observed non-linear behavior.

To conclude, the main idea of this thesis was to take advantage of the knowledge obtained in Chapter 4 (width control & surface smoothening) in order to improve other industrial applications which could benefit from the surface conditioning offered by NF etching. The choice fell on NV centers in NDs (Chapter 5), due to their high dependency on their surface state. Furthermore, direct chemical component analysis (e.g. EDS or XPS) to evaluate NF etching performance has always been tricky due to the small size of the samples. Hence the results in Chapter 5 could be used as evidence for the surface chemistry change caused by NF etching. The results in Chapter 6 could be interesting as well, if we in future can find a way to stabilize the experimental conditions (thermal, system size change). Overall, using photochemical reactions to study about ONFs can be effective, however under the assumption that limiting parameters are fully understood.

7.4 Final summary and outlook

In a general outlook, future applications for NF etching are in my opinion especially attractive in the EUV lithography industry. EUV lithography is the current high-end fabrication technique in the semiconductor industry and will most likely remain so for the foreseeable future. Currently the main problem for EUV is finding a suitable photoresist. Commonly used CARs in DUV lithography don't seem to suffice for EUV anymore, since stochastic effects are large (especially at 5 or 7 nm node dimensions). However I believe that most of these stochastic effects (e.g. bridges or roughness) can be tackled well with the techniques presented in this thesis. The structural change caused by NF etching with 325 nm was rather large, so the optimal etching time would have to be readjusted for different samples. Although photoresist patterns in EUV lithography will be significantly smaller (less than a tenth) than the photoresists presented in this thesis, I believe that the results in Chapter 5 (50 nm sample) and Chapter 6 (6 nm sample) show that NF etching should have no issues with smaller photoresists. It would be nice to perform some NF etching experiments on some current EUV photoresist patterns. I also believe that the improved NV ND spin properties show potential for future applications, albeit not as promising as the organic photoresist results. Future experiments need to confirm the long-term stability of the NF-etched NV centers, since re-adsorption seems to be a big problem. The same issue persists when immersing NV NDs into liquids (after already improving their spin performance with NF etching), since the diamond surface will get quickly contaminated with impurities again. On the other hand, while the results from Chapter 6 seem quite interesting, more experiments are definitely needed in order ensure that the I^2 dependency stems from ONFs indeed. Hereby, examining the impact of thermal effects for

higher laser powers has to be one of the top priorities, as well as finding a system which doesn't change its conditions. While I think that the 6nm Au NPs are very suitable for ONF experiments, it might be better to confirm the ONF caused photo-dissociation through ways other than Ag synthesis, e.g. photo-current measurement.

Appendix A.

Methods and analysis for the experiments presented in Chapter 4

A.1 Atomic force microscopy (AFM) with L-Trace II

The Atomic-Force Microscopy (AFM) a high-end type of scanning probe microscopy (SPM), and it allows resolutions exceeding the optical diffraction limit by a factor over 1000. The AFM large stage unit L-Trace II has been developed by the Hitachi High-tech Science Corporation. For my measurements I will be using the AFM5000 series apparatus. More precisely, the system software supports a Dynamic Force Microscopy (DFM) mode, which means that the system possesses a hybrid feature of the fundamental contact mode and true-non contact mode. Furthermore, the software of our system supports the Sampling Intelligent Scan (SIS) feature, which basically means that the system is able to cope better with inhomogeneities, such as holes or scrapes, on top of the sample surface.

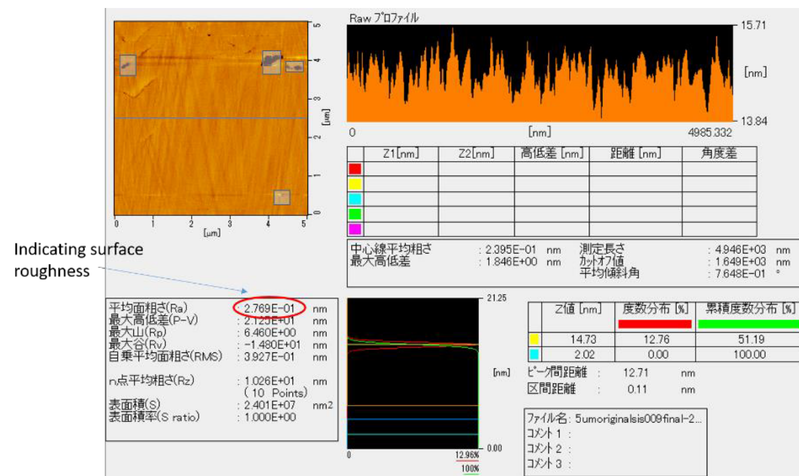

Figure A.1 User interface for inbuilt AFM roughness evaluation software.

Evaluating the sample surface roughness with an AFM-specific software. The circled (red) value indicates the mean surface roughness of a selected area inside the scanned area.

The above picture is showing the roughness analysis of a diamond sample surface. After the L-Trace II cantilever sweeped over the sample surface, while measuring the height of every pixel, the software will provide a thorough analysis of the surface. On the top right side you can see the sideview of a specified area, controlled on the image console. This feature is useful when trying to examine the depth of holes or scratches. Also it comes in handy when ensuring the height of my pattern structure, Nano-pillars and Nanowires.

A.2 Surface roughness evaluation

One important method for analyzing the effectiveness of the NF etching is evaluating the change in its surface roughness. For that we have a fixed approach procedure. The expected mean value of the surface roughness (R_a) is described by the following equation:

$$R_a = \frac{1}{L}\int_0^L |z(x)|dx \cong \frac{1}{n}\sum_{i=1}^{n}|z(x_i)| \quad \text{(A.1)}$$

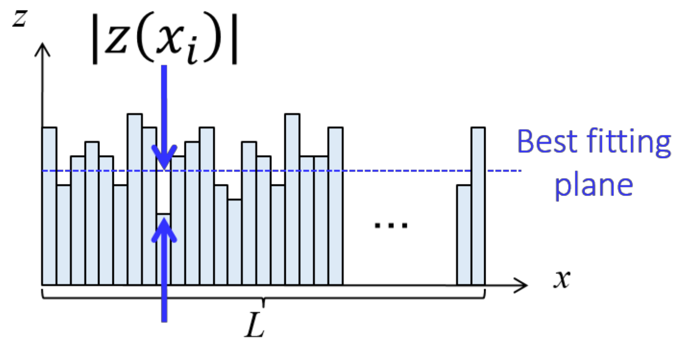

Average value of the roughness for an entire region

Figure A.2 Mathematical model visualizing the best fitting plane.

Evaluating the sample surface roughness with an AFM-specific software. Mathematical model visualizing the best fitting plane

Appendix B.

Methods and analysis for the experiments presented in Chapter 5

B.1 Charge of the NV Center

The nitrogen of the NV center is highly influencing the electronic structure of the defect and therefore also influencing its optical spectrum. However, early research of the NV center spectrum indicated the existence of two distinctively different NV centers. It then became apparent that those two different NV center were caused by different charging states of the NV center. Later it was found that the NV center is surrounded by five electrons. Three of those electrons originated from the three connected carbon atoms respectively, while two of the electrons originated from the nitrogen atom itself. However, electron spin resonance experiments indicated the existence of an even number of electrons within the NV center, because its spin should equal S = 1 [102]. Even up until now the charge state of the NV centers is not fully understand. For the working model of the NV center, people just imagine six electrons, where the additional electron originated from the surrounding crystal lattice [103,104]. As a result of the six electrons, we need to think of the NV center as a negatively charged point defect, which is also called NV^- as opposing to the NV^0, which is the NV center with only five electrons. The reason that sometimes NV centers are neutrally charged (only five electrons) is the lacking of an electron donor in the surrounding diamond lattice. Generally, people refer to the negatively charged NV center as the standard, regular NV center, since it is more interesting to study than the neutrally charged one.

B.2 Electronic structure model of the NV center

Generally speaking, the NV center can be viewed as a three-level-system, meaning a system hosting three potential electronic states. The first one is the ground state ^3A, and the second one is the excited state ^3E as well as the metastable ^1A [105], which energetically speaking lays between the ground and the excited states. The ground state and the excited state are triplet states [106], while the metastable ^1A state is only a singlet state, which was detected through examining the infrared spectrum of the NV center [107]. Although people were able to energetically confine the ^1A state in between the ground state and the excited state, they don't have much deeper knowledge about it yet though.

B.3 Optical properties of the NV Center

In order to prove the existence of the NV center, one can use relatively simple methods. For purely spectroscopically purposes, one can use standard components of conventional microscopy. Hereby, it is of special importance to use an objective lens with a sufficiently high magnifications factor (in general above 60) and a sufficiently high numerical aperture (in general above 0.4). These lay the foundation for photoluminescence measurements, in which we can examine and prove the existence of NV centers.

In the following figure, you can see the simplified structure of the 3-state energy structure of the NV center. The number "3" in front of the ground and exited states indicate the allowed number of spin-states ms. The spin multiplicity can hereby obtain values of up to $2S + 1$. If we imagine, as previously mentioned, that the total number of electron cause $S = 1$ for the negatively charged NV center, then it means that we have three possible spin-states ms. Hereby, every single spin-state m vector can obtain values between [-1, 0, +1]. This phenomena leads to a Zeeman-Splitting of the emission line, which can be confirmed

through ODMR [108] or electron spin resonance (ESR) experiments. Accordingly the same explanation can also be transferred to the singlet metastable state, although it doesn't host any spin-state varieties, although it has never been directly seen in experiments yet. The arrows indicate which electron movements can be caused by the respective color of light, or which electron movement causes the emission of a photon of the specific color. In the absence of a separate, external magnetic field, such as it is the case in ODMR measurements, you can see that the triplet spin-states energy levels essentially form only two different spin-states. The first, higher-laying spin-state would be the m = -1 and +1 spins, while the second, lower-laying spin-state would be the m = 0 spins. The so called "Zero-magnetic-Field" splitting, which means that there is no external magnetic field applied, averages about 2.87 GHz between those to spin-state levels. Normally for the resonant excitation of the NV center, people use laser light of the wavelength of 532 nm. However, it is also possible to achieve ground state to excited state transitions through excitation of the NV center into higher laying energy levels (above the excited state level) and then through rapid relaxation a returning into the excited state. This means that we can also excite NV centers with other laser wavelengths, however with a lower effectiveness than 532 nm. Through the falling back of the system from the excited state into the ground state a photon will be emitted. Hereby the energy difference between the two energy levels equals 1.945 eV, which equals a wavelength of 638 nm. This specific emission is called the zero-phonon-line, and is one of the main characteristics of the NV center spectrum. The Zero-Phonon-Line is a result of a direct smooth transition from the excited state to the ground state without any phonon interaction with the surrounding diamond matrix. However, the phonons inside the solid-state matrix of the diamond typically have enough

kinetic energy under room temperature, to excite a various number of phonons. As a result, the phonons are directly involved in the optical transition of the NV center, and they allow the system to reach higher and lower temporary energy levels, resulting in a broader spectrum. Therefore, we can't tell the exact energy value of the optical transition under ambient temperatures. With an increase of the temperature, the spectral lines will be broadened accordingly. The decaying path over the ^1A singlet state can cause a significant reduction of the NV center photon emission [109]. The same concept also applies to the neutrally charged NV center. Hereby the Zero-Phonon-Line averages about 575 nm. Hence we can differentiate between the two different charge states of the NV center through examining their Zero-Phonon-Line.

Whenever a system is in the quantum coherence state, it is basically in a superposition and can therefore be used for quantum

B.4 Hahn-Echo T_2 coherence time

Whenever a system is in the quantum coherence state, it is basically in a superposition and can therefore be used for quantum operations. The most common NV center coherence time measurement is done by the Hahn Echo method. Generally speaking, T_2 is the time required for the population to reach 37% (1/e) of its initial transverse total magnetization. T_2 coherence time can be affected by various factors, including static local field disturbances along the diamond

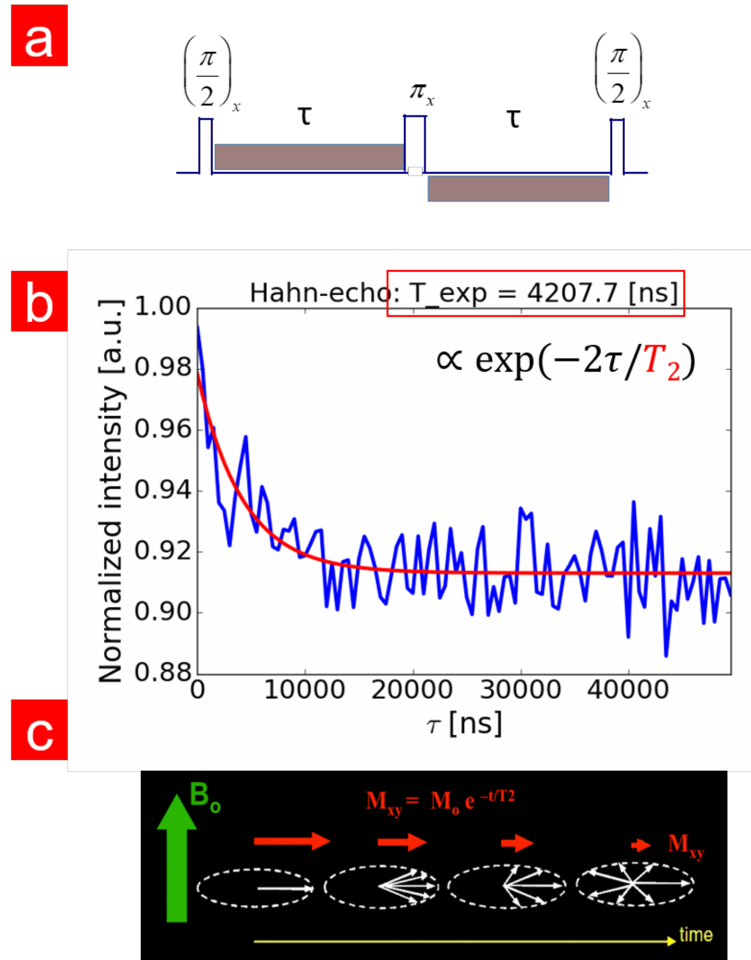

Figure B.1. Scheme of Hahn-Echo T_2

(a) Hahn-Echo pulse sequence for T_2 (b) Typical Hahn-Echo signal obtained by our confocal microscopy setup. Red curve is the automatically calculated exponential fitting curve. (c) Visualization of how decoherence of the total magnetization of the NV spin looks like (Reprinted with permission from [111]. Copyright 2018 AD Elster, ELSTER LLC).

B.5 Confocal microscopy & NF etching setup

Whenever a system is in the quantum coherence state, it is basically in a superposition In order to obtain the electron spin properties of the NV nanodiamonds, i.e. the ODMR and Hahn-Echo T_2 signals, I used a confocal microscopy setup. This setup enabled us the observation of a single NV nanodiamonds over the whole duration of NF

etching (Fig. B.2). The NF etching sequence was applied in 30 min intervals, which enables us a time-dependent evaluation of the electron spin properties of the NV nanodiamond, as well as the earlier mentioned change in the size of the nanodiamonds (Fig. B.2).

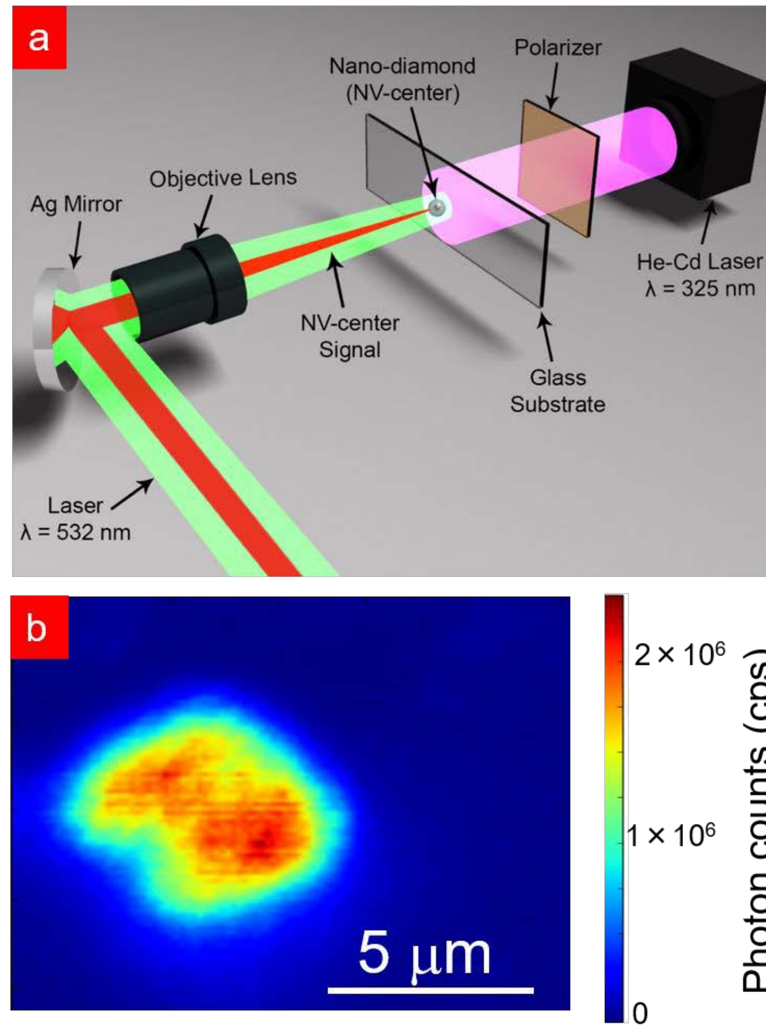

Figure B.2. Confocal microscopy setup combined with NF etching [91]

(a) Schematic view of the experimental setup. (b) Typical 2D fluorescence mapping of the NV nanodiamonds (500 NV type). (Reprinted with permission from F. Brandenburg et al. Sci. Rep. 8, 15847 (2018). Copyright 2019 Springer Nature Publishing AG)

In Fig. B.2a we can see the general setup of the confocal microscopy setup. This setup is the simplified version of the confocal microscopy setup for NV center sensing.

Some advanced setup arrangements, such as the two avalanche photodiode (APD) setup or the microwave control, are not shown in this image. In general, confocal microscopy setups allow the user to obtain high resolution images of their samples. The laser has been manufactured by Laser Quantum and emits light of the wavelength 532 nm at a max power of 250 mW. The collimated monochromatic and coherent beam of green light is characterized in the TEM_{00} spatial mode, meaning a continuous laser intensity distribution without multiple amplitude maxima. It is possible to control the laser power by a software specially provided by Laser Quantum. For that the laser source needs to be connected through its COM (RS-232) connector. The linearly polarized laser beam will next pass through an acousto-optic modulator (AOM), which is needed for pulsing the laser beam. This feature is needed for advanced measurements, such as the ODMR. Through the AOM it is possible to realized nano-pulsed laser sequences. However, the downside of using the AOM is that the laser beam will not be in the TEM_{00} spatial mode anymore after leaving the AOM. The two-mirror arrangement after the AOM ensures that the laser beam has a sufficient degree of freedom when trying to reach the objective lens of an optical fiber. It is also important that the light incidents into the objective lens of the optical fiber as perpendicular as possible. This will reduce scattering losses. Optical fibers normally consist of two objective lenses and the fiber itself. The first objective lens will focus the relatively speaking broad laser beam into the small fiber. Our fiber is specialized for wavelengths between 460 – 700 nm (product number is missing). The second objective lens ensures that the laser beam will be transformed into a parallel beam again. The optical fiber is useful because it allows an easy re-arrangement of the laser beam path, while at the same time ensuring that the laser light will be close to the TEM_{00} spatial mode again after

leaving the optical fiber. Next the laser beam will enter a beam expander in order to ensure a laser beam width that is high enough to fill the whole entrance of the final objective lens. The beam expander has been provided by Thorlabs and consists of UV Fused Silica. Furthermore the beam expander has an anti-reflection coating, which ensures that less light is lost at the glass-air interfaces. The beam expander will double the laser beam width to a diameter of around 2 cm. The laser beam path will now be reflected by a beam sampler, which reflects considerable amounts of the green light, while transmitting nearly all wavelengths above that. This means that the fluorescence of the NV center can easily pass through the beam sampler, while the returning green laser light will be reflected. From the beam sampler the laser beam will now be reflected by a mirror into the sensing system. The sensing system consists of a piezo stage, P-517.3CL, which has been manufactured by Physik Instrumente. The P-517.3CL is a nanoscale sensing system, which is made out of piezo material. This allows a step resolution of up to 0.3 nm over a range of 125 um and 25 um in X/Y and Z directions respectively. The piezo stage is connected over three channels to a signal amplifier as well as a voltage controller (more details about the controlling will follow in the next section). An objective lens is mounted on top of the Piezo Stage, through a specially designed adapter, whose details will be described in the following sections. The objective lens UPLSAPO60XO has been manufactured by Olympus and is oil-immersion based lens with a high numerical aperture (1.4 NA). The working distance is around 0.15 mm and the magnification factor is around 60. Those special features of the objective lens make it exceptionally good at detecting weak fluorescence emissions, and enables a sharp, clear image acquisition without any color shifts. Also the transmittance band of the objective lens make it well suited for laser light

of the wavelength 532 nm. In general, the objective lens will be concentrating the laser beam onto a small spot inside our diamond sample. The spot size is ideally equal to the wavelength of the corresponding light wavelength, in our case 532 nm. After the NV center has been excited by the green laser, it will emit its fluorescence (673 nm, but reaching into the infra-red spectrum) signal, which will return through the exact same laser path. First of all the fluorescence signal will be gathered by the objective lens and from there automatically introduced back into the same laser beam path of the green light. However, as mentioned earlier, the beam sampler prefers to transmit light wavelengths of over 532 nm, meaning that while considerable amounts of the returning green laser light will be reflected, most of the reddish fluorescence light will pass through the beam sampler. Next the fluorescence light will be reflected into a lens with a focal length of 100 mm. The lens is specially coated for wavelengths between 650 to 1050 nm. 100 mm behind the lens I installed a pinhole of diameter 50 um. The pinhole will ensure that only the fluorescence signal from the focal plane will be transmitted further. After the pinhole the diverging light beam will pass through a second lens, which ensures that the light beam will become parallel again. Lastly, the fluorescence light will move into an APD. The APD has been manufactured by Micro Photon Devices and belongs to the PDM series with a free space entrance (no fiber entrance). Photodiodes take advantage of the photoelectric effect and thus convert light into electricity. The APD are hereby especially sensitive in their light detection. Through the avalanche multiplication technique, the APDs are able to even detect single photons. The average photon detection efficiency is around 50%, and the detected photons will generate a TTL signal. Note that there is also a Spectrometer, next to the APD, connected to the laser beam path. However, except when trying to confirm that

the fluorescence signal is indeed originated from the NV centers, the Spectrometer is excluded from the standard setup configuration. The TTL signal will be detected by the NI Data Acquisition Board (NIDAQ), manufactured by National Instruments, and the specific modules attached to it. The NIDAQ is connected to a computer through a USB connector, and it is programmed with python.

B.6 Nanodiamond sample preparation

The nanodiamond solution was purchased from Academia Sinica (rFND-OH, 0.1% w/v) and FND Biotech, Inc. (cFND, 1 mg/mL, -COOH). The rFND (typically 50 nm, containing single NV) were used for the AFM and T_2 measurements, while the cFND (typically 200 nm, containing approximately 500 NV, obtained through milling (8000 M, SPEX) of microdiamond powder [92] were used for the FWHM measurements. Both nanodiamond types were initially covered by hydroxyl groups. The nanodiamond solutions were dropped on a 2 × 2 cm silicon substrate, which was previously cleaned using a 1:1 mixture of sulphuric acid and hydrogen peroxide at 190 °C for approximately 15 min. After dropping the nanodiamond solution onto the Si substrate, we placed the sample on a hot plate at 160 °C causing the water to evaporate.

B.7 NF etching laser parameters

The nanodiamonds were etched by the NF etching method, where induced ONFs at sub-wavelength protrusions are assumed to dissociate O_2 molecules, resulting in oxygen radicals (Fig. 5.4). For this purpose, they were vacuum-fixed onto the AFM stage, to ensure minimal misalignment of the nanodiamonds within the AFM measurement windows between each etching interval. In case of misalignments, an inbuilt function allows the

AFM stage control to refocus on the specific nanodiamonds. For the NF etching, a continuous-wave (CW) He-Cd laser (325 nm; 3.81 eV; excitation power density: 0.8 W/cm2) was chosen because its energy was below the bonding energy of O_2 (5.12 eV), thus avoiding conventional adiabatic etching. The emission line of the He-Cd laser for other wavelengths (outside 325 nm) is with a factor of around 10^{-4}, which is negligibly low and can therefore be ignored. The nanodiamond-hosting silicon plane was perpendicularly illuminated by the He-Cd laser for 30-min intervals between each measurement (structural change, T_2, and ODMR measurements).

Appendix C.

Methods and analysis for the experiments presented in Chapter 6

C.1 Photosensitive silver-ion solution

The reason for the photosensitivity of the silver-ion solution is due to one of its components, Irgacure 819 (Fig. C.1). When the Irgacure 819 moleculee is being hit by the right photon, it will split up into two charged ions. These then will act as an electron donor for the silver-ions in the solution, causing them to reduce to solid Ag_0, which agglomerates and is measurable with microscopy

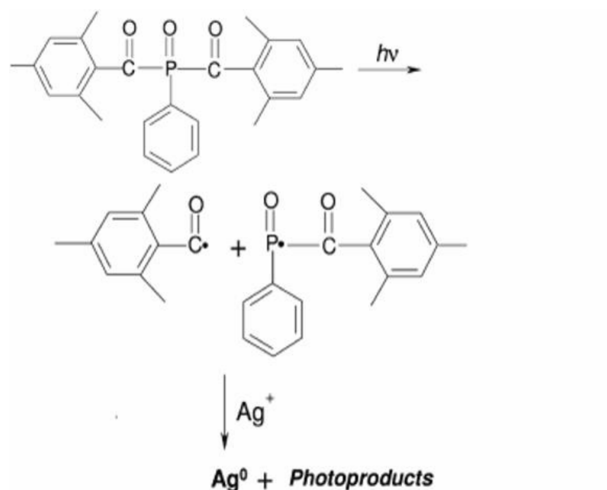

Figure C.1. Molecular structure of Irgacure 819 [110].

Chemical structure of the Irgacure 819 molecules, which acts as an electron donor for the silver-ions in the solution

More specifically, Fig. C.2 shows the spectrum for within which the photo-dissociation of the Irgacure 819 molecule can be triggered

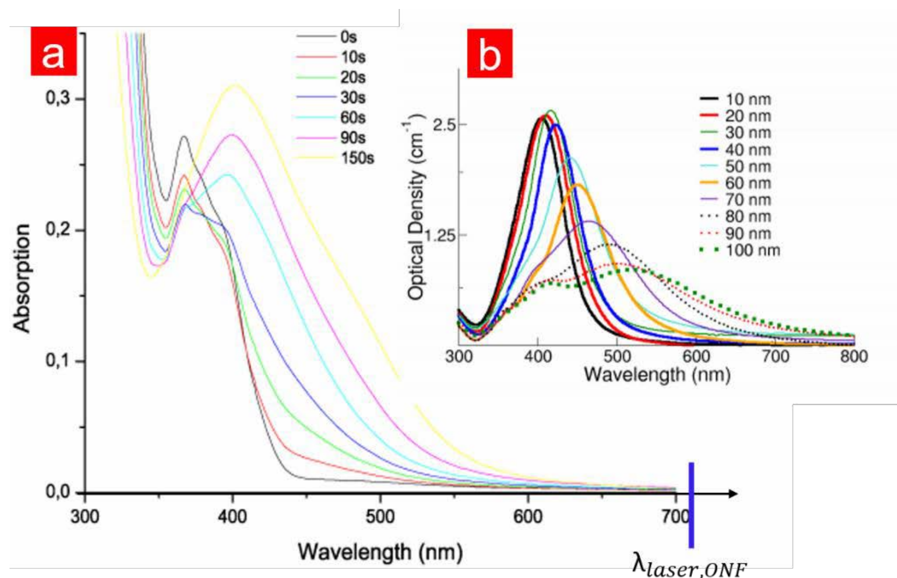

Figure C.2. Molecular structure of Irgacure 819 [110].

(a) Absorption spectrum of the Irgacure 819 molecule, changing over illumination time. (b) Optical spectrum of silver nanoparticles. Purple line depicts an ideal excitation laser wavelength, since far-field photons from that wavelength are not able to directly cause the photo-reduction (Reprinted with permission from [110]. Copyright 2010 IOP Publishing Ltd)

We note that in Fig. C.2 the spectrum changes over illumination time (405 nm light source). This is due to the fact that under 405 nm illumination solid silver is being synthesized and agglomerates into nanoparticles, which have their own optical spectrum (seen in Fig. C.2b). The result is that the newly synthesized silver nanoparticles inside the solution will shift the overall spectrum (hence a red-shift of the absorption spectrum over illumination time).

We have to note that for our experiment we will have to avoid common wavelengths which are within the typical absorption spectrum of Irgacure 819, in order to be able to conclude that the photo-dissociation has been caused by ONFs.

C.2 Machine vision software for evaluating TEM images for particle sizes

As the machine vision software we used the National Instruments Vision Assistant. This allowed us to create a binary map (threshold chosen manually) which in return allowed us to evaluate the nanoparticles. The software also offers particle analysis tools, with which various particle parameters (such as max ferret diameter or total area) can be obtained. It was also important to apply various filtering techniques for before the final binary mapping, in order to reduce the impact of noises. These filtering techniques included masking, smoothening, edge sharpening, increasing contrast and ignoring small particles (below a set threshold) functions. In Fig. C.3 we can see a typical binary image obtained be the NI software. Since the original TEM image (Fig. C.3 (left)) is not perfectly homogenous (shades, low resolution, etc.) it may be tricky to create a precise binary image. The parts which were successfully binary imaged have been described as “good” and the parts which were not able to be successfully binary imaged have been described as “bad”. Of course, for the final statistical analysis only particles which were precisely binary imaged to a high degree were used.

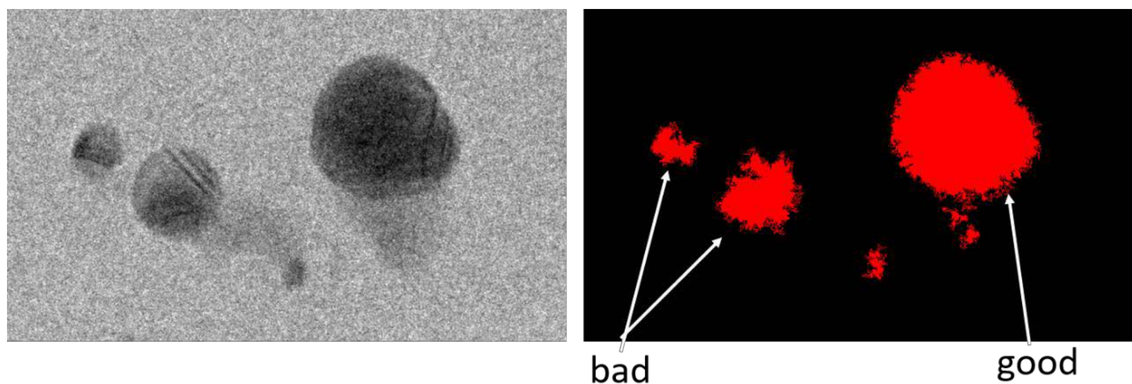

Figure C.3. National Instruments Computer Vision software

Binary imaging (right) of the original TEM image (left), setting the stage for further particle analysis tools.

C.3 Energy-dispersive X-ray spectroscopy (EDS) analysis of gold nanoparticles after experiment

A fundamentally important part in our experiment is to ensure that the size increase of the gold nanoparticles is indeed due to the reduction of silver ions along the gold nanoparticles surface. In order to verify this, we obtained the EDS images for typical gold nanoparticles after the experiment has been performed. What we can see in Fig. C.4 is that the X-ray spectroscopy clearly shows the presence of Au (initially present) and Ag (induced during the experiment).

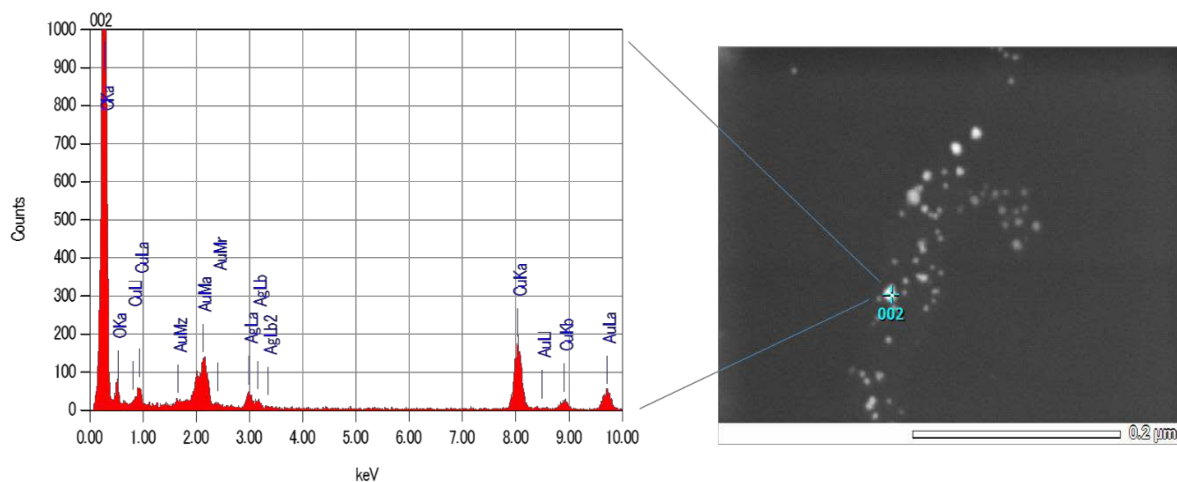

Figure C.4. EDS proof of Gold and Silver traces

EDS evaluation of a typical gold nanoparticle (seen on the right side) as seen in the TEM images. The X-ray spectrum shows clear traces of silver among the observed gold nanoparticle.

References

1. Moore, G. E. “Cramming More Components onto Integrated Circuits.” *Electronics* **38**, 114-117 (1965)
2. Pan, D., Liebmann, L., Yu, B., Xu, X. & Lin, Y. “Pushing Multiple Patterning in Sub-10nm: Are We Ready?” *In Proceedings of the 52nd Annual Design Automation Conference* **197**, 75.1 (2015)
3. Park, B. C., Cho, Y. C., Kim, I. & Yeo, J. “Roughness of EUV resists exposed to EUV, ArF and KrF radiation as evaluated using three tools: spectroscopic ellipsometry, AFM and SEM.” *Proc. SPIE* **8681**, 86812K (2013).
4. Tallents, G., Wagenaars, E. & Pert, G. “Optical lithography: Lithography at EUV wavelengths.” *Nat. Photonics* **4**, 809–811 (2010).
5. Wagner, C. & Harned, N. “Lithography gets extreme.” *Nat. Photonics* **4**, 24–26 (2010).
6. Ok, J. G., Shin, Y. J., Park, H. J. & Guo, L. “A step toward next-generation nanoimprint lithography: extending productivity and applicability.” *J. Appl. Phys. A* **121**, 343–356 (2015).
7. Oleksak, R. P., Ruther, R. E., Luo, F., Fairley, K. C., Decker, S. R., Stickle, W. F., Johnson, D. W., Garfunkel E. L., Herman, G. S. & Keszler, D. A. “Chemical and Structural Investigation of High-Resolution Patterning with HafSOx.” *ACS Appl. Mater. Interfaces* **6**, 2917–2921 (2014).
8. Lee, J., Kim, J., Jeong, S., Lim, M., Koo, S., Lim, C. & Kim Y. “Study on RLS trade-off resist upgrade for production ready EUV lithography.” *AIP Adv*. **6**, 085210 (2016).

9. Jianfeng, L. & Dornfeld, D. A. "Material removal mechanism in chemical mechanical polishing: theory and modeling." *IEEE Trans. Semicond. Manuf.* **14**, 112–133 (2001).

10. Kato, Y., Fujinaga, K., Nakamura, K., Takaya, Y., Kitamura, K., Ohta, J., Toda, R., Nakashima, T. & Iwamori, H. "Deep-sea mud in the Pacific Ocean as a potential resource for rare-earth elements." *Nat. Geosci*. **4**, 535–539 (2011).

11. Schirhagl, R., Chang, K., Loretz, M. & Degen, C. L. "Nitrogen-vacancy centers in diamond: nanoscale sensors for physics and biology." *Annual Review of Physical Chemistry* **65**, 83–105 (2014).

12. Maletinsky, P., Hong, S., Grinolds, M. S., Hausmann, B., Lukin, M. D., Walsworth, R. L., Loncar, M. & Yacoby, A. "A robust scanning diamond sensor for nanoscale imaging with single nitrogen-vacancy centres." *Nature Nanotech*. **7**, 320–324 (2012).

13. Grinolds, M. S., Hong, S., Maletinsky, P., Luan, L., Lukin, M. D., Walsworth, R. L. & Yacoby, A. "Nanoscale magnetic imaging of a single electron spin under ambient conditions." *Nature Phys*. **9**, 215–219 (2013).

14. Neumann, P., Jakobi, I., Dolde, F., Burk, C., Reuter, R., Waldherr, G., Honert, J., Wolf, T., Brunner, A., Shim, J. H., Suter, D., Sumiya, H., Isoya, J. & Wrachtrup. J. "High-Precision Nanoscale Temperature Sensing Using Single Defects in Diamond." *Nano Lett*. **13**, 2738–2742 (2013).

15. Kucsko, G., Maurer, P. C., Yao, N. Y., Kubo, M., Noh, H. J., Lo, P. K., Park, H. & Lukin, M. D. "Nanometre-scale thermometry in a living cell." *Nature* **500**, 54–58 (2013).

16. Rondin, L., Tetienne, J. P., Hingant, T., Roch, J. F., Maletinsky, P. & Jacques, V. “Magnetometry with nitrogen-vacancy defects in diamond.” *Rep. Prog. Phys*. **77**, 056503 (2014).

17. Ermakova, A., Pramanik, G., Cai, J. M., Algara-Siller, G., Kaiser, U., Weil, T., Tzeng, Y. K., Chang, H. C., McGuinness, L. P., Plenio, M. B., Naydenov, B. & Jelezko, F.”Detection of a Few Metallo-Protein Molecules Using Color Centers in Nanodiamonds.” *Nano Lett.* **13**, 3305–3309 (2013).

18. Degen, C., Reinhard, F. & Cappellaro, P. “Quantum Sensing.” *Rev. Mod. Phys.* **89**, 035002 (2017).

19. DiVincenzo, D. P. “The Physical Implementation of Quantum Computation.“ *Fortschritte der Physik* **48**, 771–783 (2000).

20. Cai, J.-M., Naydenov, B., Pfeiffer, R., McGuinness, L. P., Jahnke, K. D., Jelezko, F., Plenio, M. B. & Retzker, A. ”Robust dynamical decoupling with concatenated continuous driving.” *New Journal of Physics* **14**, 113023(2012).

21. Neumann, P., Mizuochi, N., Rempp, F., Hemmer, P., Watanabe, H., Yamasaki, S., Jacques, V., Gaebel, T., Jelezko, F. & Wrachtrup, J. “Multipartite Entanglement Amon Single Spins in Diamond.” *Science* **320**, 1326–1329 (2008).

22. Togan, E., Chu, Y., Trifonov, A. S., Jiang, L., Maze, J., Childress, L., Dutt, M. V. G., Sørensen, A. S., Hemmer, P. R., Zibrov, A. S. & Lukin, M. D. ”Quantum entanglement between an optical photon and a solid-state spin qubit.” *Nature* **466**, 730–734 (2010).

23. Neumann, P., Kolesov, R., Naydenov, B., Beck, J., Rempp, F., Steiner, M., Jacques, V., Balasubramanian, G., Markham, M. L., Twitchen, D. J., Pezzagna, S., Meijer,

J., Twamley, J., Jelezko, F. & Wrachtrup, J. "Scalable quantum register based on coupled electron spins in a room temperature solid." *Nat. Phys.* **6**, 249–253 (2010).

24. Degen, C. L. "Scanning magnetic field microscope with a diamond single-spin sensor." *Appl. Phys. Lett.* **92**, 243111 (2008).

25. Balasubramanian, G., Chan, I. Y., Kolesov, R., Al-Hmoud, M., Tisler, J., Shin, C., Kim, C., Wojcik, A., Hemmer, P. R., Krueger, A., Hanke, T., Leitenstorfer, A., Bratschitsch, R., Jelezko, F. & Wrachtrup, J. "Nanoscale imaging magnetometry with diamond spins under ambient conditions." *Nature* **455**, 648–651 (2008).

26. Breezem, J. D., Salvadori, E., Sathian, J., Alford, N. M., Kay, C. W. M. "Continuous-wave room-temperature diamond maser." *Nature* **555**, 493-496 (2018).

27. Clark, C. D. & Norris, C. A. "Photoluminescence associated with the 1.673, 1.944 and 2.468 eV centres in diamond." *J. Phys. C* **4**, 2223–2229 (1971).

28. Hopper, D. A., Shulevitz, H. J. & Bassett, L. C. "Spin Readout Techniques of the Nitrogen-Vacancy Center in Diamond" *Micromachines*. **9**, 437 (2018).

29. Gruber, A., Dräbenstedt, A., Tietz, C., Fleury, L., Wrachtrup, J. & von Borczyskowski, C., "Scanning Confocal Optical Microscopy and Magnetic Resonance on Single Defect Centers." *Science* **276**, 2012–2014 (1997).

30. Abeywardana, C., Peng, Z., Mugica, L. C., Kleinsasser, E., Fu, K. C. & Takahashi, S. "Investigation of Coherence Time of a Nitrogen-Vacancy Center in Diamond Created by a Low-Energy Nitrogen Implantation." *Applied Magnetic Resonance* **48**, 571–577 (2017).

31. Lovchinsky, I., Sushkov, A. O., Urbach, E., de Leon, N. P., Choi, S., De Greve, K., Evans, R., Gertner, R., Bersin, E., Müller, C., McGuinness, L., Jelezko, F., Walsworth, R. L., Park, H. & Lukin. M. D. "Nuclear magnetic resonance detection and spectroscopy of single proteins using quantum logic." *Science* **351**, 836–41 (2016).

32. Jackson, J.D. Classical electrodynamics. *Wiley* (1962).

33. Yamaguchi, M., Nobusadam K., Kawazoe, T. & Yatsui, T. "Two-photon absorption induced by electric field gradient of optical near-field and its application to photolithography." *Appl. Phys. Lett*. **106**, 191103 (2015).

34. Moskovits, M. "Surface-enhanced Raman spectroscopy: a brief retrospective." *J. Raman Spectrosc*., **36**, 485-496 (2005).

35. Zhang, R., Zhang, Y., Dong, Z. C., Jiang, S., Zhang, C., Chen, L. G., Zhang, L., Liao, Y., Aizourua, J., Luo, Y., Yang, J. L. & Hou, J. G. "Chemical mapping of a single molecule by plasmon-enhanced Raman scattering." *Nat*., **498**, 82-86 (2013).

36. Durr, N.J., Larson, T., Smith, D. K., Korgel, B. A., Sokolov, K. & Ben-Yakar, A. "Two-Photon Luminescence Imaging of Cancer Cells Using Moleculary Targeted Gold Nanorods." *Nano Lett*., **7**, 941-945 (2007).

37. Atwater, H. & Polman, A. "Plasmonics for improved photovoltaic devices." *Nat. Mater*., **9**, 205-213 (2010).

38. Yamaguchi, M. & Nobusada, K. "Photodissociation path in H_2^+ induced by nonuniform optical near fields: Two-step excitation via vibrationally excited states." *Phys. Rev. A*. **93**, 023416 (2016).

39. Yamaguchi, M. & Nobusada, K. “Indirect interband transition induced by optical near fields with large wave numbers.” *Phys. Rev. B*. **93**, 195111 (2016).

40. Lagzi, I. et al. Atmospheric Chemistry. *Eotvos Lorand University* (2013)

41. Katayama, M. “On the Temperature Dependence of the Molecular Polarization of Ammonia.“ *J. Chem. Phys*. **22**, 1473 (1954).

42. Flycarpet. (2019). Retrieved from http://www.flycarpet.net/en/psyonline

43. Maksyutenko, P., Rizzo, T. R. & Boyarkin, V. “A direct measurement of the dissociation energy of water.” *J. Chem. Phys.* **125**, 181101 (2006).

44. Yatsui, T., Hirata, K., Nomura, W., Tabata, Y. & Ohtsu, M. “Realization of an ultra-flat silica surface with angstrom-scale average roughness using nonadiabatic optical near-field etching.” *Apply. Phys. B*, **93**, 55-57 (2008).

45. Yatsui, T., Nomura, W., Naruse, M. & Ohtsu, M. “Realization of an atomically flat surface of diamond using dressed photon-phonon etching.” *J. Phys. D*, **45**, 475302 (2012).

46. Yatsui, T., Takeuchi, D., Koizumi, S., Sato, K., Tsuzuki, K., Iwasaki, T., Hatano, M., Makino, T., Ogura, M., Kato, H., Okushi, H. & Yamasaki, S. “Polarization-controlled dressed-photon-phonon etching of patterned diamond structures.” *Physica status solidi (a)*, **211**, 2339-2342 (2014).

47. Oyama, T. G., Oshima, A. & Tagawa, S. “Estimation of resist sensitivity for extreme ultraviolet lithography using an electron beam.” *AIP Adv*. **6**, 085210 (2016).

48. Neisser, M. et al. (2013). Retrieved from https://www.nist.gov

49. TSMC (2018). Fab 18. Retrieved from https://www.tsmc.com

50. Nishimura, Y., Hori, T., Yabu, T., Wakana, K., Ueno, Y., Soumagne, G., Nagai,

S., Yanagida, T., Kawasuji, Y., Shiraishi, Y., Abe, T., Nakarai, H., Saito, T. & Mizoguchi, H. "Key components development progress of high-power LPP-EUV light source with unique debris mitigation system using a magnetic field." *Proc. SPIE* **10809**, 108091M (2018).

51. Goldberg, K. A. "EUV photoresist patterning characterization for imec N7/N5 technology." *Proc. SPIE* **10583**, 1058312 (2018).
52. Mizuochi, N., Neumann, P., Rempp, F., Beck, J., Jacques, V., Siyushev, P., Nakamura, K., Twitchen, D. J., Watanabe, H., Yamasaki, S., Jelezko, F. & Wrachtrup, J. "Coherence of single spins coupled to a nuclear spin bath of varying density." *Phys. Rev. B* **80**, 041201 (2009).
53. DOW (2018). Retrieved from https://www.dow.com
54. Levinson, H.J. & Brunner, T.A. "Current challenges and opportunities for EUV lithography." *Proc. SPIE* **10809**, 1080903 (2018).
55. Murphy, J. N., Harris, K. D. & Buriak, J. M. "Automated Defect and Correlation Length Analysis of Block Copolymer Thin Film Nanopatterns." *PLoS ONE* **10**, e0133088 (2015).
56. Chandhok, M., Datta, S., Lionberger, D. & Vesecky, S. "Impact of line-width roughness on Intel`s 65-nm process devices." *Proc. SPIE* **6519**, 1A (2007).
57. De Bisschop, P. "Stochastic effects in EUV lithography: random, local CD variability, and printing failures." *J. Micro/Nanolith. MEMS MOEMS* **16**(4), 041013 (2017).
58. Nomura, W., Yatsui, T., Kawazoe, T., Tate, N. & Ohtsu, M. "High-speed flattening of crystallized glass substrates by dressed-photon-phonon etching." *Appl. Phys. A*

121, 1403–1407 (2015).

59. Keilin, D. & Hartree, E. F. "Absorption Spectrum of Oxygen." *Nature* **165**, 543–544 (1950).
60. Yatsui, T., Imoto, T., Mochizuki, T., Kitamura, K. & Kawazoe, T. "Dressed-photon-phonon (DPP)-assisted visible- and infrared-light water splitting." *Sci. Rep.* **4**, 4561 (2014).
61. Brandenburg, F. J., Okamoto, T., Saito, H., Soppera, O. & Yatsui, T. "Surface improvement of organic photo-resists through a near-field-dependent etching method." *Beilstein J. Nanotechnol.* **8**, 784–788 (2017).
62. De Bisschop, P. & Hendrickx, E. "Stochastic effects in EUV lithography." *Proc. SPIE* **10583**, 105831K (2018)
63. Shin, C. *Springer Series in Advanced Microelectronics* **56**, *Book.* (2016).
64. Doherty, M. W., Manson, N. B., Delaney, P., Jelezko, F., Wrachtrup, J. & Hollenberg, L. C. L. "The nitrogen-vacancy colour centre in diamond." *Physics Reports* **528**, 1-46 (2013).
65. Nizovtsev, A., Kilin, S. Y., Jelezko, F., Gaebal, T., Popa, I., Gruber, A. & Wrachtrup, J. "A quantum computer based on NV centers in diamond: Optically detected nutations of single electron and nuclear spins." *Optics and Spectroscopy*. **99**, 233–244 (2005).
66. Dynes, J., Takesue, H., Yuan, Z. L., Sharpe, A. W., Harada, K., Honjo, T., Kamada, H., Tadanaga, O., Nishida, Y., Asobe, M. & Shields, A. J. "Efficient entanglement distribution over 200 kilometers." *Optics Express*. **17,** 11440-11449 (2009).
67. Knowles, H. S., Kara, D. M. & Ataüre, M. "Observing bulk diamond spin coherence

in high-purity nanodiamonds." *Nat. Mater*. **13**, 21-25 (2014).

68. Balasubramanian, G., Neumann, P., Twitchen, D., Markham, M., Kolesov, R., Mizuochi, N., Isoya, J., Achard, J., Beck, J., Tissler, J., Jacques, V., Hemmer, P. R., Jelezko, F. & Wrachtrup, J. "Ultralong spin coherence time in isotopically engineered diamond." *Nat. Mater*. **8**, 383-387 (2009).
69. Fuchs, G. D., Dobrovitski, V. V., Toyli, D. M., Heremans, F. J. & Awschalom, D. D. "Gigahertz Dynamics of a Strongly Driven Single Quantum Spin." *Science* **326**, 1520-1522, (2009)
70. Element Six: Classification of Diamond. Retrieved from https://e6cvd.com
71. Jacques, V., Neumann, P., Beck, J., Markham, M., Twitchen, D., Meijer, J., Kaiser, F., Balasubramanian, G., Jelezko, F. & Wrachtrup, J. "Dynamic Polarization of Single Nuclear Spins by Optical Pumping of Nitrogen-Vacancy Color Centers in Diamond at Room Temperature." *Physical Review Letters* **102**: 057403 (2009)
72. Jeong, K., Parker, A. J., Page, R. H., Pines, A., Vassiliou, C. C. & King, J. P. "Understanding the Magnetic Resonance Spectrum of Nitrogen Vacancy Centers in an Ensemble of Randomly Oriented Nanodiamonds." *J. Phys. Chem. C* **121**, 21057-21061 (2017)
73. Pham, L. M. "Magnetic Field Sensing with Nitrogen-Vacancy Color Centers in Diamond." (Doctoral dissertation), Harvard University (2013).
74. Dréau, A., Lesik, M., Rondin, L., Spinicelli, P., Arcizet, O., Roch, J. F. & Jacques, V. "Avoiding power broadening in optically detected magnetic resonance of single NV defects for enhanced dc magnetic field sensitivity." *Physical Review B* **84**, 195204 (2011).

75. Taylor, J. M., Cappellaro, P., Childress, L., Jiang, L., Budker, D., Hemmer, P. R., Yacoby, A., Walsworth, R. & Lukin, M. D. "High-sensitivity diamond magnetometer with nanoscale resolution." *Nature Physics* **4**, 810 (2008).

76. Hauf, M. V., Grotz, B., Naydenov, B., Dankerl, M., Pezzagna, S., Meijer, J., Jelezko, F., Wrachtrup, J., Stutzmann, M., Reinhard, F. & Garrido, J. A. "Chemical control of the charge state of nitrogen-vacancy centers in diamond." *Phys. Rev. B* **83**, 081304 (2011).

77. Ofori-Okai, B. K., Pezzagna, S., Chang, K., Loretz, M., Schirhagl, R., Tao, Y., Moores, B. A., Groot-Berning, K., Meijer, J. & Degen, C. L. "Spin properties of very shallow nitrogen vacancy defects in diamond." *Phys. Rev. B* **86**, 081406 (2012).

78. Myers, B. A., Das, A., Dartiailh, M. C., Ohno, K., Awschalom, D. D. & Jayich, B. "Probing Surface Noise with Depth-Calibrated Spins in Diamond." *Phys. Rev. Lett.* **113**, 027602 (2014)

79. De Oliveira, F., Momenzadeh, S. A., Wang, Y., Konuma, M., Markham, M., Edmonds, A. M., Denisenko, A. & Wrachtrup, J. "Effect of Low-Damage Inductively Coupled Plasma on Shallow NC Centers in Diamond." *Appl. Phys. Lett.* **107**, 073107 (2015).

80. Rosskopf, T., Dussaux, A., Ohashi, K., Loretz, M., Schirhagl, R., Watanabe, H., Shikata, S., Itoh, K. M. & Degen, C. L. "Investigation of Surface Magnetic Noise by Shallow Spins in Diamond." *Phys. Rev. Lett.* **112**, 147602 (2014)

81. Kim, M., Mamin, H. J., Sherwood, M. H., Rettner, C. T., Frommer, J. & Ruger, D. "Effect of oxygen plasma and thermal oxidation on shallow nitrogen-vacancy centers in diamond." *Appl. Phys. Lett*. **105**, 042406 (2014)

82. Romach, Y., Müller, C., Unden, T., Rogers, L. J., Isoda, T., Itoh, K. M., Markham, M., Stacey, A., Meijer, J., Pezzagna, S., Naydenov, B., McGuinness, L. P., Bar-Gill, N. & Jelezko, F. "Spectroscopy of Surface-Induced Noise Using Shallow Spins in Diamond." *Phys. Rev. Lett*. **114**, 017601 (2015).

83. Yatsui, T., Yamaguchi, M. & Nobusada, K. "Nano-scale chemical reactions based on non-uniform optical near-fields and their applications." *Progress in Quantum Electronics* **55**, 166-194 (2017).

84. Yamaguchi, M. & Nobusada, K. "Large Hyperpolarizabilities of the Second Hamonic Generation Induced by Nonuniform Optical Near Fields." *J. Phys. Chem. C* **120**, 23748–23755 (2016).

85. Zurita-Sanchez, J. R. & Novotny, L. "Multipolar interband absorption in a semiconductor quantum dot. I. Electric quadrupole enhancement." *J. Opt. Soc. Am. B* **19**, 1355-1362 (2002).

86. Jain, P. K., Ghosh, D., Baer, R., Rabani, E. & Alivisatos, A. P. "Near-field manipulation of spectroscopic selection rules on the nanoscale." *Proc. Natl. Acad. Sci. USA* **109**, 8016-8019 (2012).

87. Kern, A. M. & Martin, O. J. F. "Strong enhancement of forbidden atomic transitions using plasmonic nanostructures." *Phys. Rev. A* **85**, 022501 (2012).

88. Filter, R., Mühlig, S., Eichelkraut, T., Rockstuhl, C. & Lederer, F. "Controlling the dynamics of quantum mechanical systems sustaining dipole-forbidden transitions via optical nanoantennas." *Phys. Rev. B* **86**, 035404 (2012).

89. Nagumo, R., Brandenburg, F. J., Ermakova, A., Jelezko, F. & Yatsui, T. "Spectral control of nanodiamond using dressed photon-phonon etching." *Applied Physics A* **121**, 1335–1339 (2015).

90. Su, L. J., Fang, C. Y., Chang, Y. T., Chen, K. M., Yu, Y. C., Hsu, J. H. & Chang, H. C. "Creation of high density ensembles of nitrogen-vacancy centers in nitrogen-rich type lb nanodiamonds." *Nanotechnology* **24**, 315702 (2013).

91. Brandenburg, F. J., Nagumo, R., Saichi, K., Tahara, K., Iwasaki, T., Hatano, M., Jelezko, F., Igarashi, R. & Yatsui, T. "Improving the electron spin properties of nitrogen-vacancy centres in nanodiamonds by near-field etching." *Sci. Rep.* **8**, 15847 (2018).

92. Hui, Y. Y., Zhang, B., Chang, Y. C., Chang, C. C., Chang, H. C., Hsu, J. H., Chang, K. & Chang, F. H. "Two-photon fluorescence correlation spectroscopy of lipid-encapsulated fluorescent nanodiamonds in living cells." *Opt. Exp.* **18**, 5896–5905 (2010).

93. Loretz, M., Pezzagna, S., Meijer, J. & Degen, C. L. "Nanoscale nuclear magnetic resonance with a 1.9-nm-deep nitrogen-vacancy sensor." *Appl. Phys. Lett.* **104**, 033102 (2014).

94. McGuinness, L. P., Hall, L. T., Stacey, A., Simpson, D. A., Hill, C. D., Cole, J. H., Ganesan, K., Gibson, B. C., Prawer, S., Mulvaney, P., Jelezko, F., Wrachtrup, J., Scholten, R. E. & Hollenberg, L. C. L. "Ambient nanoscale sensing with single spins using quantum decoherence." *New J. Phys.* **15**, 073042 (2013).

95. De Sousa, R. "Dangling-bond spin relaxation and magnetic 1/f noise from the amorphous-semiconductor/oxide interface: Theory." *Phys. Rev. B* **76**, 245306 (2007).

96. Bansal, R. C., Vastola, F. J. & Walker Jr., P. "Kinetics of chemisorption of oxygen on diamond." *Carbon* **10**, 443–448 (1972).

97. Grotz, B., Hauf, M. V., Dankerl, M., Naydenov, B., Pezzagna, S., Meijer, J., Jelezko, F., Wrachtrup, J., Stutzmann, M., Reinhard, F. & Garrido, J. A. "Charge state manipulation of qubits in diamond." *Nature Communications* **3**, 729 (2012)

98. Balasubramanian, G., Lazariev, A., Arumugam, S. R. & Duan, D. W. "Nitrogen-Vacancy color center in diamond-emerging nanoscale applications in bioimaging and biosensing." *Chemical Biology* **20**, 69-77 (2014)

99. Mapps, D. J. "Remote Magnetic Sensing of People." *Sensors and Actuators A: Physical* **106**, 321-325 (2003)

100. Yatsui, T., Saito, H., Nishioka, K., Leuschel, B., Soppera, O. & Nobusada, K. "Effects of a power and photon energy of incident light on near-field etching properties." *Appl. Phys. A*, **123**, 751 (2017).

101. Zuber, A., Purdey, M., Schartner, E., Forbes, C. J., Van der Hoek, B., Giles, D., Abell, A., Monro, T. M. & Ebendorff-Heidepriem, H. "Detection of gold nanoparticles with different sizes using absorption and fluorescence based method." *Sensors and Actuators B* **227**, 117-127 (2016).

102. Loubser, J. H. N. & van Wyk, J. A. "Electron spin resonance in the study of diamond." *Rep. Prog. Phys.* **41**, 1201–1248 (1978).

103. Mita, Y. "Change of adsorption spectra in type-lb diamond with heavy neutron

irradiation." *Phys.Rev.B*. **53**, 11360 (1996).

104. Lenef, A. & Rand, S. "Electronic structure of the N-V center in diamond: Theory." *Phys. Rev. B*. **53**, 13441 (1996).

105. Tamarat, P., Manson, N. B., Harrison, J. P., McMurtrie, R. L., Nizovtsev, A., Santori, C., Beausoleil, R. G., Neumann, P., Gaebel, T. & Jelekzo, F. "Spin-flip and spin-conserving optical transition of the nitrogen-vacancy centre in diamond." *New Journal of Physics*. **10**, 045004 (2008).

106. Collins, A.T, Thomaz, M. F. & Jorge, M. I. B. "Luminescence decay time of the 1.945 eV centre in type lb diamond." *Solid State Physics*. **16**, 2177 (1983).

107. Rogers, L.J., Armstrong, S., Sellars, M. J. & Manson, N. B. "Infrared emission of the NV centre in diamond: Zeeman and uniaxial stress studies." *New Journal of Physics*. **10**, 103024 (2008).

108. Robinson, M. E., Ng, J. D., Zhang, J. T., Buchman, J. T., Shenderova, O. A., Haynes, C. L., Ma, Z., Goldsmith, R. H. & Hamers, R. J. "Optically Detected Magnetic Resonance for Selective Imaging of Diamond Nanoparticles." *Anal. Chem*. **90**, 769-776 (2018).

109. Fuchs, G., Dobrovitski, V. V., Hanson, R., Batra, A., Weis, C. D., Schenkel, T. & Awschalom, D. D. "Excited-State Spectroscopy Using Single Spin Manipulation in Diamond." *Phys. Rev. Lett*. **101**, 117601 (2008).

110. Jradi, S., Balan, L., Zeng, X. H., Plain, J., Lougnot, D. J., Royer, P., Bachelot, R., Akil, S., Soppera, O. & Vidal, L. "Spatially controlled synthesis of silver nanoparticles and nanowires by photosensitized reduction." *Nanotechnology* **21**, 095605 (2010).

111. Elster, A. D. (2001) Retrieved from https://mriquestions.com

112. Dhumale, V. A., Shah, P. V., Sharma, R. B. & Tanabe, K. "Effects of particle size and surrounding media on optical radiation efficiencies of spherical plasmonic metal nanoparticles." *Bull. Mater. Sci* **35** (2), 143-149 (2012)

List of Publications

I. Journal Publications

1. Brandenburg, F. J., Okamoto, T., Saito, H., Soppera, O. & Yatsui, T. "Surface improvement of organic photo-resists through a near-field-dependent etching method," Beilstein Journal of Nanotechnology **8**, 784–788 (April 2017)
2. Brandenburg, F. J., Nagumo, R., Saichi, K., Tahara, K., Iwasaki, T., Hatano, M., Jelezko, F., Igarashi, R. & Yatsui, T. "Improving the electron spin properties of nitrogen-vacancy centres in nanodiamonds by near-field etching" Scientific Reports **8**, 15847 (October 2018)
3. Nagumo, R., Brandenburg, F. J., Ermakova, A., Jelezko, F. & Yatsui, T. "Spectral control of nanodiamond using dressed photon-phonon etching," Applied Physics A **121**, 1335-1339 (December 2015)

II. Conferences (International)

1. Brandenburg, F. J., Nagumo, R., Tahara, K., Iwasaki, T., Hatano, M., Jelezko, F. & Yatsui, T."Improvement in T2 times of NV-nanodiamond through near-field etching," The 11th Asia-Pacific Conference on Near-field Optics (APNFO11), July 10-13, 2017, National Cheng Kung University, Tainan, Taiwan, paper ID: Contr 10-6 (July 12, 2017)
2. Nagumo, R., Brandenburg, F. J., Igarashi, R., Jelezko, F., Iwasaki, T., Hatano, M., & Yatsui, T. "Improvement of Spin-Coherence Time of Nitrogen-Vacancy Center in Diamond using Near-field Etching," NFO-14: The 14th International Conference of Near-Field Optics, Nanophotonics

and Related Techniques, September 4-8, 2016, Act City Hamamatsu Concert Hall & Congress Center, Hamamatsu, Shizuoka, Japan, paper ID: Tu-9P-12, p.183 (September 2016)

3. Yatsui, T., Nagumo, R., Brandenburg, F. J., Iwasaki, T. & Hatano, M. "Near-field induced photochemical reaction for an ultraflat surface" 2016 Germany-Japan Workshop on Nanoscale Electron-Photon Interactions via Energy Dissipation and Fluctuation, Ulm University, Ulm, Land Baden-Württemberg, Germany, August 1-2, 2016, paper ID: TA-2 (August 2016)
4. Brandenburg, F. J., Nagumo, R. & Yatsui, T. "Study on near-field etching phenomena through selective control," 2016 Germany-Japan Workshop on Nanoscale Electron-Photon Interactions via Energy Dissipation and Fluctuation, Ulm University, Ulm, Land Baden-Württemberg, Germany, August 1-2, 2016, paper ID: TA-4 (August 2016)

III. Conferences (Domestic)

1. Brandenburg, F. J., Kameche, F., Leuschel, B., Soppera, O. & Yatsui, T. "Study on Near-Field effects by usage of photosensitive silver salt solution," JSPS Core-to-Core Japan Workshop 2018, Koshiba Hall, The University of Tokyo, Bunkyo-ku, Tokyo (July 2018)
2. Brandenburg, F. J., Saito, H., Soppera, O. & Yatsui, T. "Evaluation of the polarization dependence of an electron spin properties of NV nanodiamond through a near-field etching approach," The 65th JSAP Spring Meeting, West Waseda Campus, Waseda University, Shinjuku-ku, Tokyo, paper ID: 18a-A402-11 (March 2018)

3. Brandenburg, F. J., Saito, H., Soppera, O. & Yatsui, T. “Wavelength-dependence of near-field etching” The 64th JSAP Spring Meeting, Pacifico Yokohama, Nishi-ku, Yokohama, paper ID: 14p-F202-192 (March 2017)
4. Brandenburg, F. J., Nagumo, R., Yatsui, T., Ermakova, A. & Jelezko, F. “Confocal Microscopy on diamond substrate assisted by dressed photon-phonon etching” The 76th JSAP Autumn Meeting, Nagoya Congress Center, Atsuta-ku, Nagoya, paper ID: 16p-2G-3 (September 2015)
5. Nagumo, R., Brandenburg, F. J., Igarashi, R., Jelezko, F., Iwasaki, T., Hatano, M. & Yatsui, T. “Improvement of Spin-Coherence Time of Nitrogen-Vacancy Center in Diamond using Near-field Etching,” The 14th International Conference of Near-Field Optics, Nanophotonics and Related Techniques, Act City Hamamatsu, Hamamatsu, Shizuoka, paper ID: Tu-9P-13 (September 2016)